Imperial College London
Department of Chemical Engineering

Microfluidic Visualisation and Analysis of Multiphase Flow Phenomena at the Pore Scale

Imperial College London

Emily May Chapman

31st December 2014

Submitted in part fulfilment of the requirements for the degree of
Doctor of Philosophy in Chemical Engineering of Imperial College London

Abstract

Micro-fluidic devices have been designed and used to investigate immiscible fluid-fluid displacement processes. Due to their optically transparent nature, such devices allow direct visualisation of pore scale events using light microscopy. In this thesis, we focus on imaging multiphase flow phenomena at the pore scale within specifically designed micro-models using optical and Raman microscopy. The flow channel designs have been selected to investigate fundamental questions relating to fluid displacement mechanisms.

The Lucas-Washburn equation predicts that the distance a meniscus travels within a smooth cylindrical capillary is proportional to the square root of time. However, it is poorly understood how surface roughness of the capillary influences the rate of imbibition. This is of great importance for flow in real porous media. Therefore, the displacement dynamics within a series of single capillaries of increasing surface roughness was investigated. It was found that as the roughness increased, the rate of penetration decreased. The rate of decrease with increasing roughness was observed to be different from recent computer simulation studies.

Using specifically designed single-junction micro-models, the role of pore geometry on fluid displacement during drainage and imbibition processes is investigated via quasi-static and spontaneous experiments under ambient conditions. The experimental results are directly compared to theory and Lattice Boltzmann Model (LBM) simulations. The experimental critical pore filling pressures observed for the quasi-static experiments agree well to those predicted by the Young-Laplace equation and follow the expected filling sequence. However, the experimental spontaneous imbibition results were found to be different from those predicted by the Young-Laplace equation: instead of entering the narrowest available downstream throat, the wetting phase enters an adjacent throat first. Thus, pore geometry plays a vital role as it becomes the main deciding factor in the displacement sequence. This observation may have serious implications for the prediction of displacement processes at the Darcy

scale: current Pore Network Models (PNMs) adopt the Young-Laplace displacement sequence for spontaneous imbibition processes and may therefore need to be revised. To further consider these observations, more complex models consisting of multiple connected junctions, are being investigated.

Finally, experiments have been conducted to investigate Raman spectroscopy to understand surfactant enhanced oil recovery (EOR) processes within micro-models. This may prove particularly useful for EOR as micro-emulsion formation is difficult to discern optically. The work presented demonstrates that Raman spectroscopy is an effective technique in visualising pore scale fluid flow processes and distributions.

DECLARATION OF ORIGINALITY

I hereby declare that the work presented here is entirely my own. Where I have incorporated the work of others it has been acknowledged and referenced appropriately.

The copyright of this thesis rests with the author and is made available under a Creative Commons Attribution Non-Commercial No Derivatives licence. Researchers are free to copy, distribute or transmit the thesis on the condition that they attribute it, that they do not use it for commercial purposes and that they do not alter, transform or build upon it. For any reuse or redistribution, researchers must make clear to others the licence terms of this work.

Acknowledgments

I would like to express my sincere gratitude to my supervisors Dr. Edo Boek and Dr. John Crawshaw for giving me this opportunity to continue my scientific education. Their insightful guidance, encouragement and support during my Ph.D has been essential. It has been a pleasure working in the Complex Fluids Group from the beginning!

The entire group have helped my throughout my Ph.D but in particular I would like to acknowledge Christine Seifried, Nathan Welch, Ruien Hu, and Dr. Saurabh Shah for their indispensable experimental support and encouragement. Furthermore, the morale boosting tea sessions in the common room with Christine Seifried and Daniel Ross kept me motivated. I am appreciative to Dr. Jianhui Yang and Dr. Ioannis Zacharoudiou for their time and expertise conducting the Lattice Boltzmann simulations. Outside of Imperial I would like to recognise Dr. Apostolos Georgiadis and Dr. Holger Ott for providing the opportunity to experience and learn from the Shell laboratories.

I would especially like to thank my family: my parents Kevin and Jennifer for their never-ending love and guidance across the miles and my siblings Charlotte and Alastair for providing comic relief when needed. Last but not least, I would like to thank my partner Dom without whose constant support, encouragement and patience it would not have been possible for me to finish this Ph.D.

I would also like to gratefully acknowledge the funding through the EPSRC Doctoral Training Award and the Qatar Carbonates and Carbon Storage Research Centre (QCCSRC), provided jointly by Qatar Petroleum, Shell, and Qatar Science & Technology Park.

Nomenclature

α	Polarisibility
ΔA	Change in Surface Area
ΔG_M	Free energy of formation of micro-emulsions
ΔS	Entropy
Δw	Raman Shift
η	Viscosity of the fluid
γ	Interfacial Tension
γ_{gl}	Interfacial Tension between the gas/liquid
γ_{sg}	Interfacial Tension between the solid/gas
γ_{sl}	Interfacial Tension between the solid/liquid
λ_0	Incident radiation wavelength
λ_1	Raman radiation wavelength
λ_{em}	Laser wavelength
ρ	Density of the fluid
θ	Equilbrium contact angle
θ^a	Advancing dynamic contact angle
ϖ	Dipole moment

ξ Coefficient of friction

A Cross-sectional area

$A1$ Surface area of the bulk dispersed phase

$A2$ Surface area of the micro-emulsion droplets

Bo Bond number

Ca Capillary number

d Depth of throat

dA Increase in surface area

dW Energy required to increase the surface area by one unit

dx Displacement

$E_{Head-Brine}$ Head-Brine Energy Term

$E_{Tail-Oil}$ Tail-Oil Energy Term

G Shape factor

g Gravity

h Height difference between the reservoir and the model

l Distance the meniscus has travelled into the capillary

n Number of atoms

Oh Ohnesorge number

P Perimeter

P_C Capillary pressure

P_{NW} Non-wetting phase pressure

P_P	Piston-like displacement critical pressure
P_S	Snap-off critical pressure
P_W	Wetting phase pressure
R	Radius of a circle fitted to the curvature of the interface
r^*	Mean radius of curvature
$r_{1,2}$	Principal radii of curvature
R_H	Hydraulic radius
Re	Reynolds number
S_{OR}	Residual saturation
S_{WC}	Connate water saturation
t	Time
t_1	Initial settling phenomena time-scale
t_2	Viscous time-scale
v	Velocity of fluid
w	Width of the capillary
w_t	Width of throat
fps	Frames per second
IFT	Interfacial tension
IOS	Twin-tailed internal olefin sulphonates
IR	Infra-red
LBM	Lattice Boltzmann Method

NWP Non-wetting phase

PNM Pore network model

scCO$_2$ Supercritical CO$_2$

WP Wetting phase

WR Winsor Ratio

List of Figures

1.1. A) Combined land and ocean surface temperature from 1850 – 2012, taken from Figure SPM.1(a), p.6 [1] B) Atmospheric CO_2 levels recorded at the Mauna Loa Observatory from 1960 – 2012, [2]. 23

1.2. Diagram illustrating the different geological storage mechanisms involved in carbon sequestration: structural (hydrodynamic), capillary (residual), dissolution and mineral trapping. Image courtesy of CO_2 Capture Project [3]. 25

1.3. Schematic of the typical oil recovery process. Once primary recovery is no longer viable, either secondary or tertiary recovery (EOR) procedures are applied. The red boxes illustrate the EOR process of interest for this thesis - Surfactant flooding. 27

2.1. Schematic of contact angle (θ) with the respective interfacial tensions: γ_{gl} (gas/liquid), γ_{sg} (solid/gas) and γ_{sl} (solid/liquid). 31

2.2. Equilibrium at a curved interface between two immiscible fluids, modified from [4], p.445. 32

2.3. Schematic of two immiscible fluids within a capillary tube of radius r, where the radius of curvature is $R = \frac{r}{cos(\theta)}$, where R is radius of a circle fitted to the curvature of the interface. 32

2.4. Simplified drainage/imbibition capillary pressure curve - during primary and secondary drainage the capillary pressure systematically increases with increasing NWP saturation to connate water saturation (S_{WC}), whereas the capillary pressure decreases with increasing WP saturation during imbibition to residual saturation (S_{OR}). 33

2.5. Schematic diagram of snap-off mechanism which can occur during imbibition. Here the WP is shown in red. The WP films swell and eventually become unstable at critical meniscus position illustrated by the red dashed line. 35

2.6. I1 – I3 pore body filling events, WP shown in red. 35

2.7. Schematic of the cross-sectional shapes - circular, triangular and square - used as the network elements within PNMs [5]. . 40

2.8. Schematic illustrating the chemical structure of an anionic surfactant molecule. The hydrophilic head group is located within the solvent (most commonly water), whilst the hydrophobic tail sticks out into the oil phase [6]. 42

2.9. Schematic of micro-emulsion formation. IFT decreases from I to II with the subdivision of the dispersed phase into much smaller droplets. This leads to an increase of surface area, surface energy and entropy assuming IFT and T remain constant. 44

2.10. Schematic of Winsor type micro-emulsions. Winsor I – oil-in-water micro-emulsion, Winsor II – water-in-oil micro-emulsion, Winsor III – middle phase micro-emulsion. 45

2.11. Regular two-dimensional networks of cylindrical tubes used by Fatt *et al.* [7] to improve visualisation of flow phenomena. 48

2.12. Schematic cross-section of the network used by Lenormand *et al.* [8]. 50

3.1. Images of rough capillaries used within this study. The roughness increases from Cap_50_0 to Cap_50_4. 55

3.2. The original .bmp files of the rough capillary designs investigated going from smoothest (Cap_50_0) to roughest (Cap_50_4): top to bottom. 55

3.3. Schematic micro-model designs, including channel configuration and connectors A) Square pore with equal throats, B) more complex pore body with equal throats, C) square pore with unequal channels, D) more complex pore body with unequal channels, E) single representative Berea pore. 56

3.4. Schematic of 'Abstract' network model. The main features are the inlet/outlet ports and fracture channels located at either end of the model. The 'porous plate' structure is situated at one end of the model with the matrix design in the centre. 58
3.5. Berea micro-model throat distribution in comparison to actual Berea thin section. Micro-model results from personal communication. Berea thin section results from [9]. 58
3.6. Image of a section of the 'porous plate' within the micro-model. The narrow throats of the 'porous plate' are 8 μm in width. 59
3.7. A) subsection of the 'abstract' network design B) the corresponding throat distribution created by the MatLab code . . 60
3.8. The final 'abstract' micro-model design, including the 'porous plate' on the right-hand-side of the design. 61
3.9. A) General wafer layout for PMMA micro-models B) Top down view of model C) cross-section of model including connections. 63
3.10. General etching procedure for glass micro-models. Provided by The Dolomite Centre Ltd. 64
3.11. A) Original PEEK glass micro-model holder, close-up illustrates the fitting directly touching the micro-model B) modified PEEK glass micro-model holder with the addition of an o-ring contacting the micro-model. 64
3.12. Schematic of a Zeiss AxioObserver A1.m inverted light microscope. A list of components is given below. 67

4.1. Schematic of the cross-section of borosilicate caillaries A) 500 x 50 μm B) 4000 x 400 μm [10]. 73
4.2. Image illustrating the increase in roughness for the silicon/-glass etched capillaries investigated 74
4.3. A) Width of the capillary B) Entrance of the capillary C) Entrance of the capillary 74
4.4. A) HSVM set-up in transmitted light mode using the illuminated stage base B) HSVM set-up in reflected light mode using additional lighting from above 75

4.5. Smooth capillary results A) 500 × 50 μm Runs 1-3 B) 4000 × 400 μm Runs 1-3 C) 500 × 50 μm Run 2 including trend lines for Time and Time$^{0.5}$ to illustrate the different time regimes D) 500 × 50 μm Run 2 and 4000 × 400 μm Run 3 including $t^{0.5}$ trend line with neither reaching the Lucas-Washburn regime. 76

4.6. Pinned meniscus taken with 50× objective, the imbibing DI water is blue whilst the empty capillary is orange 78

4.7. Snap-shot of the meniscus within a rough capillary taken with the DSLR camera. 78

4.8. Meniscus position vs time for capillaries of different roughness (Cap_50_0 – smoothest to Cap_50_4 – roughest) 79

4.9. A) Original data of selected runs of all the capillaries B) Normalised data for all the capillaries, in which the roughest capillary is also the slowest. 80

4.10. Selected single runs from each capillary of difference roughness illustrating the transition from the visco-inertial regime (black dashed line) to the Lucas-Washburn regime (red dashed line). 81

4.11. Single runs of the different rough capillaries from Cap_50_-0 (smoothest) to Cap_50_4 (roughest) all presented with the linear fit at late times. 82

4.12. Change in intercept vs change in capillary roughness. 83

5.1. Single junction micro-model with throat width measured using ILM and supporting software AxioVision. 88

5.2. Superimposed circle used to calculate the contact angle from static images. Open source software ImageJ was used to draw and measure the circle. 89

5.3. A) Experimental set-up B) Schematic of experimental set-up illustrating the height measured. 90

5.4. Plan view of the PMMA micro-model design, including the cross-section of a micro-model imaged using the CLSM. . . . 91

5.5. Sequence of WP displacement during quasi-static primary drainage. The model was initially filled with WP (white) before being displaced by NWP (grey). The contact angle is 26°. 93

5.6. Forced drainage experiment with corresponding LBM simulations in which DI water is injected at a flow rate of 6μl/hour. The displacement pathway observed corresponds with the Young-Laplace law prediction; even though throats *1* and *3* are encountered by the NWP before *4*, their high capillary entry pressure prohibits entry. 95

5.7. Primary drainage images: A) experimental images of forced injection of NWP at 0.5 ml/min; B) corresponding LBM simulations. WP – wetting phase (n-decane). NWP – non-wetting phase (air). 95

5.8. Quasi-static I1, I2, I2A and I3 imbibition experimental results (WP is white, NWP grey). The critical radii used to calculate the displacement pressures for each case are also illustrated in red. 97

5.9. Predicted displacement sequence for Quasi-static I3 imbibition using the Young-Laplace equation for a contact angle of 16°, with the narrowest throat filling first via snap-off (P_S) followed by the body filling through piston-like displacement (P_P). 99

5.10. Quasi-static I3 imbibition experimental results (WP: white, NWP: grey, Wetting films: black). Snap-off occurs in the narrowest throat before the meniscus enters the pore as predicted by the Young-Laplace equation. 99

5.11. Quasi-static I3 imbibition experimental results (WP: white, NWP: grey, Wetting films: black). Snap-off occurs in the narrowest throat before the meniscus enters the pore as predicted by the Young-Laplace equation. 100

5.12. Spontaneous I3 imbibition experimental results (top row, throat widths: r_2(T1) = 27 μm, r_2(T2) = 47 μm, r_2(T3) = 60 μm, r_2(T4) = 100 μm, etch depth = 55 μm), with the corresponding LBM simulations (bottom row); here the WP travels down the adjacent throat first. This behaviour is not predicted by the Young-Laplace law (5.1). 101

5.13. Spontaneous Imbibition I3 experiment in a pore shape representative of Berea sandstone with corresponding LBM simulations. Here the WP travels down the adjacent throat first. This behaviour is not predicted by the Young-Laplace law (5.1). 102

5.14. A) Interface tracking of the meniscus in throat 3 as a function of time for the experiments. B) Rescaled length as a function of dimensionless time for both experiment and LB simulations. Ohnesorge numbers: Oh=2.1 ($sims_1$), Oh=1.6 $\times 10^{-1}$ ($sims_2$), $Oh = 7.3 \times 10^{-2}$ ($sims_3$). 103

6.1. 'Abstract' network model design fabricated in PMMA. Four throat widths (30, 50, 64 and 104 μm) randomly distributed to create a larger model. 106

6.2. Experimental set-up of the gravity driven flow micro-model experiments. 107

6.3. A) Modified camera stand B) Linear actuator control panel. . 108

6.4. A) Image of micro-model 100 % saturated with n-decane + Oil Red EGN B) Micro-model after drainage C) Micro-model after drainage + Background correction applied D) Segmented image, white - air (non-wetting phase, NWP). . . 109

6.5. Pressure testing of glass micro-model. 110

6.6. Saturation curve for PMMA micro-model drainage/imbibition cycle. 111

6.7. A) Image of DI water + Methyl Blue saturated glass micro-model before drainage/imbibition began B) Micro-model at the end of drainage C) Micro-model after imbibition. 112

7.1. Optical path for visible light in LabRAM HR Evolution Raman spectrometer. The red line is route the laser light travels to the sample. Whilst the pink line is the route the scattered light travels from the sample to the CCD detector. HORIBA Scientific. 117

7.2. Spectrograph optic path for LabRam HR Evolution Raman spectrometer. HORIBA Scientific. 117

7.3. Possible Raman frequencies. Of interest is inelastic scattered light - Stokes Raman and Anti-Stokes Raman. HORIBA Scientific [11]. 119

7.4. Chemical structure of Internal olefin sulphonates investigated Left: Alkene sulphonate Right: Hydroxy alkane sulphonate. . 120

7.5. Chemical structure of A) *n*-decane and B) *d*-decane, where the hydrogen molecules have been replaced with deuterium. . 121

7.6. Schematic of homogeneous micro-model matrix pattern used in this study. Pattern consisted of pore bodies with a width – 60μm, throat width – 13μm, etch depth – 5μm and a coordination number of 6 (personal communication). 121

7.7. Example of a square grid used for mapping purposes. 124

7.8. A) Raman spectra for an empty micro-model used as the reference spectra B) Raman spectrum of water before (blue line) and after (red line) baseline correction. 125

7.9. Spectra of other possible materials to fabricate micro-models – Borofloat 33, D 263 glass and fused Silica. All have a response ca. 450 – 500 cm^{-1} due to the Si-O-Si bonds present.126

7.10. A) Water (red) and 5 wt% surfactant (purple) spectra illustrating the difference between the two especially at ca. 2800 cm^{-1} B) Spectra for 1 – 5 wt% surfactant solutions, C) S03 and S=O peaks relating to the sulphonate head group and the OH bending peak ca. 1600 cm^{-1}. D) Peak height ratio for S=O/OH bending peak. 128

7.11. Phase behaviour test conducted within a pipette. The middle phase is a Winsor III micro-emulsion. [12] 129

7.12. Spectrum for an optimum micro-emulsion created from 2% Surfactant + 2.2% NaCl during a phase behavior test, where oil phase was *n*-decane. Both the water peak and CH_2/CH_3 peaks can be seen, however, cannot distinguish how much of the CH_2/CH_3 peak is from the surfactant and *n*-decane, In addition the surfactant head peaks are difficult to identify (inset) 130
7.13. A) Optical image of a pore body within the micro-model in which two phases are present B) Spectra acquired for the different phases within the pore body, Acq. Time 5 s, Accumulations 2, Range 400-4000 cm-1, 50× LWD objective, 1800 gr/mm grating and 200 hole size. C) Intensity map relating to the peaks highlighted in the spectra 131
7.14. Spectra for both *n*-decane and *d*-decane, illustrating the shift in peak locations due to the change in bonds from hydrogen to deuterium. Some CH_2/CH_3 peaks are still present in the *d*-decane due to its 99% purity. 133
7.15. A) Micro-emulsion spectra including, with the insert of the micro-emulsion within the micro-model. B) Spectra illustrating the difference between the micro-emulsion and the *d*-decane. Three phases can be clearly identified: water, surfactant and *d*-decane. C) illustrates the difference between the CH_2/CH_3 peaks in B. 134

C.1. NOAA permission to reprint Figure 1.1.B. 183
C.2. CO_2 Capture Project permission to reprint Figure 1.2. 183
C.3. Dover permission to reprint Figure 2.2. 184
C.4. SPE permission to reprint Figure 2.8. 185
C.5. Cambridge University Press permission to reprint Figure 2.12. 186
C.6. VitroCom permission to reprint Figure 4.1. 187
C.7. HORIBA Scientific permission to reprint Figures 7.1, 7.2 and 7.3. 187
C.8. SPE permission to reprint Figure 7.11. 188

List of Tables

3.1. Properties of rough capillaries investigated 56
3.2. Capillary entry pressures for selected throat widths. Selected fluid n-decane, etch depth 50 μm, contact angle 30° and IFT 0.024 N/m 57
3.3. Capillary entry pressures for narrowest throat in matrix design and throats of porous plate. Selected fluid DI water, etch depth 25 μm, contact angle 30° and IFT 0.072 N/m . . . 59
3.4. Details of Objectives found on the ILM 66

4.1. Properties of the rough capillaries investigated 81

5.1. Critical pressures for drainage in throats 51, 65 and 107 μm in a model with unequal throat widths calculated via equation 5.1 and experimental data. Contact angle: 26°, etch depth: 45 μm, interfacial tension: 0.024N/m. 94
5.2. Critical pressures for I1, I2, I2A and I3 pore filling events within a micro-model with equal throat widths. Critical pressures calculated via equation 5.1 and experimental data. Contact Angle: 28°, etch depth: 56 μm, throat width: 73 μm, pore width: 238 μm, γ: 0.024 N/m. 98

7.1. Raman shift locations of CH_2 and CH_3 corresponding to the hydrocarbon chain 129

Contents

1. Introduction **22**
1.1. Anthropogenic CO_2 emissions and Climate Change 22
1.2. Carbon Sequestration 23
1.3. Enhanced Oil Recovery 26
1.4. Outline 27

2. Background and Literature Review **29**
2.1. Multiphase Flow 30
2.1.1. Fundamentals of Multiphase Flow 30
2.1.2. Drainage and Imbibition 32
2.1.3. Quasi-static Displacement 35
2.1.4. Dynamics of Multiphase Flow 36
2.1.5. Computational Methods 39
2.2. Surfactants and Micro-emulsions 41
2.2.1. Surfactants 41
2.2.2. Micro-emulsions 43
2.3. Applications of Micro-models 46
2.3.1. History of Micro-models 47
2.3.2. Displacement Processes within Micro-models 51
2.4. Motivation 53

3. Micro-model Fabrication and Imaging Techniques **54**
3.1. Micro-model Design 54
3.2. Micro-model Fabrication 60
3.3. Imaging Techniques 65
3.3.1. Inverted Light Microscope (ILM) 65
3.3.2. High Speed Video Microscope (HSVM) 68
3.3.3. DSLR Camera 69

4. Exploring the Lucas-Washburn Equation: Rough Capillaries 71
4.1. Introduction . . . 71
4.2. Experimental Set-up . . . 72
4.3. Results and Discussion . . . 76
4.3.1. Smooth Capillaries . . . 76
4.3.2. Rough Capillaries . . . 77
4.4. Conclusions . . . 83

5. Exploring the Young-Laplace Equation: Single Junctions 85
5.1. Introduction . . . 86
5.2. Experimental Set-up . . . 87
5.3. Results and Discussion . . . 92
5.3.1. Drainage Results . . . 93
5.3.1.1. Quasi-static displacement. . . . 93
5.3.1.2. Forced Drainage . . . 94
5.3.2. Imbibition . . . 96
5.3.2.1. Quasi-static imbibition . . . 96
5.3.2.2. Spontaneous imbibition . . . 98
5.4. Conclusions . . . 103

6. 'Abstract' Network Models 105
6.1. Introduction . . . 105
6.2. Experimental Set-up . . . 106
6.3. Results and Discussion . . . 110
6.3.1. PMMA micro-models . . . 110
6.3.2. Glass micro-models . . . 111
6.4. Conclusions . . . 113

7. Phase Identification using Raman Spectroscopy within Micro-models 114
7.1. Introduction . . . 115
7.1.1. Introduction to Raman Spectroscopy . . . 115
7.2. Experimental Set-up . . . 120
7.3. Results and Discussion . . . 126
7.3.1. Calibration of Single Surfactant Phases . . . 127
7.3.2. Micro-emulsion and Multiple Phases in Micro-models 130

7.4. Conclusions 134

8. Conclusions and Future Work **137**
8.1. Conclusions 137
8.2. Recommendations for Future Work 139
8.2.1. Lucas-Washburn Studies 139
8.2.2. Young-Laplace Studies 140
8.2.3. Raman Spectroscopy 141

Appendices **166**

A. MatLab Code **167**

B. ImageJ Macros **180**

C. Permissions **183**

1. Introduction

Since the onset of the Industrial Revolution, society's growth and development has been propelled forward by the ever increasing consumption of fossil fuels, with no signs of slowing down anytime soon. Through this continued consumption of fossil fuels, the first world has achieved a high standard of living which they are unwilling to give up and that many developing countries still strive for [1, 13]. Therefore, to maintain this life style, and for others to obtain it, energy demands will continue to rise. At present, meeting this growing energy demand can only be achieved through the combustion of fossil fuels [13]. Currently, around 80% of all global energy is derived from fossil fuels (coal, oil and natural gas) [13]. However, this dependency on fossil fuels for our energy needs and economic growth may not continue forever, as we are dealing with a finite resource. Furthermore, it is now generally agreed that the combustion of fossil fuels has led to ever increasing levels of anthropogenic carbon dioxide (CO_2) in the atmosphere. Therefore steps must be taken to constrain the amount of CO_2 reaching the atmosphere. This may be achieved by carbon capture and storage (CCS) in saline aquifers. In addition, enhanced oil recovery (EOR) may be considered by injecting CO_2 in depleted oil reservoirs. To optimise the residual saturation of the CO_2 after initial injection, a detailed understanding of pore scale fluid flow is required. This is the main topic of the current PhD thesis.

1.1. Anthropogenic CO_2 emissions and Climate Change

Since the onset of the Industrial revolution anthropogenic CO_2 emissions have been rising, with pre-industrial levels of roughly 280 ppm (parts per million) increasing to historic highs of over 400 ppm, primarily as a conse-

quence of fossil fuel combustion [13]. Therefore, it is of upmost importance that steps are taken to help control anthropogenic CO_2 emissions as it is now generally agreed that these emissions are causing global temperatures to rise with unknown consequences. Figure 1.1 illustrates the relationship between rising global temperature and anthropogenic CO_2 levels [2, 14]. Therefore, limiting the amount of CO_2 emissions reaching the atmosphere is essential until more environmentally friendly energy resources are available. Whilst there is no single solution, one key technology could be the capture and sequestration of anthropogenic CO_2 emissions in suitable geological formations – CCS.

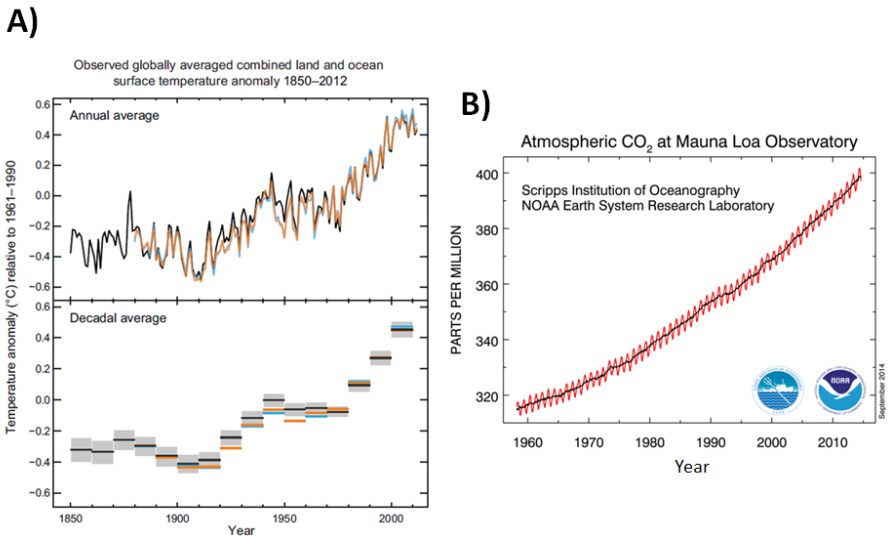


Figure 1.1.: A) Combined land and ocean surface temperature from 1850 – 2012, taken from Figure SPM.1(a), p.6 [1] B) Atmospheric CO_2 levels recorded at the Mauna Loa Observatory from 1960 – 2012, [2].

1.2. Carbon Sequestration

Carbon sequestration refers to the injection and long-term storage of anthropogenic CO_2 in suitable storage locations to help constrain emissions reaching the atmosphere. Two main storage locations have been suggested: the deep ocean [15, 16] and geological formations [15, 17, 18]. Of these, sequestration in geological formations is most appealing due to security of

storage and the large storage volumes available globally. Potential geological storage locations include: depleted oil and gas reservoirs, coal beds and deep saline aquifers. Deep saline aquifers provide the greatest storage capacity, and they have a wide distribution globally.

One of the major concerns regarding geological CO_2 sequestration is the long term security of the injected CO_2. Understanding the potential for leakage from the storage locations is essential, as significant loss would make sequestration ineffective. Therefore, to avoid such a situation arising, a thorough understanding of the trapping mechanisms involved in geological sequestration is essential. The trapping mechanisms are outlined below and illustrated in Figure 1.2:

1. **Structural Trapping** (or hydrodynamic trapping): is the physical trapping of injected CO_2 by a thick impermeable layer, also known as a cap-rock; here the more buoyant CO_2 is prevented from migrating to the surface. Therefore, to ensure safe storage over short time scales, it is vital that the cap-rock is well characterised before injection begins [17].

2. **Capillary Trapping** (or residual trapping): primarily occurs once CO_2 injection has stopped and the more buoyant CO_2 migrates upwards with the surrounding in-situ brine moving in behind and displacing the CO_2 due to imbibition processes.[19, 20] The result is a discontinuous CO_2 phase, with the CO_2 immobile within the pore space due to capillary forces and no longer a leakage threat [19, 20].

3. **Dissolution Trapping**: occurs as CO_2 is soluble in the formation brine, resulting in a denser CO_2/brine mixture. Consequentially the CO_2/brine slowly sinks further into the formation, storing the CO_2 more securely. The timescale for this process can be tens to hundreds of years due to natural aquifer flows [21].

4. **Mineral Trapping**: is the final process and occurs over the longest timescale (tens to thousands of years, or longer). In mineral trapping, the injected CO_2 dissolves into the in situ brine creating carbonic acid, which can react with minerals present within the geological formation, causing the precipitation of carbonates [22]. Therefore, it is a very

attractive trapping mechanism as it renders the CO_2 immobile for very long periods [23, 24].

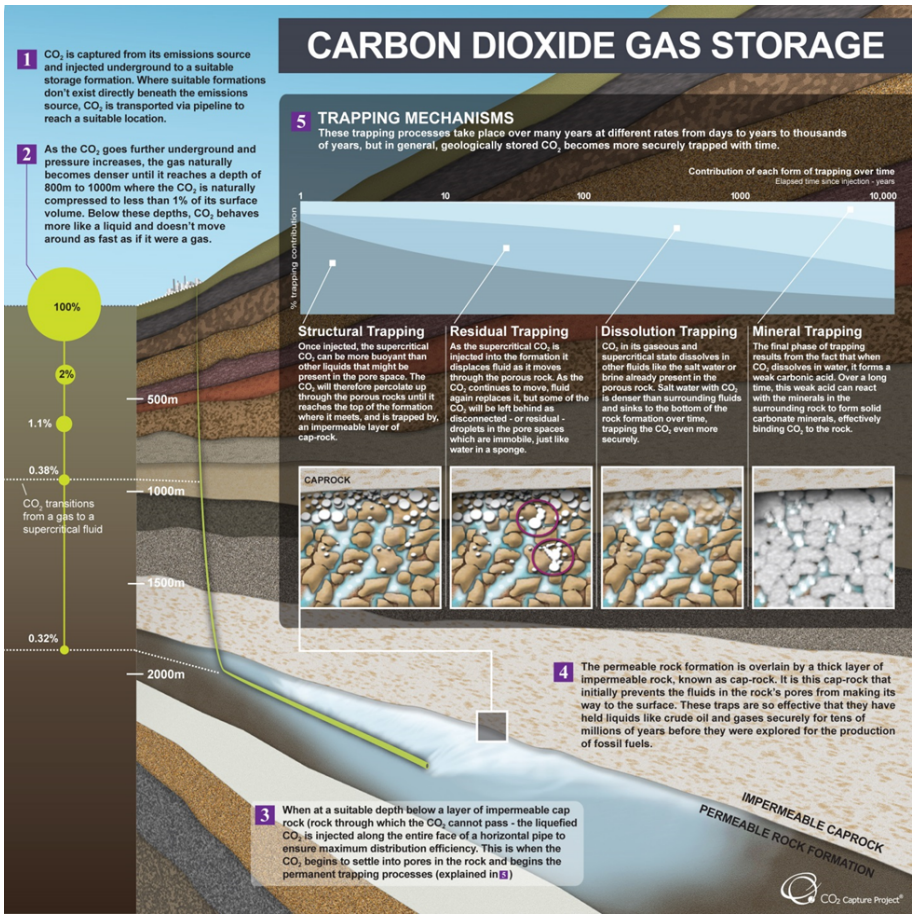


Figure 1.2.: Diagram illustrating the different geological storage mechanisms involved in carbon sequestration: structural (hydrodynamic), capillary (residual), dissolution and mineral trapping. Image courtesy of CO_2 Capture Project [3].

Of these trapping mechanisms, capillary trapping is of particular interest as is it does not wholly rely on the integrity of the cap-rock [19]. Instead trapping is achieved by capillary forces. Furthermore, it renders the injected CO_2 immobile over relatively short timescales [25–27]. However, its applicability in CCS needs to be further understood.

Indeed, one of the most crucial aspects of carbon sequestration is being able to predict how much CO_2 will be stored and where it will migrate to

over time. These predictions are very challenging for a number of reasons including the different geological and physical characteristics of different CCS sites and the time dependent wettability of the trapping rocks. In particular, supercritical CO_2 can alter migration pathways and storage potential [28, 29]. Work still needs to be conducted to improve the understanding of flow pathways chosen by injected CO_2. Current reservoir migration and storage predictions are usually calculated via reservoir simulators. The fundamental flow properties - including capillary pressure, residual saturation and relative permeability - which feed into these simulations, are generated by Pore Network Models (PNMs) [30–33]. However, for this to be computationally efficient, the real pore space needs to be simplified into a network of pores and throats.

1.3. Enhanced Oil Recovery

Approximately 80% of all global energy is produced via fossil fuels with the majority produced from mature fields [34–36]. There has been a concern for the past few decades about the ability to maintain and increase supply to meet demand [34–36]. However, a large amount of oil still remains in place after primary and secondary recovery processes have reached economic limits [37]. On average the amount of oil produced once primary and secondary recovery processes are no longer economical is roughly 35% of the original oil in place (OOIP) [35–38]. Therefore, maximising the recovery factor (RF) of a reservoir is a key goal for oil/energy companies.

To improve the RF, various Improved Oil Recovery (IOR) techniques can be employed, often referred to as tertiary recovery. Enhanced Oil Recovery (EOR) is a subset of IOR and increases recovery via either chemical, thermal, miscible flooding or other techniques such as microbial EOR. The RF can typically be increased by 5-15% and in some instances total field recovery can be greater than 70% when EOR techniques are implemented [35, 36].

One EOR approach is the use of surfactants which significantly lower the interfacial tension between the oil and brine phases. Once the critical capillary pressure immobilising the oil is exceeded the oil will be able to

flow, allowing for greater oil recovery. The typical oil recovery process is illustrated in Figure 1.3.

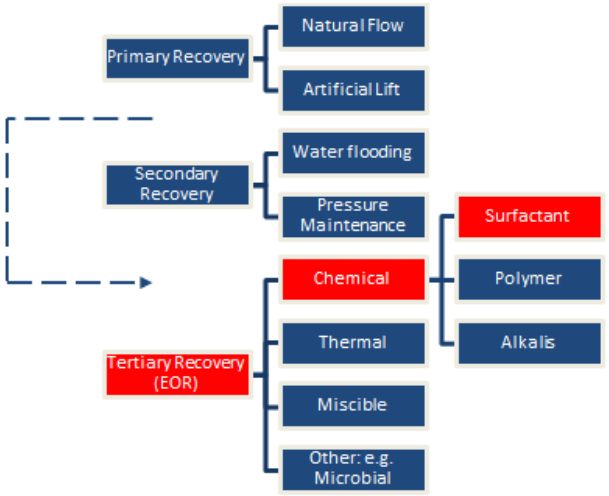


Figure 1.3.: Schematic of the typical oil recovery process. Once primary recovery is no longer viable, either secondary or tertiary recovery (EOR) procedures are applied. The red boxes illustrate the EOR process of interest for this thesis - Surfactant flooding.

In part of this study we will focus on surfactant flooding and present the preliminary results of Raman spectroscopy experiments designed to accurately identify separate phases within micro-models, as well as validating the suitability of this technique for future investigations.

1.4. Outline

Chapter 2 introduces the scientific background behind the work and is divided into three main sections:

- Section 2.1 covers the fundamental physical properties involved in multiphase flow (2.1.1), including Drainage and Imbibition (2.1.2), quasi-static displacement (2.1.3) and dynamics of multiphase flow (2.1.4).
- In Section 2.2 both surfactants (2.2.1) and micro-emulsions (2.2.2) and their importance to EOR applications are described.
- Finally, in Section 2.3 the applications of micro-models will be dis-

cussed. This will comprise of the history of micro-models (2.3.1), and current literature available on two-phase displacement processes for both carbon storage and EOR applications (2.3.2).

Chapter 3 is split into micro-model design (3.1) and fabrication (3.2) sections. The designs used in this study and their construction will be discussed. Section 3.3 outlines the general imaging techniques used throughout this work. More detailed experimental methodology will be given in the individual results chapters.

Chapters 4, 5, 6 and 7 will present the experimental results of this study; each chapter begins with an introduction before describing the experimental set-up and methodology in more detail followed by results and discussion. The results chapters are: Chapter 4 Rough capillaries, Chapter 5 Single Junctions, Chapter 6 Network Models and Chapter 7 Phase Identification using Raman Spectroscopy. Chapter 4 investigates the influence of roughness on the rate of imbibition conducted in two sets of capillaries with varying dimensions. Chapter 5 examines the fluid displacement pathway chosen during both drainage and imbibition in a single idealised pore with reference to the Young-Laplace law used to predict displacement pathways in PNMs. These results are compared to Lattice Boltzmann Method (LBM) simulations and analysis of different time-scales. Finally, in Chapter 7 the preliminary results from Raman spectroscopy experiments are presented which investigate the technique's effectiveness for phase identification with focus on surfactant EOR processes.

Chapter 8 will present the conclusions drawn from this work and discuss potential future work, including experimental investigations.

2. Background and Literature Review

The study of carbon storage and enhanced oil recovery (EOR) processes in rock formations requires investigation of multi-phase fluid systems. These systems can be comprised of two or more immiscible phases with distinct interfaces between them [39]. At the pore scale, capillary forces usually dominate. Therefore, understanding the fundamental physics of multiphase flow is vital. This chapter begins by introducing the basic physics influencing multiphase flow at the pore scale in Section 2.1. Drainage and imbibition and the possible displacement events possible will be discussed in Section 2.1.2. Sections 2.1.3 and 2.1.4 describe quasi-static and dynamic flow. Section 2.1.5 introduces the different computational methods used for investigating fluid flow in porous media – Pore Network Models (PNMs) and Lattice Boltzmann Method (LBM) simulations.

The use of surfactants to increase oil reservoir yield has been growing in popularity. The structure, properties and influence of surfactants will be discussed in Section 2.2.1. In particular, the interactions between surfactants and oil have been shown to lower the interfacial tension (IFT) of the system, producing micro-emulsions, consequently driving EOR. In Section 2.2.2 the concept of micro-emulsions will be developed in the context of EOR.

Section 2.3 examines the applications of micro-models for investigating fluid displacement processes at the pore scale. This includes a brief history of micro-models (2.3.1) and current literature on two-phase flow with regards to EOR and carbon sequestration applications (2.3.2). Finally, Section 2.4 will outline the motivation of this study.

2.1. Multiphase Flow

2.1.1. Fundamentals of Multiphase Flow

In many real-life systems, multiple fluids are involved. Whenever, two or more immiscible phases are present within a porous medium, distinct interfaces form between these immiscible phases, across which a pressure difference is present if the interfaces are curved [4]. For example, when considering a water/air system, three interfaces are present: (1) water – air, (2) water – solid, and (3) air – solid, see Figure 2.1. The interfacial tension (γ) between each phase is measured as a force per unit length or energy per unit area. The interfacial tension is therefore the energy (dW) required to increase the surface area by one unit. The work needed to create this additional surface area is proportional to the number of molecules which must be transported to the surface to increase the area (dA):

$$dW = \gamma dA \tag{2.1}$$

This results in an equilibrium configuration of the two fluids depending on the interfacial tension between the solid, liquid, and gas; denoted as s, l, g, respectively. At equilibrium the contact angle (θ), illustrated in Figure 2.1, is defined by Young's equation:

$$\gamma_{gl} \cos(\theta) = \gamma_{sg} - \gamma_{sl} \tag{2.2}$$

$$\cos(\theta) = \frac{\gamma_{sg} - \gamma_{sl}}{\gamma_{gl}} \tag{2.3}$$

where γ_{gl}, γ_{sg} and γ_{sl} are the interfacial tensions between the gas/liquid, solid/gas and solid/liquid interfaces respectively with the contact angle conventionally measured through the denser phase [4]. The LHS of equation 2.2 represents the adhesion tension and determines which fluid will preferentially wet the solid. If $\theta < 90°$, the fluid is described as the wetting phase (WP). Alternatively if $\theta > 90°$, the fluid is the non-wetting phase (NWP) and would like to have the smallest possible area in contact with the solid

surface.

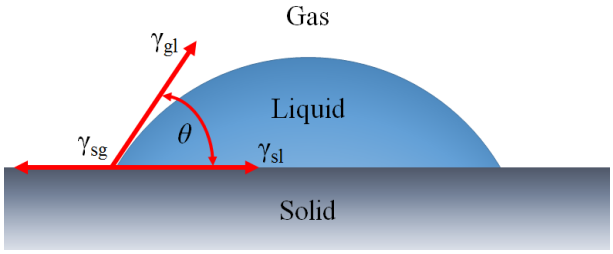


Figure 2.1.: Schematic of contact angle (θ) with the respective interfacial tensions: γ_{gl} (gas/liquid), γ_{sg} (solid/gas) and γ_{sl} (solid/liquid).

The capillary pressure across the interface between two immiscible phases can be calculated using the Young-Laplace equation:

$$P_C = P_{NW} - P_W, \tag{2.4}$$

where P_C is the capillary pressure, P_{NW} and P_W are the pressures of the non-wetting and wetting phases, respectively. When considering a porous medium, the local interface within a pore is curved to minimise the surface energy. As can be seen in Figure 2.2 there are two principal radii of curvature, r_1 and r_2, which are related to P_C (equation 2.5):

$$P_C = \gamma(\frac{1}{r_1} + \frac{1}{r_2}) = 2\frac{\gamma}{r^*}, \tag{2.5}$$

where r^* is the mean radius of curvature. Conceptually, capillary pressure can be used as a measure of the tendency of the WP to be *sucked* into the porous medium, or to repel the NWP. Within each pore P_C is dependent on γ and r^* and therefore the pore geometry is very important. Thus, variations in capillary pressure depend on the size of the pore and the nature of the phases.

Since in real porous media the pore spaces are very irregular, often idealised structures must be adopted to study the fundamentals. Furthermore, the processes which occur when the system is not in equilibrium (drainage and imbibition) can begin to be understood using simplified systems, such as capillary tubes. For example, when considering a single capillary tube,

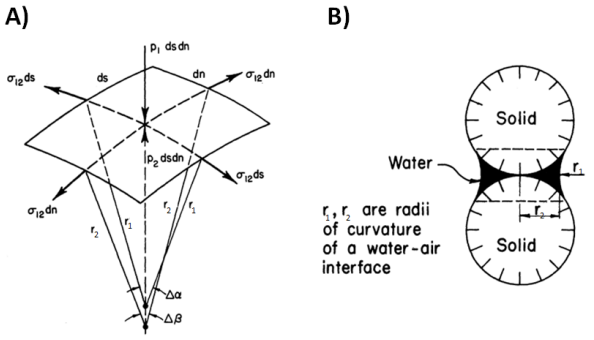


Figure 2.2.: Equilibrium at a curved interface between two immiscible fluids, modified from [4], p.445.

illustrated in Figure 2.3, the capillary pressure can be expressed in terms of principle radii of curvature.

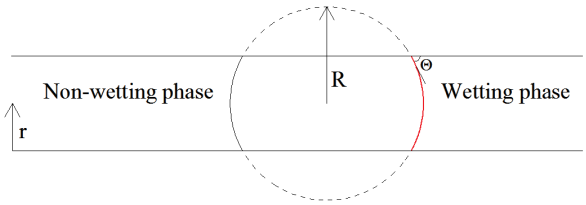


Figure 2.3.: Schematic of two immiscible fluids within a capillary tube of radius r, where the radius of curvature is $R = \frac{r}{cos(\theta)}$, where R is radius of a circle fitted to the curvature of the interface.

2.1.2. Drainage and Imbibition

Of particular importance for fluid migration and storage potential in porous media is the inverse relationship between capillary pressure and the saturation of the system. This relationship is demonstrated in the form of capillary pressure curves, with an example curve given in Figure 2.4. The shape of these curves is dependent on the displacement history of the system and is known as capillary hysteresis. Each curve represents a different displacement process, and depends on the initial saturation conditions of the porous media. In each case the phase initially present will be slowly displaced by the other phase.

As can be seen in Figure 2.4, during **drainage** the porous medium is

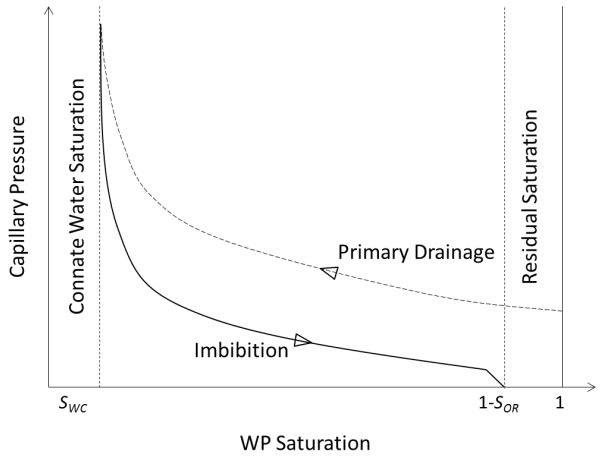


Figure 2.4.: Simplified drainage/imbibition capillary pressure curve - during primary and secondary drainage the capillary pressure systematically increases with increasing NWP saturation to connate water saturation (S_{WC}), whereas the capillary pressure decreases with increasing WP saturation during imbibition to residual saturation (S_{OR}).

initially saturated with WP before being displaced by the NWP. This requires an external force, such as gravity or a pressure gradient, to induce the displacement of the WP. In drainage, displacement events are only able to occur via piston-like displacement once the threshold pressure of a particular throat has been exceeded. The capillary pressure systematically increases with decreasing saturation, until connate water saturation (S_{WC} in Figure 2.4) is reached. From here the saturation will not decrease further even with increasing capillary pressure. The filling sequence during drainage therefore favours pore bodies/throats with the lowest capillary pressure, as these offer the path of least resistance.

Conversely, **imbibition** occurs when the NWP is replaced by the WP. Imbibition can either be spontaneous, driven by capillary forces, or forced, driven by external mechanisms. Here the capillary pressure decreases with increasing saturation, until the *residual saturation* level (S_{OR} in Figure 2.4) is reached. So following the Young-Laplace equation, it is expected that the WP will enter the narrowest downstream throat first, before sequentially filling all other throats in order of increasing diameter.

Both drainage and imbibition processes trigger displacement events to occur. These events can be complex and are dependent on various factors including pore geometry and location of both the WP and NWP within the porous medium. The individual displacement events which can occur can be divided into three main categories: piston-like, snap-off and pore body filling events, with the latter two only occurring during imbibition. Furthermore, during imbibition it is possible for a proportion of the NWP to become trapped by snap-off or by-passing of regions by piston-like displacement.

Piston-like displacement can occur during both drainage and imbibition. Both the WP and NWP are present within the throat, with the WP located in the corners of the throat, see Figure 2.5 A. For piston-like displacement to occur during drainage, the NWP pressure (P_{NW}) must be equal to or greater than that of the WP (P_W). Once the critical pressure ($P_C = P_{NW} - P_W$) is overcome, the NWP may enter the throat. Piston-like displacement is a reversible process and is dependent on throat dimensions.

Snap-off occurs only during imbibition. A snap-off event can occur anywhere within the porous medium ahead of the advancing WP front. This is possible as WP films can develop in the corners of the porous medium, (see Figure 2.5 A), and advance ahead of the main imbibing front. Snap-off happens when these films become unstable and come together causing a throat to become filled with WP, (see Figure 2.5 B). To calculate the critical snap-off pressure (P_S) the following equation is used:

$$P_S = \frac{\gamma}{r}(\cos\theta - \sin\theta), \tag{2.6}$$

Pore Body Filling events in imbibition are dependent on the number of throats connected to the pore that are filled with NWP. This is because the capillary entry pressure for a pore body is limited to the largest radius of curvature that can be achieved. Therefore, the number of throats filled with WP along with location is important. In general, pore-filling events are designated as I1, I2, I3....In, where n is the number of throats filled with the NWP [8]. Figure 2.6 illustrates the possible pore body filling events for a pore with a coordination number of four; the NWP is represented in grey.

The processes of drainage and imbibition are therefore complicated and

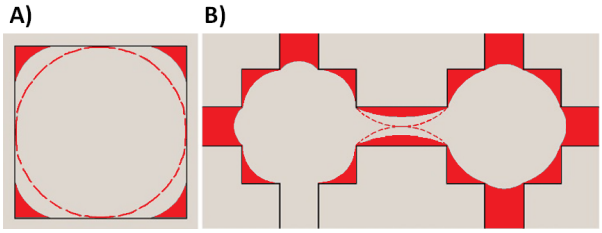


Figure 2.5.: Schematic diagram of snap-off mechanism which can occur during imbibition. Here the WP is shown in red. The WP films swell and eventually become unstable at critical meniscus position illustrated by the red dashed line.

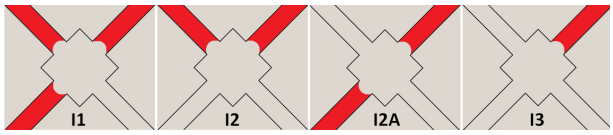


Figure 2.6.: I1 – I3 pore body filling events, WP shown in red.

determined through a variety of different variables. Indeed, both pore scale and macroscopic properties impact on the capillary trapping curve which results from these processes. Therefore, establishing the influence of these parameters is imperative. This is true for both experiments and predictive models, including PNMs and LBM simulations, which are used to calculate the parameters used in reservoir simulations. These in turn are used to predict the migration pathways and storage potential of possible carbon sequestration sites.

2.1.3. Quasi-static Displacement

Many models assume that the displacement processes can be simplified by assuming the flow is quasi-static. The quasi-static approximation assumes that the system changes sufficiently slowly such that it remains constantly in equilibrium. In the case of PNMs, the displacement processes are governed by the Young-Laplace equation with quasi-static pressure steps. PNMs usually assume that flow is capillary dominated and that viscous forces and gravity do not affect flow at the pore scale. Furthermore, the quasi-static approximation appears relevant to displacement processes occurring

in the far field during CO_2 storage and EOR operations, associated with low Reynolds (Re is the ratio of inertial to viscous forces), Bond (Bo is the ratio of gravity to viscous forces) and Capillary (Ca is the ratio of IFT to viscous forces) numbers.

Drainage processes are achieved in PNMs by increasing the pressure of the oil phase, whilst the WP pressure remains the same. This results in an overall increase of the capillary pressure within the network. During each incremental change in pressure, filling events which are possible will occur anywhere within the model. All interfaces are kept static within the network, apart from a single displacement event or cascade of events. This process will continue until either a predefined saturation is reached or all pores and throats have been filled with NWP.

For **imbibition**, more displacement processes are possible than during drainage. These additional displacement events are influenced by the presence of WP films. In PNMs, three shapes are used to represent the pore space – cylindrical, triangular and square cross-sections, which are discussed further in Section 2.1.5. Within the triangular and square cross-sectional pores, WP films are considered always present and connected after drainage.

2.1.4. Dynamics of Multiphase Flow

In addition to understanding the basic fundamental quasi-static conditions, in real systems dynamic processes are also important. These are relevant to both drainage and imbibition transport processes occurring near the well bore at relatively high Re and Ca. This section will discuss the basis of capillary filling dynamics within a single capillary.

The pioneering work of Lucas and Washburn [40], nearly a century ago, established that the distance travelled by the fluid interface within a capillary was proportional to the square root of time for a sufficiently high viscosity ratio ($rn = \eta_w/\eta_{nw}$). By assuming that the capillary and friction forces are balanced, [41–46] the well-known Lucas-Washburn equation can be derived:

$$l^2 = \frac{\gamma w \cos\theta^a}{3\eta_w}(t + t_0), \tag{2.7}$$

where l is the distance the meniscus has travelled into the capillary, w is the width of the capillary, θ^a is the advancing dynamic contact angle, η is the viscosity of the fluid and t is the time.

While the Lucas-Washburn equation has become the foundation of capillary phenomena, several modifications have been generated following the original equation. Early modifications were performed by Rideal [47] and Bosanquet [48] by introducing an inertial term relating to the mass/acceleration of the liquid, respectively. Subsequently, Szekely *et al.* [49] developed the equation further by considering the effect of the inlet length. A thorough analysis of the development in capillary rise in circular capillaries is given by Stange *et al.* [50], who conclude that a comprehensive theory of capillary filling was still missing. Even though different effects have been outlined, a systematic investigation of their importance has not been conducted [50].

However, cylindrical capillaries are generally not a realistic representation of actual porous media. Therefore, work has also been done relating to irregularly shaped capillaries. Mason and Morrow [51] used a theoretical approach to investigate capillary behaviour of a perfectly wetting fluid within a capillary with a triangular cross-section. They found that both the wetting and non-wetting phase could be simultaneously present within the pore, meaning that there is a possibility of imbibition occurring during the drainage processes, although it would be very slow. This is also true for capillaries with a rectangular cross-section, which have been used in this thesis. In rectangular capillaries, the characteristic length is the hydraulic radius ($R_H = \frac{r_1 r_2}{(r_1+r_2)}$) . Knowing that the WP and NWP can be present simultaneously within a capillary is important for understanding the displacement processes; this means that mechanisms normally limited to imbibition, such as snap-off, can also occur during drainage.

From dimensional analysis, the dynamics of capillary filling depends on two characteristic time-scales:

1. $t_1 \sim \sqrt{\frac{\rho R_H^3}{\gamma}}$, where ρ is the density of the fluid, which is related to the initial settling phenomena and the reorientation of the interface of the

meniscus at the inlet of the capillary.

2. $t_2 \sim \frac{\rho R_H^2}{\eta_W}$, which is the viscous time-scale. This roughly determines the crossover between the initial inertial regime and the viscous regime (i.e. the Lucas-Washburn regime) for t $\gg$ t_2.

These time-scales can be used to determine the Ohnesorge number (Oh), which relates viscous to inertial forces and surface tension. It is known as a damping measure for capillary dominated oscillations. The Oh can be described as the ratio between the two time-scales:

$$Oh = \frac{\eta_W}{\sqrt{\rho \gamma R_H}} = \frac{t_1}{t_2}, \tag{2.8}$$

Therefore, depending on Oh and the relative magnitude of experimental times compared to t_1 and t_2, three successive length vs time ($l - t$) regimes can be obtained [41, 50]:

1. $l \sim t^2$ for $t \ll t_1$ - Inertial regime;
2. $l \sim t$ for $t_1 < t < t_2$ - Visco-inertial regime;
3. $l \sim t^{0.5}$ for $t \geq t_2$ - Lucas-Washburn regime.

If the Oh number is decreased – by increasing the system size (R_H) – t_2 will increase first and the linear regime will precede the $l \sim t^{0.5}$ regime. For even smaller Oh numbers, t_1 will also increase which leads to an initial $l \sim t^2$ dependency.

Another important consideration for flow dynamics is establishing whether laboratory flow conditions are representative of subsurface conditions. The Ca measures the ratio of viscous to capillary forces and is conventionally defined as: $Ca = \frac{v\eta}{\gamma}$, where v is the velocity of the fluid. When considering Ca at the pore scale, a value of 10^{-3} or smaller is used in experiments as the viscous and capillary pressure drops are of the same magnitude [52].

In the case of dynamic imbibition processes, the competition between pore and throat filling controls the final amount of NWP trapped.

2.1.5. Computational Methods

For predicting fluid migration at the field scale, modelling fluid flow is necessary. This can be achieved by using computational simulations such as PNMs or the LBMs. These can be used to predict fundamental flow properties including capillary pressure and relative permeability, which are then used in reservoir simulators for field scale predictions.

PNMs can be used to simulate both single- and multiphase fluid flow in porous media [30, 33, 53–55]. The simulations are based on simplified models of the pore space geometry as the complexity of actual porous media cannot be modelled at a scale representative of the real rock's macroscopic behaviour.

Original PNMs were based on a regular lattice of connected pores and throats which were not representative of real porous media. One important parameter is the number of throats surrounding each pore – or coordination number – which is known to have a significant effect on the behaviour of the network model [33]. Therefore, PNMs were improved to include such parameters and thus be more representative of porous media [33]. However, due to the highly irregular nature of porous media, it is not feasible to represent the pore space geometry exactly. Instead a topologically equivalent network is created, in which properties, including radius and volume, are extracted from the original voxel representation [56]. The individual elements of the network (pores and throats) are uniform ducts of circular, square or triangular cross-sectional shapes, shown in Figure 2.7. These all have the same shape factor (G) [51] as the voxel representation:

$$G = \frac{A}{P^2}, \tag{2.9}$$

where A is the cross-sectional area and P is the perimeter.

A high shape factor will be represented by a circular cross-section, the more irregular the pore the lower the shape factor. Within PNMs, WP films in square and triangular pores can be clearly modelled. The presence of WP films is very important during imbibition and is necessary for snap-off to occur, which is described in Section 2.1.2.

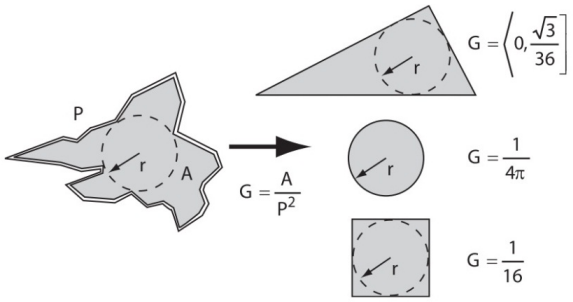


Figure 2.7.: Schematic of the cross-sectional shapes - circular, triangular and square - used as the network elements within PNMs [5].

PNMs operate in a quasi-static fashion meaning that the flow is capillary dominated and therefore the viscous pressure drops are considered insignificant [56]. At each pressure step, the displacement events are calculated until hydrostatic equilibrium is achieved. The PNM will then progress to the next pressure step.

The limitations of PNMs lie in the simplifications which are applied for computational efficiency. This includes simplifying both the geometries, for single-phase simulations, and the underlying physics, for multiphase flow predictions [57]. Meakin and Tartakovsky [54] state that the value of PNM simulations is limited by these simplifications and thus provide only partial insight into the detailed physics and chemistry of the wetting phenomena can be extracted. Additional parameters - such as the contact angle - also need to be provided which may be acquired either experimentally [8] or via other computational methods [57].

LBM simulations [58–61] are a type of Computational Fluid Dynamics (CFD) simulations. The LBM was chosen over other CFD algorithms due to its ability to handle complex solid geometries [62] and liquid-liquid boundaries without simplification [63]. Thus, they differ from PNMs in their ability to calculate flow properties directly on the pore space images without the need of simplification. Additionally, local computation allows efficient parallel implementation. This makes LBM an ideal numerical tool for the study of pore scale flow properties in porous media. Here an extension of the LBM known as the free energy lattice Boltzmann method, first introduced by Swift *et al.* [64, 65], is used to simulate two-phase flow in

micro-models. A Multiple-Relaxation-Time collision scheme has also been employed to improve numerical stability [66] and permit higher viscosity ratios and lower capillary numbers than other multi-phase LBM models. For further detail, see the review of Crawshaw and Boek which outlines the development and applications of LBM simulations [57].

All of the LBM simulation results presented here have been conducted by either Jianhui Yang (former PhD student) or Ioannis Zacharoudiou (Post-Doc).

2.2. Surfactants and Micro-emulsions

Understanding how and where surfactants migrate in porous media flow is vital. Beyond the scientific interest, it would also allow more cost efficient surfactant injection to the subsurface, which has often been considered prohibitively expensive. The objective is to inject the minimum amount of surfactant possible whilst still achieving the best sweep efficiency and avoiding losses due to adsorption on the reservoir rock surface and surfactant stability during injection. Of particular importance are the spatial distribution of the injected surfactants and the resulting phase behaviour such as micro-emulsion formation in ultra-low IFT systems. This work further develops the capability for such characterization using Raman spectroscopy.

2.2.1. Surfactants

Surfactants (contraction of **surf**ace-**act**ive **a**ge**nts**) generally are organic, amphiphilic molecules. Their chemical structure contains both a hydrophilic ("water attracting") head group and a hydrophobic ("water repelling") tail group, as shown in Figure 2.8 [6, 67–69]. Their dual nature makes surfactants versatile products with applications including: detergents, cosmetics, pharmaceuticals, paints, adhesives and EOR [68]. One of the main advantages of surfactants is that they will preferentially adsorb at interfaces - where the hydrophilic head remains within the solvent (such as water), whilst the hydrophobic tail sticks out into the oil phase, Figure 2.8. This induces noticeable changes in physical properties, for example, by signifi-

cantly lowering γ [67, 68].

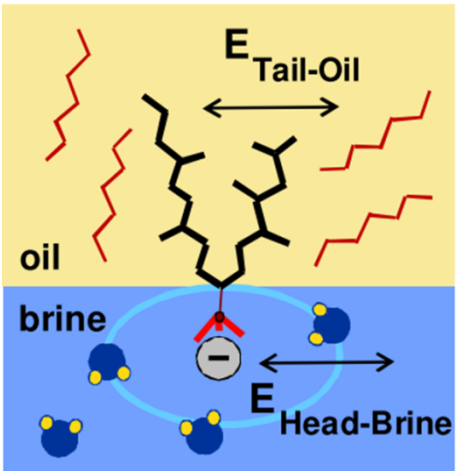


Figure 2.8.: Schematic illustrating the chemical structure of an anionic surfactant molecule. The hydrophilic head group is located within the solvent (most commonly water), whilst the hydrophobic tail sticks out into the oil phase [6].

The practice of adding surfactants to reduce the IFT between oil and brine is not a recent development, in fact, initial interest began as early as 1927 [70]. It has been shown to be beneficial for EOR [71]. At the end of primary or secondary oil recovery, often a large amount of oil remains trapped in the reservoir (in the range 40 % to 70 %) due to competing capillary and viscous forces. This is often quantified with the capillary number (Ca). Here the Ca of the flowing formation brine is high, whilst the Ca of the trapped oil is zero. The trapped oil will be mobilised once a critical Ca is exceeded. To overcome this barrier and increase Ca, the IFT between the oil and brine may be significantly lowered [12]. This can be achieved by the addition of surfactants to the system [6, 12, 67, 71, 72], which mobilises the trapped oil increasing the recovery factor. The trapped oil is able to flow as decreasing the IFT in turn reduces the opposing capillary forces [73, 74].

Significant research has focused in this area and it is well known that to mobilise residual oil the IFT needs to be reduced from the typical oil/brine values of between 20-50 mN/m by several orders of magnitude to below 0.01 mN/m [6, 71]. In order to achieve these ultra-low IFT values, the selected surfactant must be tailored for each individual reservoir [12, 72]. The opti-

mum conditions are ascertained by systematic laboratory tests, as discussed below. Furthermore, there are different surfactants available which are classified based on the ionic nature of their head group: anionic, cationic, non-ionic and zwitterionic [68, 69, 75]. Each of these surfactant families possess different benefits, although this study will focus on anionic surfactants [72]. Anionic surfactants are the most widely used in chemical EOR processes as they have been shown to provide the best performance/cost profile [72]. The most commonly used anionic surfactants are: carboxylates, sulphates, sulphonates and phosphates [74, 75]. In this thesis, sulphonates were considered for a number of reasons: reduced tendency to form ordered structures, good stability over a range of conditions, availability of raw materials, easy production and low cost [71, 76]. Further discussion on sulphonate surfactants will be presented in Chapter 7.

Therefore, the ability of surfactants to achieve ultra-low IFT values is essential in EOR. To anticipate the effects of surfactants, Winsor proposed a simple concept - the ratio of the attractive energy terms on either side of the interface, known as the Winsor Ratio (WR) [77]:

$$WR = \frac{E_{Tail-Oil}}{E_{Head-Brine}}, \tag{2.10}$$

where $E_{Tail-Oil}$ and $E_{Head-Brine}$ are the energy terms for the tail-oil and head-brine interfaces respectively. To achieve ultra-low IFT values the energies on either side of the interface should be large and equal in magnitude, leading to $WR = 1$. The system can be fine-tuned to achieve ultra-low IFT values. Section 2.2.2 will present more details on achieving the optimum conditions for anionic surfactants and the formation of micro-emulsions.

2.2.2. Micro-emulsions

One of the most important properties of surfactants is their ability to form micro-emulsions. It was only after the work of Hoar and Schluman in 1943 [78] - in which they reported the formation of a spontaneous emulsion of water and oil after the addition of a surfactant – that micro-emulsions gained more recognition. However, it would be more than another decade before the term “micro-emulsion” was introduced by Schulman *et al.* in 1959 [79].

The term was used to describe a multiphase system containing water/oil/-surfactant and an alcohol, which had formed a transparent solution [79]. Danielsson and Lindman [80] succinctly described micro-emulsions as:

"... a system of water, oil and an amphiphile which is a single optically isotropic and thermodynamically stable liquid solution."

The formation of a micro-emulsion is only possible when the interfacial tension is ultra-low. Conceptually this can be explained by considering the subdivision of the dispersed phase into much smaller droplets as shown in Figure 2.9 [81].

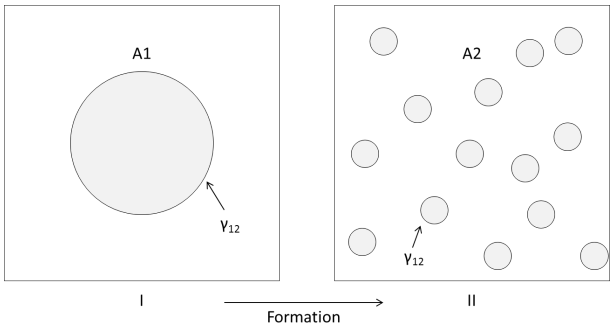


Figure 2.9.: Schematic of micro-emulsion formation. IFT decreases from I to II with the subdivision of the dispersed phase into much smaller droplets. This leads to an increase of surface area, surface energy and entropy assuming IFT and T remain constant.

In Figure 2.9, $A1$ is the surface area of the bulk dispersed phase, $A2$ is the total surface area of all the micro-emulsion droplets and γ_{12} is the interfacial tension between the phases. Therefore, when moving from state I to II, there is an increase in surface area ($\Delta A = A2 - A1$), surface energy assuming the IFT is constant (equal to $\Delta A\gamma_{12}$) and entropy ($T\Delta S$), at constant temperature T.

The free energy of formation of micro-emulsions, ΔG_M, can be described according to the second law of thermodynamics:

$$\Delta G_M = \Delta A\gamma_{12} - T\Delta S. \tag{2.11}$$

Therefore, as the number of droplets increases then ΔS is positive. If

the chosen surfactant is able to lower the IFT to ultra-low values, then the energy term $\Delta A\gamma_{12}$ may become small enough (being positive due to the increase in surface area), resulting in a negative free energy change ($\Delta G_M < 0$). Thus, the micro-emulsion will form spontaneously and be thermodynamically stable.

There is a well-known classification of micro-emulsions by Winsor, who identified four general types of micro-emulsions, known as Winsor types I – IV [77]:

- **Winsor I (o/w)** – forms an oil-in-water micro-emulsion since the surfactant is preferentially soluble in water. It consists of a surfactant-rich water phase and an oil rich (surfactant poor) phase.
- **Winsor II (w/o)** – forms a water-in-oil micro-emulsion. Here the surfactant is predominantly in the surfactant-rich oil phase and coexists with the surfactant-poor water phase.
- **Winsor III (middle phase micro-emulsion)** – instead produces a three-phase system, in which there is a surfactant-rich middle-phase that coexists with surfactant poor -water and -oil phases.
- **Winsor IV** – is a single homogeneous phase.

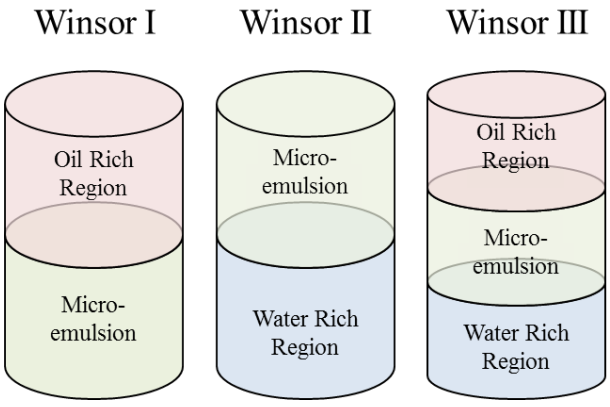


Figure 2.10.: Schematic of Winsor type micro-emulsions. Winsor I – oil-in-water micro-emulsion, Winsor II – water-in-oil micro-emulsion, Winsor III – middle phase micro-emulsion.

Figure 2.10 illustrates Winsor I – III micro-emulsions. Winsor III is of most interest as it indicates that ultra-low IFT values have been achieved.

Salt, such as sodium chloride (NaCl), acts as a shield on the head group of the surfactant. Therefore, the salinity of the reservoir must be considered to achieve optimum conditions [6].

It is necessary to perform systematic tests to determine the optimum surfactant solution relating to the reservoir of interest. These tests are performed in the laboratory by mixing surfactant solution with an oil phase [12, 72, 75]. Anionic surfactants need to be tuned based on the salinity of the in-situ brine of the reservoir of interest. An increase in salinity causes the following transition: Winsor I – Winsor III – Winsor II at a particular temperature and pressure [79]. If the salinity is too low, the result will be an "under-optimum" oil-in-water emulsion. Equally, if the salinity is too high, the outcome will be an "over-optimum" water-in-oil emulsion. At the optimum salinity, the minimum IFT is reached, resulting in higher recovery factor [79].

These ultra-low IFT values are best for oil recovery as the capillary number of the system is increased at reservoir flow rates, thus capillary forces can be overcome by viscous forces enabling previously trapped oil to flow. The appearance of the middle phase, Winsor III micro-emulsion, is dependent on the amount of water, oil and surfactant present [82]. Additionally, the volume of micro-emulsion created is proportional to the surfactant concentration [82]. For surfactant EOR floods to be most successful, understanding the spatial distribution of the phases is preferential. Therefore, the ability to observe migration of injected surfactant solutions and the in-situ formation of a micro-emulsions phase is of great interest.

2.3. Applications of Micro-models

The field of micro-fluidics has been growing over the past 50 years and can be defined as:

... the study of flows that are simple or complex, mono- or multiphasic, which are circulating in artificial microsystems... [83]

The applications for micro-fluidic devices are vast and span multiple fields, including chemistry, biology, biomedicine and geology [83]. The implemen-

tation of micro-models has increased over the past several decades, especially with regard to visualising subsurface processes relating to EOR and carbon sequestration processes. This has come about particularly as understanding migration pathways occurring subsurface is of great importance for both improving recovery and demonstrating secure storage. Unfortunately, at present, direct visualisation of subsurface fluid displacement processes is challenging, requiring the use of either medical- or micro-CT scanners. However, these techniques are not able to capture displacement processes in real time using lab scale benchtop scanners. The use of a synchrotron provides a better time resolution but is still complex. Therefore, the use of micro-models offers an attractive alternative for real time imaging. This is especially the case as it is possible to create optically transparent micro-models on the pore scale. Hassanizadeh has defined micro-models used for investigating flow in porous media as [84]:

"... an idealized, usually two-dimensional representation of a porous medium—a network of connected pores, measuring in the (tens of) microns, through which fluids flow and solutes spread... Accordingly, a micromodel is typically made of a transparent material that enables visual observation, such as glass or quartz, but it could be polymeric. The requirement of small pores (< 1 mm) is essential for two-phase flow studies because capillary effects will be otherwise irrelevant."

Furthermore, as micro-models are a synthetic system, the user has a significant amount of control on the final model, including geometry and model characteristics – such as surface energy and roughness – allowing specific questions to be addressed and the influence of individual aspects on fluid displacement to be discovered.

2.3.1. History of Micro-models

Over the decades, the techniques used to fabricate micro-models have improved considerably. Improving technology and the advances in imaging rock sections has enabled micro-model designs to become increasingly representative of real porous media. Below is a brief description of the progression of micro-models.

The first micro-scale observations were conducted by Chatenever and Calhoun [85], whose aim was to explore the possibility of a visual approach in investigating microscopic mechanisms for fluid behaviour in porous media. They fabricated 'observation flow cells' which consisted of a single layer of glass spheres sandwiched between two flat plates, also known as a glass bead/sphere pack. The packing of the glass beads within the model resulted in an approximately rhombic pattern. They found that multi-layered cells were not suitable due to the difficulties in differentiating one phase from another. Additionally, as the pore space itself is complex, understanding observed flow phenomena is extremely complicated.

Since analysing flow phenomena within a bead pack is very difficult, Fatt *et al.* [7] proposed a two-dimensional regular network of glass cylindrical tubes with randomly distributed radii. Four different regular networks were investigated: single hexagonal, square, double hexagonal and triple hexagonal, all are shown in Figure 2.11.

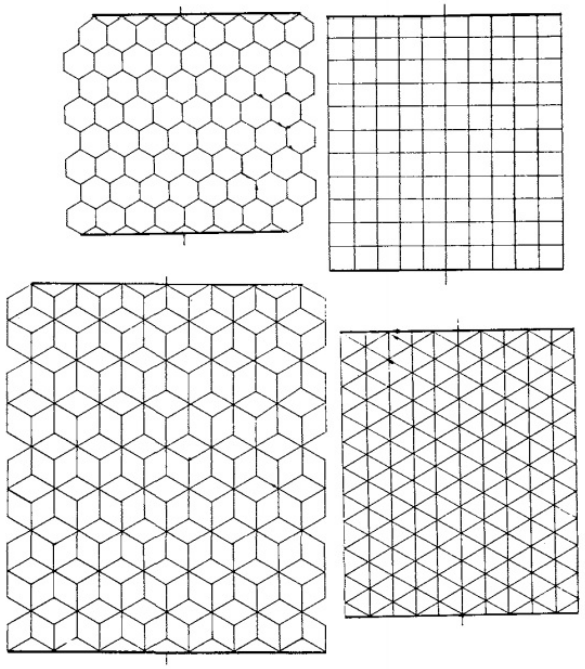


Figure 2.11.: Regular two-dimensional networks of cylindrical tubes used by Fatt *et al.* [7] to improve visualisation of flow phenomena.

The first etched glass micro-model was fabricated by Mattax and Kyte in

1961 [86], in order to capture fluid interface motion in more detail. The micro-model consisted of a network of interconnecting capillary grooves etched into a glass plate. These v-shaped grooves were achieved by coating a glass plate with a thin layer of wax into which the pattern was inscribed using a stylus. The exposed glass was then treated with hydrofluoric acid (HF) for between 1 to 3 minutes to etch the pattern into the glass. Next, the wax was removed and a second glass plate fused to the first in an annealing oven. Finally, holes were drilled through the fused glass penetrating into the capillary network.

This technique was improved upon by Davis and Jones [87], who replaced the wax which limited the designs which could be fabricated, with photoresist. This meant that any black and white pattern could be etched into the glass plate.

The methodology for fabricating etched glass micro-models was refined by McKellar and Wardlaw [88] and is still currently used. Their refinement was the addition of an intermediate layer of copper-silver between the photoresist and the glass plate. This was beneficial as copper-silver is resistant to HF, yet easily removed by other solvents. Furthermore, the photoresist is still able to bond easily to the copper-silver layer. The copper or silver layer can either be directly applied to the glass plate, or instead a piece of mirror can be used once the backing has been removed, revealing the copper/silver layer. The general steps are outlined below [88]:

1. A piece of mirror is cut to the desired size and the backing is removed via a hot sodium hydroxide solution;
2. The mirror is examined microscopically for imperfections in the copper-silver coating before an even layer of resist is applied;
3. A negative transparency of the desired flow pattern is positioned on the glass plate and exposed to ultra-violet (UV) light;
4. The pattern is developed – at this stage portions of the model which need to be etched away are bare glass, whilst those that do not still have copper-silver and resist coatings;
5. HF is used to etch the pattern into the glass;

6. Any remaining resist is removed;
7. The model is then placed in a solution of 50 % nitric acid to remove the copper-silver coating and rinsed with deionized (DI) water;
8. Second glass plate is fused to create micro-model.

In 1983 Lenormand *et al.* [8] advanced the micro-fluidics field with the fabrication of a resin micro-model, which are less difficult to manufacture. Previous experiments had been hindered by a number of factors: poor visualisation on the pore scale and intricate interfaces observed in bead packs meaning data interpretation was difficult. Ill-defined throats were also a problem with chemical etching, in addition to cover plate adhering problems which could result in WP entering the gap between the plates. Therefore, the resin moulding technique resulted in throats of rectangular cross-section that were beneficial for both observation and analysis, see Figure 2.12.

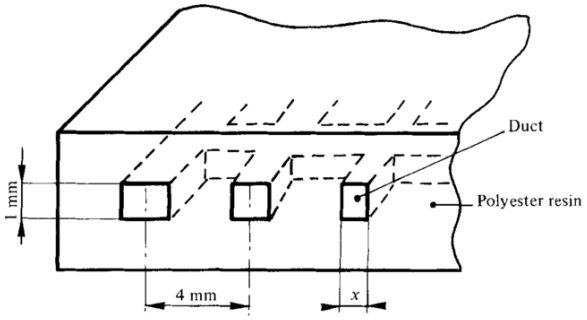


Figure 2.12.: Schematic cross-section of the network used by Lenormand *et al.* [8].

In order to improve micro-model dimensions, Hornbrook *et al.* [89] fabricated the first silicon micro-model to produce an almost exact two-dimensional replica of porous media, in their case a Berea sandstone. This technique is still used today and a more detailed description is given in Section 3.2.

More complex **'Network'** designs have also been investigated within micro-models. Here the designs can range from very simple homogeneous designs to those which are based on rock thin sections. However, due to the 2.5 D nature of the models not all characteristics can be matched perfectly, such as porosity and permeability. Furthermore, the uniform etch depth of

micro-models limits the possible capillary pressure values.

In this thesis a range of micro-models has been used - glass, Poly(methyl methacrylate) (PMMA) and silicon/glass. More details on the design and fabrication process for all the models used are given in Chapter 3.

2.3.2. Displacement Processes within Micro-models

Single capillaries are the simplest micro-models which provide an idealised system to observe fluid dynamics. Significant work has been carried out on the subject of filling dynamics in a single capillary.

Beyond the theoretical developments discussed in Section 2.1.4, there have been numerous experimental studies of pore scale fluid behaviour. Indeed, the behaviour predicted by Lucas-Washburn had been previously observed by Bell and Cameron in earlier experiments [90].

The experimental studies which have been conducted on the different aspects of capillary filling are detailed below. Early experiments conducted using small diameter capillaries, observed $l \sim t^{0.5}$ behaviour (Lucas-Washburn regime) at small time scales [40, 90]. Furthermore, Tas *et al.* [91] reported experiments on the capillary filling speed of water in nanochannels. They observed that the measured position of the meniscus followed square root of time behaviour, in agreement with the Lucas-Washburn equation. However, the most extensive research has been done investigating the initial stages of capillary filling [41–46]. This is because many authors agree that while the Lucas-Washburn regime is the asymptotic limit for large times, where all influences cease to exist apart from the capillary force and viscous drag, at initial stages other forces can dominate [41–46].

Other factors experimentally investigated include dynamic contact angle [46, 92–95] - the moving contact angle, either advancing or receding. The dynamic advancing contact angle is expected to be greater than the equilibrium contact angle [96]. Therefore, with a better constraint on contact angle, the agreement between position of the meniscus with time observed experimentally and the Lucas-Washburn equation should be improved. In addition to the contact angle, the 'roughness' of the capillary walls has also been investigated and its effect on contact angle [97–101]. However, it is

poorly understood how surface roughness of the capillary influences the rate of imbibition. This is of great importance for flow in porous media applications. Therefore, this thesis has considered the meniscus penetration within a series of single capillaries of increasing surface roughness.

Furthermore, different simulation techniques have also been used to investigate different aspects of capillary filling. Dimitrov *et al.* [102] used Molecular Dynamic (MD) simulations to investigate capillary rise in nanopores. MD simulations were also used by Stukan *et al.* [103] to study the effect of wettability and roughness on the rate of spontaneous imbibition. They show that increasing roughness causes the velocity of the meniscus to slow down. Alternatively, LBM simulations have been used by Diotallevi *et al.* [104] to research the effect of density, whilst Pooley *et al.* [105] observed that the correct scaling behaviour is recovered when the viscosity ratio between the two fluids is sufficiently high.

Some of the most fundamental research conducted on immiscible flow within micro-models is that of Lenormand *et al.* [8], who investigated fluid displacement processes within a simple resin etched micro-model of rectangular throats. Since then numerous fluid flow experiments have been conducted within micro-models investigating immiscible flow systems [85, 106–114]. Individual displacement processes have also been investigated including drainage/imbibition and viscous or capillary fingering [8, 84, 86, 106–109, 111, 113–121].

However, none have investigated fluid displacement mechanisms within a micro-model of a single pore where the fluid in each connected throat can be controlled directly. In this study both quasi-static and dynamic displacement pathways will be investigated within a single pore.

Network micro-models have also been used for the study of EOR processes at the pore scale. These processes include polymer, surfactant and microbial flooding, in order to displace oil towards the production well. However, the success of EOR operations is dependent on multiple factors including the physical properties of each phase and reservoir conditions, which can vary significantly. These include capillary number, temperature and flow dynamics which have been studied in a variety of papers [84, 89, 122–135].

Some work has been conducted into surfactant flooding using micro-

models. Jamaloei and Kharrat [136] investigated displacement mechanism of dilute surfactant flooding in both oil- and water-wet glass micro-models. They found that after water- and surfactant-flooding the final oil recovery value was greater in the water-wet model than in the oil-wet model.

In this work, the effect of surfactants has been considered via micro-model experiments, allowing direct visualization of the pore space. Traditionally, an in-depth phase analysis has not been possible as identifying individual phases is difficult. This is especially true for surfactant studies due to the formation of micro-emulsions. This is where Raman spectroscopy has significant advantages for micro-model EOR applications as it allows spatially resolved composition measurements.

2.4. Motivation

Micro-fluidic devices can be used to investigate a wide range of applications from different fields. The research presented in this thesis focuses on multiphase flow phenomena at the pore scale with respect to carbon sequestration and EOR. To achieve this, a range of micro-models (PMMA, glass and silicon/glass) have been designed and used with the aim of investigating the underlying fundamental physical displacement processes occurring at the pore scale.

The specific objectives of this research are:

1. Design multiple sets of micro-models to investigate displacement mechanisms at varying system sizes: from a single pore to a complex network;
2. Investigate the influence of pore geometry on fluid displacement processes with respect to the Young-Laplace equation;
3. Investigate the role of roughness on the rate of spontaneous imbibition within a single capillary with respect to the Lucas-Washburn equation;
4. Investigate the use of Raman spectroscopy for phase identification with regards to surfactant flooding for EOR.

3. Micro-model Fabrication and Imaging Techniques

Micro-fluidic experiments reveal fluid displacement mechanisms in confined geometries. In this thesis, four variations of micro-fluidic experiments have been conducted using a range of micro-fluidic devices from single capillaries to complex networks. The aim of the experiments was to investigate fundamental displacement mechanisms in comparison with predictions from the Lucas-Washburn and Young-Laplace laws. For the phase identification experiments, a novel approach was taken using Raman Spectroscopy to probe micro-fluidic devices in order to identify phases for surfactant enhanced oil recovery (EOR) applications.

All the experiments utilise micro-fluidic models in order to visualise events occurring at the pore scale in real time. In this chapter the different micro-model designs (3.1) used in this thesis will be presented and their designs explained. The general fabrication procedures for Poly(methyl methacrylate) (PMMA), glass and silicon/glass micro-models will be discussed in (3.2). Lastly, Section 3.3 describes the main imaging techniques used in this study.

3.1. Micro-model Design

The designs of micro-models can range from simple straight capillaries to complex designs which are based on real porous media [8, 84, 89, 107, 117, 119, 137]. However, there are limitations to potential model designs predominantly due to the issues of fabrication. These fabrication limitations are material driven and include the minimum width of channels, aspect ratio of etch depth to channel width, pressure rating and wettability of the models. Therefore, the range of materials used for the micro-models in this study

include silicon/glass, PMMA and glass. In addition, three types of micro-models have been designed: rough capillaries, single junctions and 'abstract' network models. Below are brief descriptions of these micro-model designs.

Rough Capillaries: the aim of these models is to investigate the role of roughness on the rate of spontaneous imbibition in relation to the Lucas-Washburn equation. To do this a range of models has been fabricated with varying degrees of roughness, see Figure 3.1.

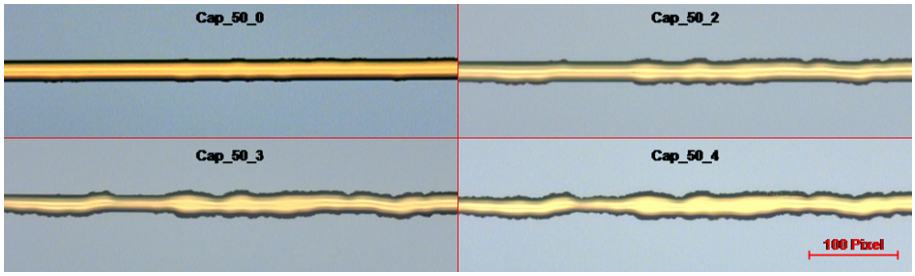


Figure 3.1.: Images of rough capillaries used within this study. The roughness increases from Cap_50_0 to Cap_50_4.

The designs were generated by starting with the roughest channel (e.g. Cap_50_4, Figure 3.1). In order to decrease the roughness in subsequent capillaries, additional pixels were removed systematically to 'plane' away the roughness. The initial .bmp designs are shown in Figure 3.2, with the mean width and the standard deviation of roughness presented in Table 3.1. All rough capillaries are silicon/glass micro-models with a nominal etch depth of 50 μm.

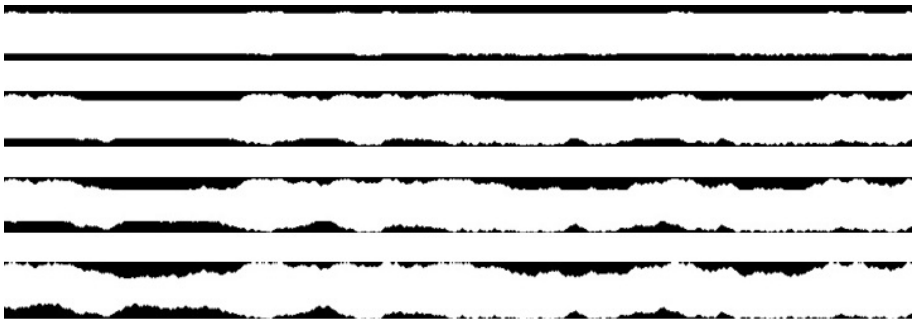


Figure 3.2.: The original .bmp files of the rough capillary designs investigated going from smoothest (Cap_50_0) to roughest (Cap_50_4): top to bottom.

Table 3.1.: Properties of rough capillaries investigated

Name	Mean Width (μm)	Roughness standard deviation (μm)
Cap_50_0	40.7	0.97
Cap_50_2	40.4	1.89
Cap_50_3	39.6	3.22
Cap_50_4	40.6	4.01

Mean width $\pm$ 1.54 μm - resolution of image

Single Junctions: the purpose of these designs is to investigate displacement pathways in single pore geometries during primary drainage and imbibition. All designs were created in AutoCAD. The pore geometries chosen are shown in Figure 3.3.

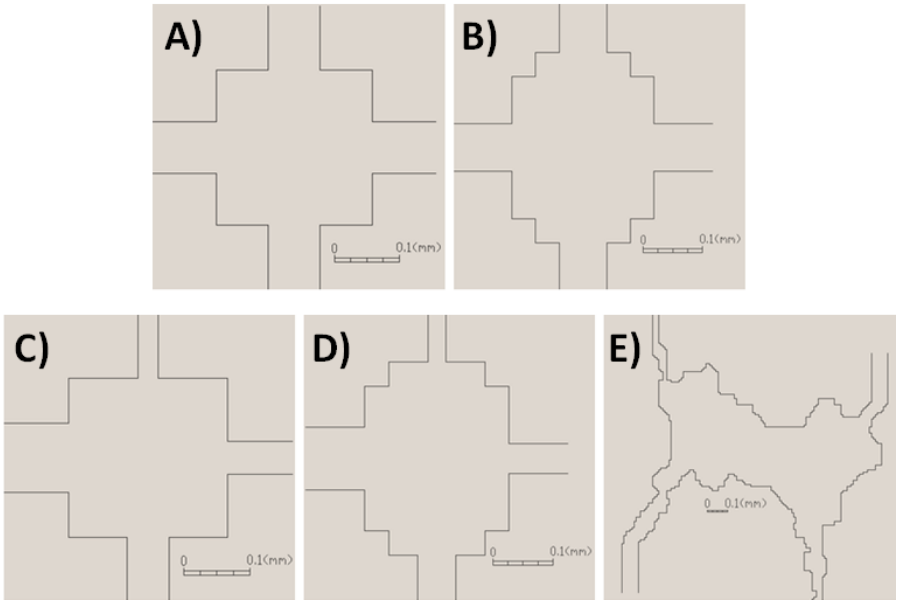


Figure 3.3.: Schematic micro-model designs, including channel configuration and connectors A) Square pore with equal throats, B) more complex pore body with equal throats, C) square pore with unequal channels, D) more complex pore body with unequal channels, E) single representative Berea pore.

The dimensions of the pore body and throats in the designs were chosen to give capillary entry pressures similar to those found in natural sandstones. The pore body width in Figure 3.3 A and C, is 240 μm in both directions. In the case of Figure 3.3 B and D, the pore body width in the x-direction

is 240 μm, and 320 μm in the y-direction. Figures 3.3 A and C display equal throat widths (80 μm), whilst in Figures 3.3 C and D, the throat widths vary, clockwise from top: 30, 50, 64 and 104 μm. These widths were chosen to give the range of capillary entry pressures shown in Table 3.2. The etch depth for all models was 50 μm. The capillary entry pressures were calculated using the Young-Laplace equation (Equation 5.1) discussed in Section 2.1.1. Finally, Figure 3.3 is a pore shape representative of a Berea sandstone. However, the dimensions are larger than in a real Berea sandstone due to fabrication limitations.

Table 3.2.: Capillary entry pressures for selected throat widths. Selected fluid n-decane, etch depth 50 μm, contact angle 30° and IFT 0.024 N/m

Throat Diameter (μm)	Capillary Entry Pressure (MPa)
30	2.22×10^{-3}
50	1.66×10^{-3}
64	1.48×10^{-3}
80	1.35×10^{-3}
104	1.23×10^{-3}

Due to the unique fabrication of each model, the throat widths will vary slightly from model to model. The precise dimensions corresponding to the models used in each experiment will be provided in the results section.

'Abstract' Network Models: these models are designed to build on the results of the single junction micro-models and provide a more representative model of actual porous media. The abstract network models are more complex constructions consisting of four distinct sections:

1. Inlet/outlet ports;
2. Fracture channels;
3. Porous plate;
4. Network matrix.

The main sections of the abstract network micro-models are illustrated in Figure 3.4.

The fracture channel is included to enable a flat drainage front to be

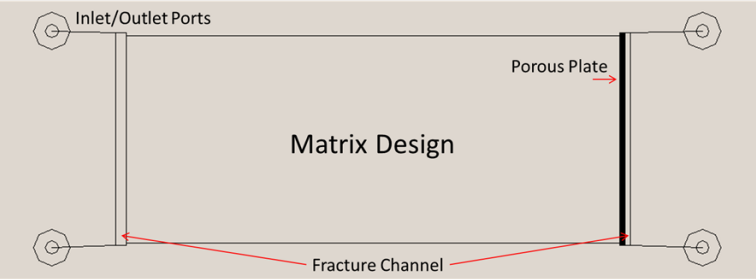


Figure 3.4.: Schematic of 'Abstract' network model. The main features are the inlet/outlet ports and fracture channels located at either end of the model. The 'porous plate' structure is situated at one end of the model with the matrix design in the centre.

injected into the matrix. This is possible as during drainage the widest throat will fill with the NWP first, so the fracture channel can be filled completely before the first matrix pore is invaded. This will ensure that all throats in contact with the fracture channel 'see' the NWP and can drain in order. The network matrix designs are based on physical properties of actual porous media, however, with idealised square/rectangular pores in plan view/cross-section, respectively. In the model design the pore/throat size distributions were maintained as best as possible to match real porous media. Figure 3.5 illustrates the pore throat size distributions of the micro-model (private correspondance) and Berea sandstone [9].

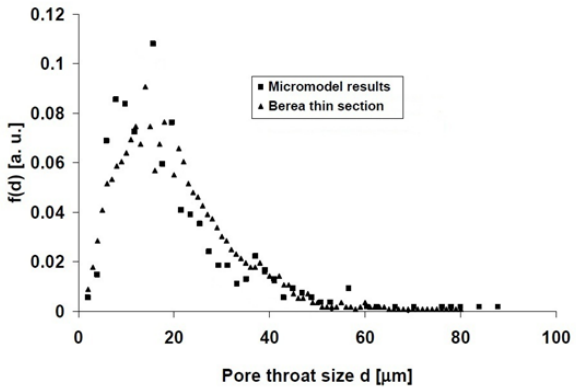


Figure 3.5.: Berea micro-model throat distribution in comparison to actual Berea thin section. Micro-model results from personal communication. Berea thin section results from [9].

The minimum throat width of the micro-model has been increased to

18 μm in comparison to the 2 μm of the Berea sandstone section. This is necessary for two key reasons. Firstly, the minimum throat width that can be achieved during fabrication is 7 μm. Secondly, the smallest size possible was reserved for fabrication of a 'porous plate' structure at one end of the model. The porous plate consists of a row of closely spaced narrow channels (8 μm), illustrated in Figure 3.6. This has been included to allow greater saturation of the NWP without breakthrough into the outlet fracture channel. This is required to achieve a flat front during the imbibition stage following drainage. Therefore, to guarantee no NWP will go through, there had to be a reasonable size difference (10 μm) between the porous plate and the narrowest throat in the matrix, see Table 3.3. The etch depth was selected to be 25μm.

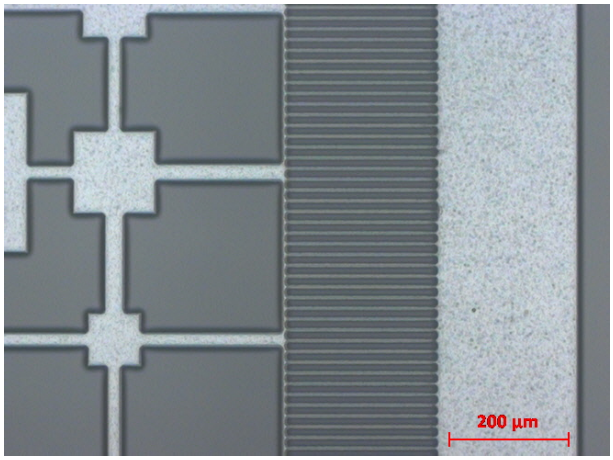


Figure 3.6.: Image of a section of the 'porous plate' within the micro-model. The narrow throats of the 'porous plate' are 8 μm in width.

Table 3.3.: Capillary entry pressures for narrowest throat in matrix design and throats of porous plate. Selected fluid DI water, etch depth 25 μm, contact angle 30° and IFT 0.072 N/m

Throat Diameter (μm)	Capillary Entry Pressure (MPa)
8	2.06×10^{-2}
18	1.19×10^{-2}

The process of creating the design begins with running a Matlab code which generates matrices based on the statistical properties of Berea sandstone. The Matlab code was created by Jianhui Yang (see Appendix A). The

code includes the throat radius dimensions (9 - 95 μm) and pore dimensions (12 –157 μm). The code then outputs a subsection of the design illustrated in Figure 3.7 A, which is 10 $\times$ 20 pore bodies, and the corresponding throat distribution, Figure 3.7 B.

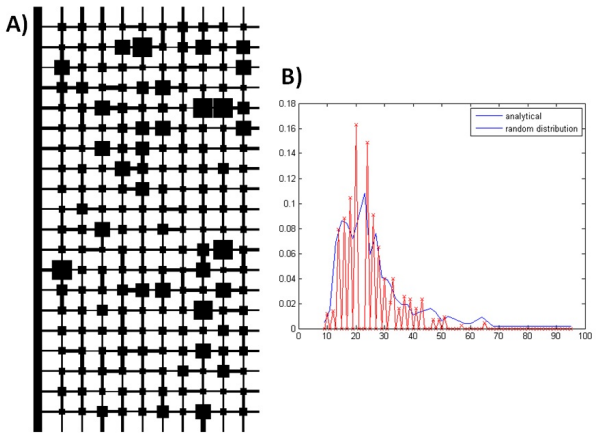


Figure 3.7.: A) subsection of the 'abstract' network design B) the corresponding throat distribution created by the MatLab code

The code makes sure that a throat width cannot be larger than a connecting pore body. Multiple 10 $\times$ 20 pore body sections were created to form the entire design. These sections were then stitched together to create a suitably sized model: 35 $\times$ 80 pore bodies. All sections are originally created as .bmp files by MatLab; these are then converted to .dwg using open source software img2cad. Once in AutoCAD the sections are stitched together. In order to achieve this all throats on the right hand side of the design were removed. Two sections were positioned at the same level; the throats on the left hand section were then moved manually to ensure they were in the centre of each pore body. Finally, the 'porous plate' was added manually using AutoCAD. Figure 3.8 is the final design.

3.2. Micro-model Fabrication

Having designed the micro-models, it is necessary to fabricate them. The key requirements for micro-models are that they are fabricated from transparent and hardy materials which allow reproducible real time visualisation of the fluids. Various materials are available: Polydimethylsiloxane

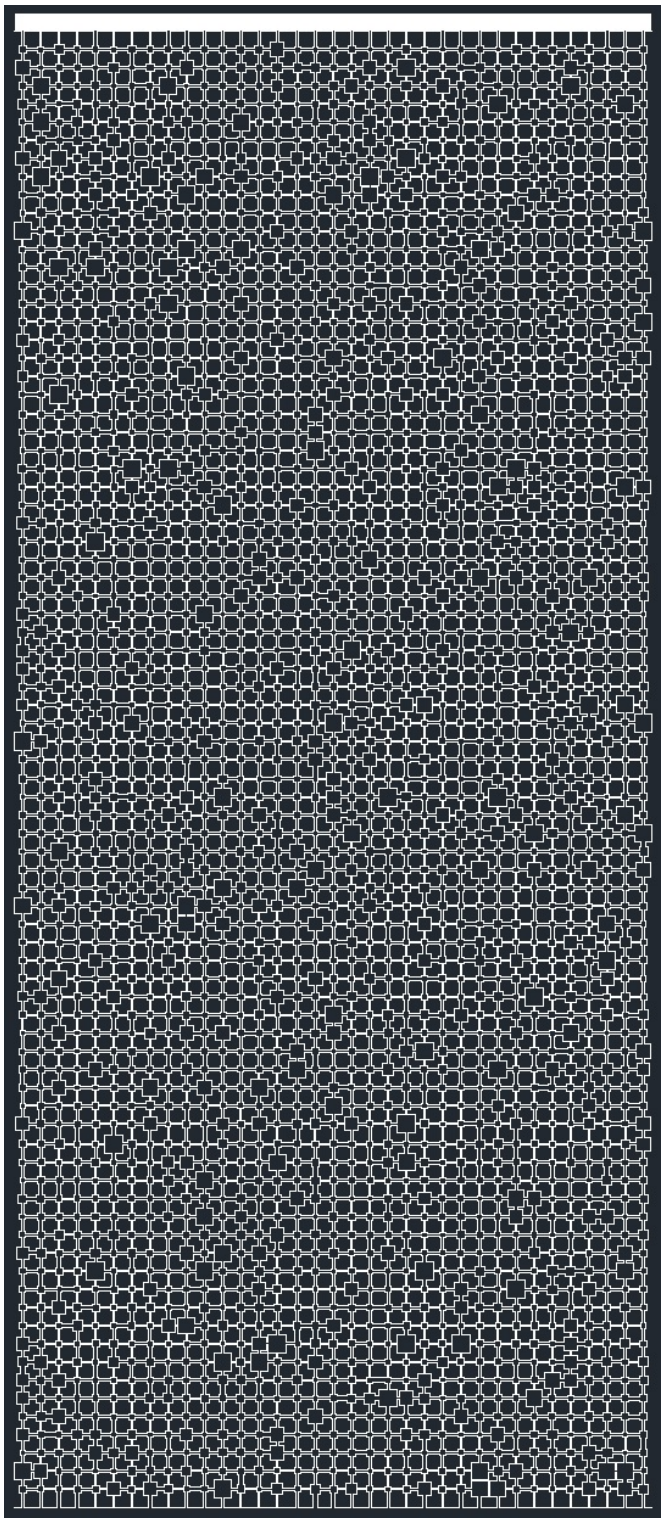


Figure 3.8.: The final 'abstract' micro-model design, including the 'porous plate' on the right-hand-side of the design.

(PDMS), PMMA, silicon and glass. There are advantages and disadvantages to each material, including etching limitations, pressure restrictions, fabrication time and cost. Therefore, the micro-models used in this study have been fabricated from different materials based on the purpose of each experiment. The fabrication processes for the models utilised in this work are detailed below.

PMMA Micro-models are fabricated of Poly(methyl methacrylate) (PMMA), an acrylic thermoplastic material which is a good substitute for glass. PMMA models are relatively inexpensive and fast to fabricate. However, there are limitations, including possible swelling of the models related to reaction and absorption of injected chemicals. Also, only moderate temperature and pressures can be used with these models.

A PMMA model consists of two wafers which are bonded together to form an enclosed micro-fluidic pattern. All of the PMMA models in this study have been fabricated by Epigem (Redcar). The general fabrication process is:

1. Spin coat a uniform layer of SU-8 (an epoxy based photoresist) onto the base wafer;
2. Allow SU-8 layer to dry and fully cure before depositing a secondary layer in the same way;
3. Expose the design through a photo-mask to develop the design;
4. Deposit a partially cured SU-8 layer onto the underside of the top wafer, which will form the top of the design
5. Drill the inlet/outlet holes into the top wafer;
6. Assemble the base and top wafers in a registration bonding jig and heat under load in a laminating press. This is held for a period of time to form the bond;
7. Finally, dice up the wafers into individual models.

Figure 3.9 A is the wafer layout for the single junction micro-models. Schematic images of the top down view and cross-section of the PMMA micro-models are given in Figure 3.9 B and C.

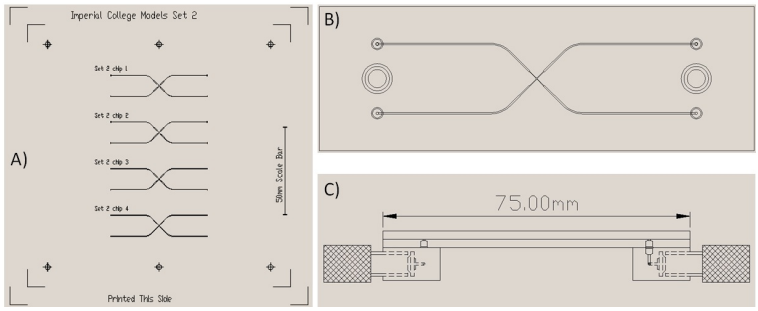


Figure 3.9.: A) General wafer layout for PMMA micro-models B) Top down view of model C) cross-section of model including connections.

All of the PMMA models in this study have been chemically treated by Epigem, increasing the hydrophobicity of the surface. The etch depth of the models is approximately 50 μm. However, due to fabrication process each chip is unique and therefore the etch depth can vary between chips.

Glass Micro-models. Figure 3.10 outlines the general procedure for fabrication of the Glass micro-models via wet-etching. In our case the etching was achieved by Deep Reactive Ion Etching (DRIE), though Steps 1-4 are still the same. Unlike wet-etching, DRIE is an anisotropic etching technique which allows steep-sided channels that have high aspect ratios and a rectangular cross-section, unlike the rounded cross-sections illustrated in Figure 3.10 5. The mask through which the glass wafer is exposed, Figure 3.10 Step 2, is an 'abstract' network design we provided to The Dolomite Centre Ltd. Furthermore, the top wafer of the models has been highly polished via a process called Chemical Mechanical Polishing (CMP). This is done to allow precise positioning of the access holes for drilling. The two glass wafers are then bonded by van der Waals forces followed by thermal bonding at 1000°C.

The models are able to withstand pressures up to 100 bar. To achieve repeatable experiments at 100 bar pressure, modifications were required to the Polyether ether ketone (PEEK) holder provided by The Dolomite Centre Ltd. The original inlet/outlet connections were sealed by pressing a plastic ferrule directly on the glass. The micro-models were easily broken when pressure was applied whilst trying to make the connection leak-tight. Therefore the PEEK holder was redesigned to mitigate this problem. Figure

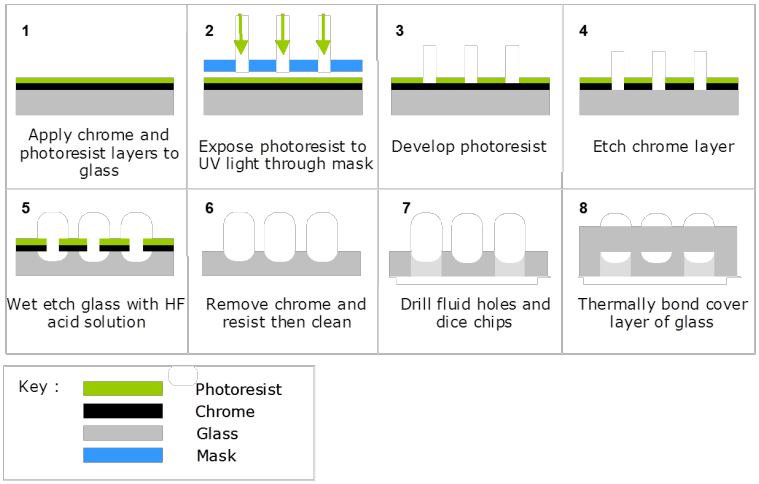


Figure 3.10.: General etching procedure for glass micro-models. Provided by The Dolomite Centre Ltd.

3.11 A, is the holder provided by the manufacturer and B, is the modified version of the PEEK holder. The modified version contains a ledge onto which the fittings are tightened and small o-rings which seal to the model, illustrated in the close-up of Figure 3.11 B. These modifications allow the fittings to be fully tightened without the glass model breaking due to excess pressure.

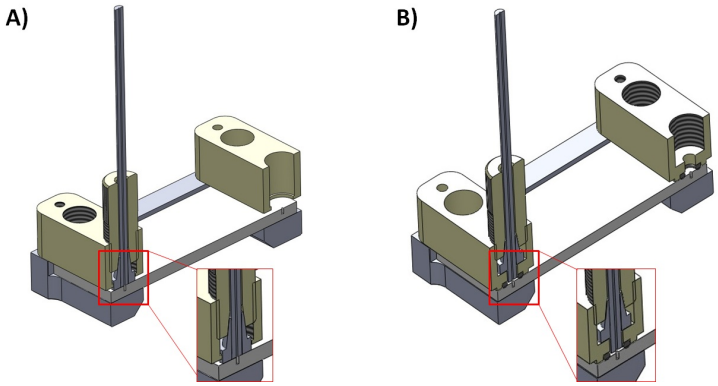


Figure 3.11.: A) Original PEEK glass micro-model holder, close-up illustrates the fitting directly touching the micro-model B) modified PEEK glass micro-model holder with the addition of an o-ring contacting the micro-model.

Silicon micro-models. The fabrication procedure of silicon/glass

micro-models still follows the procedure pioneered by Hornbrook *et al.* in 1991 [89]. The fabrication procedure can be simplified into four key stages:

1. **Digital manipulation** – once a satisfactory black and white image of the design is obtained the image was altered manually to systematically increase the roughness of the capillary;
2. **Image mask construction** – this is then used to transfer the flow pathway image onto the silicon wafer;
3. **Image transfer and etching** – the silicon wafer is coated with a photoresist onto which the image mask is placed. UV light is shone through the mask with the photoresist destroyed by the UV light. The exposed pore bodies are then etched to the desired depth;
4. **Model construction** – the models are then treated to achieve the desired wettability, for water-wet models the silicon must be oxidised. Lastly, a flat glass plate is anodically bonded to the base to create an isolated flow path to study pore level events.

However, unlike the 100 % glass micro-models, silicon/glass models are unable to withstand high pressures.

3.3. Imaging Techniques

The bulk of the experimental results presented in this thesis was acquired via optical imaging techniques. The main experimental apparatus used in capturing the images and/or videos in this study will be described in detail below, including an inverted light microscope, a high speed video microscope and a digital single-lens reflex (DSLR) camera. The exact experimental procedure for each set of experiments will be described separately.

3.3.1. Inverted Light Microscope (ILM)

To capture precise images of the micro-models used in the experiments, a calibrated inverted light microscope (ILM) was used (AxioObserver A1.m, Zeiss) coupled with a motorised stage (Mac 6000 system, Ludl Electronic

Products Ltd) which allowed accurate positioning of the micro-models. The ILM used was equipped with six objectives ranging from 2.5× – 50× magnification. Details of the objectives can be found in Table 3.4, providing high quality images from which accurate measurements of the micro-model channel widths could be taken. The configuration of the ILM also allowed the micro-models to be imaged in either transmitted or reflected light depending on the nature of the models.

Table 3.4.: Details of Objectives found on the ILM

Magnification	Objective Type	Aperture	Free Working Distance (mm)	Resolution (μm/pixel)
2.5x	EC Epiplan-Neofluar	0.06 HD* M27	15.1	6.29
5x	EC Plan-Neofluar	0.16 Ph**2	18.5	3.09
10x	EC Epiplan-Neofluar	0.25 HD	9.0	1.54
20x	EC Plan-Neofluar	0.5 Ph2	2.0	0.77
40x	EC Plan-Neofluar	0.75 Ph2	0.71	0.38
50x	EC Epiplan-Neofluar	0.55 HD DIC***	9.0	0.31

HD - brightfield/darkfield, Ph - phase contrast, DIC - differential interference contrast

All the images were captured via the digital camera (AxioCam HSc) attached to the left sideport of the microscope; see Figure 3.12, component 2. Live images of the model positioned on the stage can be viewed through either the Eyepiece (3.12, component 21) or directly on the PC by running specialist software AxioVision (Version 4.8.1, Zeiss) attached to the microscope via a FireWire cable. Furthermore, another advantage of the ILM is the motorised stage – in X and Y directions – with an absolute accuracy ± 5 μm, which allows large Mosaic images to be acquired. This enables the whole model to be imaged if required rather than just the limited field of view, at the expense of long acquisition time.

In order to protect the objectives, an Aqua-stop II (Zeiss) was installed over the nosepiece to ensure that no fluid came into contact with the objec-

tives. The Aqua-stop II diverts any spillages into a small beaker located off to the side of the microscope.

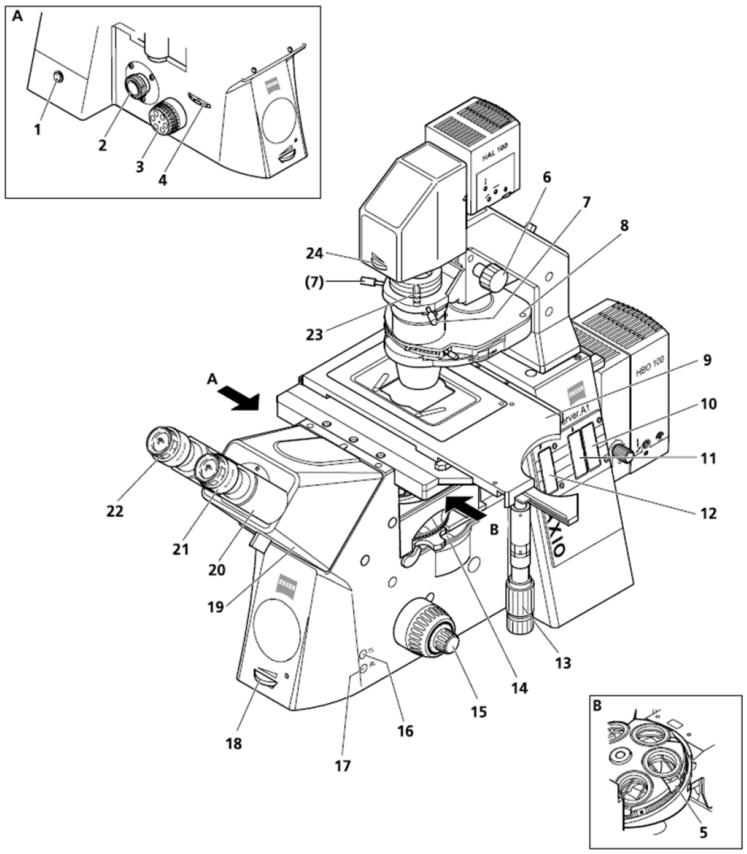


Figure 3.12.: Schematic of a Zeiss AxioObserver A1.m inverted light microscope. A list of components is given below.

Components and Controls:

1	On/Off switch	13	Drive knobs for controlling XY positioning of the mechanical stage
2	Left sideport	14	Reflector turret
3	Coarse/fine focus drive (left side) with fine drive, flat[1]	15	Focus drive coarse/fine (right side)[1]
4	Light path switching control (left side port/vis)	16	TL button for switching the transmitted light halogen illuminator on and off

5	Objective nosepiece	17	RL button for switching the reflected light shutter (fluorescence) on and off[3]
6	Vertical adjustment knob for condenser	18	Halogen illumination intensity control
7	Condenser centring screw	19	Binocular tube
8	Condenser	20	Binocular section of the binocular tube
9	Microscope stage	21	Eyepiece
10	3-position filter slider slot (diameter 25 mm)	22	Eyepiece adjustment ring
11	Slot for iris stop slider as reflected light aperture stop of FL attenuator[2]	23	Polarizer with 2-position filter changer or 3-position filter changer
12	Slot for iris stop slider as reflected light luminous-field stop[2]	24	Luminous-field stop control

[1] The positions are reversed on the microscope, [2] Not in use, [3] Not in use - reflected light controlled by external control box

3.3.2. High Speed Video Microscope (HSVM)

For the experiments in which the displacement processes occur very rapidly, an optical system with fast acquisition was necessary. This was achieved by combining the Navitar 12X Zoom system with the FastCam recording system, described below.

The main component is a 12X Zoom system in the body tube (12 mm Fine Focus, 1-50486, Navitar), which contains the core zoom mechanisms. Both the zoom and focus can be altered manually allowing great flexibility in the field of view which may be increased or decreased depending on the region of interest. Both zoom and focus adjustments can be performed independently to achieve the optimal image. In order to complete the 12X Zoom system an 0.67X adapter tube (0.67X Standard Adapter, 1-6020, Nav-

itar) is required, in combination with a C-mount coupler (1-6010, Navitar). This allows accurate positioning of the camera sensor in the optical imaging plane of the 12X zoom system. To view and capture images and/or videos, a single head camera (MC2, Photron) is attached to the top of the body tube. Furthermore, a range of lens attachments is available – 0.25×, 0.5×, 0.75×, 1.5×, 2× – (1-50011, 1-50012, 1-50013, 1-50014, 1-51473, Navitar) which attach to the base of the body tube allowing a greater range of field of views possible.

Either single 'snap shot' images or videos can be recorded with the HSVM; 512 × 512 pixel resolution is obtainable up to 2,000 frames per second (fps) with a maximum achievable frame rate of 10,000 fps possible at reduced image resolution. The live feed from the camera is transferred to the PC via a Gigabit Ethernet connection and is viewed via specialist software: Photron Fastcam Viewer (PFV). The micro-models can be easily positioned for imaging using a graduated manual stage over a dimmable LED microscope base (Meiji Techno), with the stage moving independently in both x- and y-directions. The dimmable microscope base allows imaging in transmitted light. However, for reflected light additional lighting is required – this is produced by a LED ring light positioned above the sample (LED ring light 66/40, Photonic) controlled by a separate controller (LED standard control unit, Photonic). The entire set-up is located within a laminar flow cabinet (PurAir-48, Air Science) to prevent sample contamination from dust settling on and near the micro-models and reducing the possibility of blockages.

3.3.3. DSLR Camera

For situations that require rapid acquisition of a larger field of view than either the ILM or HSVM can provide, a DSLR camera (D800E, Nikon) combined with a Micro lens (AF-S Micro Nikkor 105 mm, Nikon) and filter (Pro1 Digital Close-Up No.3, Hoya) have been used.

To allow continuous operation, an AC adapter (EH-5b, Nikon) is connected to the camera via a power connector (EP-5B, Nikon) instead of a conventional battery. The camera is linked to the PC via a USB cable (UC-E14 USB, Nikon) which allows the camera to be controlled remotely via dedicated software: Camera Control Pro 2 (Ver 2.13.0, Nikon). The camera

is always operated in Manual setting mode and is controlled via Camera Control Pro 2. Here features including aperture, shutter speed, storage location, and image type can be chosen. Possible image formats include: RAW, JPEG and TIFF.

The camera is positioned on an adjustable stand (fabricated in-house) which can be adjusted manually to attain the best image possible. The camera points vertically down onto the models.

Either still images or videos can be captured with the DSLR. The DSLR can be set to capture still images at set time intervals. The models can be viewed in either transmitted or reflected light. To image the models in transmitted light, a dimmable halogen backlight is used (Fiber-Lite, DC-950, Dolan-Jenner). The intensity of the light is controlled by a separate box which is attached by a fibre-optic cable.

4. Exploring the Lucas-Washburn Equation: Rough Capillaries

Abstract

The effect of surface roughness on capillary displacement dynamics is investigated. First, displacement dynamics in smooth capillaries is investigated for validation purposes. Although the viscosity ratio between the two phases is sufficiently high, the Lucas-Washburn square-root of time behaviour is not observed due to the time scale of the experimental displacement process. Instead, displacement in the visco-enertial regime was observed associated with mensicus position increasing linearly with time. Second, a set of square capillaries, etched in silicon, is used, with systematically increasing surface roughness. It was observed that, in the roughest capillary, the advancing meniscus became pinned. Second, a systematic decrease in the rate of imbibition with increasing roughness was observed. Recent simulation studies in nano-pores have shown a linear decrease of the rate of imbibition with roughness increasing. In contrast, in this experimental study, the rate of imbibition was observed to decrease with the fourth power of time. A separate independent measure of the dynamic contact angle is required to confirm our observations.

4.1. Introduction

Understanding dynamic processes within porous media is very important for a number of applications [138], including CO_2 storage and enhanced oil recovery processes. In this chapter, single capillaries of varying roughness, are used to investigate the effect of surface roughness on the displacement

dynamics. For smooth capillaries, the Lucas-Washburn equation (2.7) states that the distance travelled by the fluid interface within a capillary is proportional to the square root of time for a sufficiently high viscosity ratio between displacing and displaced phase. Assuming that the capillary and friction forces are balanced [41–46], the well-known Lucas-Washburn equation can be derived:

$$l^2 = \frac{\gamma w cos\theta^a}{3\eta_w}(t + t_0), \tag{4.1}$$

where l is the distance the meniscus has travelled into the capillary, w is the width of the capillary, θ^a is the advancing dynamic contact angle, η is the viscosity of the fluid and t is the time. The dynamics of capillary filling depend on two characteristic time-scales discussed in Chapter 2.1.4.

This chapter will focus on the displacement dynamics within single capillaries and the observations of different time scales and the transition between them. Spontaneous imbibition experiments have been conducted in various single capillaries with the results linked back to the Lucas-Washburn equation. Recent computational work [103] has indicated that the surface roughness of nano-capillaries can alter the l vs. t relationship. To explore this, a series of single capillaries, including both smooth glass capillaries and those in which the 'roughness' has been systematically altered, with the aim of understanding the influence of roughness on the rate of imbibition.

4.2. Experimental Set-up

The experiments presented in this chapter have been conducted in two types of capillaries: smooth borosilicate glass and rough silicon/glass capillaries. The smooth borosilicate glass capillaries have a simple rectangular cross-section. The design and fabrication of the rough capillaries are discussed in Chapters 3.1 and 3.2, respectively. The dimensions of each of the models used will be given in the results section below. During these experiments different microscopy techniques were used to accurately determine and capture the geometry of the capillary and fluid displacement events. The two primary imaging tools used were the high speed video microscope (HSVM)

and the Nikon DSLR camera to capture dynamic processes. The inverted light microscope (ILM) and micro-CT scanner were used to verify capillary dimensions. All the micro-CT scans were conducted by Nathan Welch. A more detailed description of the imaging techniques (excluding micro-CT) is given in Chapter 3.3.

The methodology has been subdivided into two sections: verification of capillary geometry and spontaneous imbibition methodology. All experiments have been conducted at ambient temperature and pressure conditions.

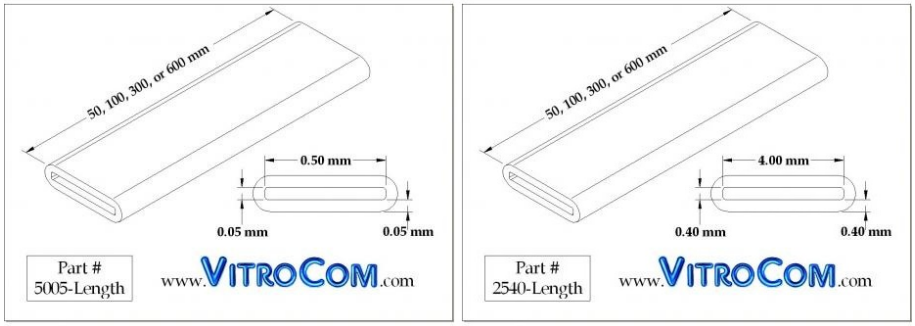


Figure 4.1.: Schematic of the cross-section of borosilicate caillaries A) 500 x 50 μm B) 4000 x 400 μm [10].

Verification of capillary geometry. For the smooth capillary experiments, the dimensions of the two borosilicate glass capillaries used were – 500 $\times$ 50 μm (5005/100, VitroCom) and 4000 $\times$ 400 μm (2540/100, VitroCom) – respectively. A cross-section schematic of the capillaries is given in Figure 4.1. It was assumed that the dimensions provided by the manufacturer were correct.

Next, capillaries in which the roughness has been systematically altered were investigated; Figure 4.2 shows the change in roughness for the capillaries. These capillaries have been fabricated in silicon/glass. A description of the fabrication methodology is given in Chapter 3.2.

However, due to the fabrication process of the silicon/glass micro-models the exact dimensions needed to be attained for each model used. The ILM allows high resolution still images of the capillaries to be taken from which the width can be accurately measured, see Figure 4.3 A. Images of the inlet

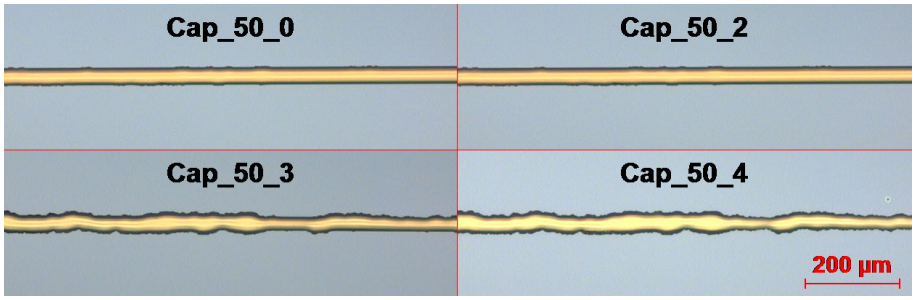


Figure 4.2.: Image illustrating the increase in roughness for the silicon/glass etched capillaries investigated

were taken using the ILM to ascertain the etch depth of the capillaries. In Figure 4.3 B and C, the etched capillary can be seen in the silicon wafer which has been covered by a glass plate. However, the cross-section of the capillary is not rectangular, (see Figures 4.3 B and C), as would be expected from the DRIE etching technique, discussed in Chapter 3.2. This artefact is most likely due to the dicing process during fabrication. Therefore, to establish an accurate etch depth needed for analysis the capillaries were scanned via micro-CT microscopy.

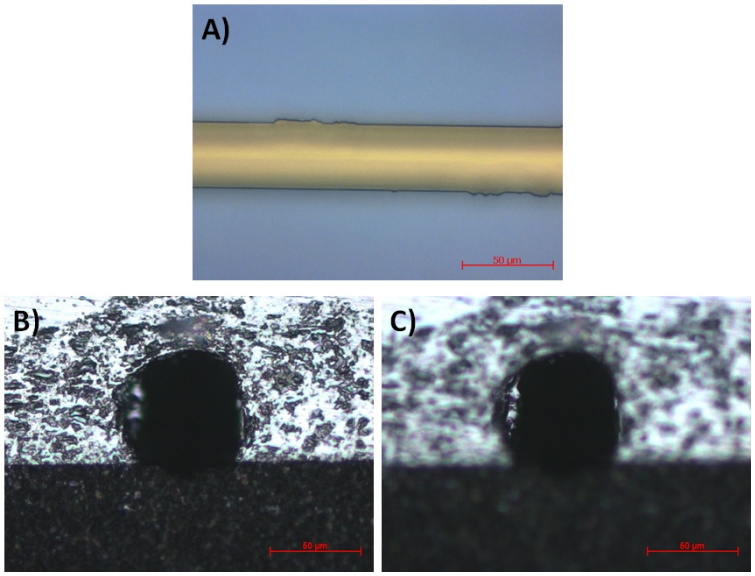


Figure 4.3.: A) Width of the capillary B) Entrance of the capillary C) Entrance of the capillary

Spontaneous Imbibition methodology. All of the experiments were

conducted with the capillary positioned horizontally at ambient temperature and pressure conditions. The fluids investigated were DI water ($\eta_{DI} = 0.89$ mPa s, $\gamma_{DI} = 0.072$ N/m, $\rho_{DI} = 1000$ kg/m^3) and hexadecane (η_H= 3 mPa s, $\gamma_H = 0.027$ N/m, $\rho_H = 770$ kg/m^3).

To visualise capillary filling the smooth borosilicate glass capillaries were placed on the base illuminated stage with no additional lighting necessary. In contrast, the rough capillaries required additional lighting to illuminate the capillary, see Figure 4.4. The capillary filling process was captured via either the HSVM or the DSLR camera.

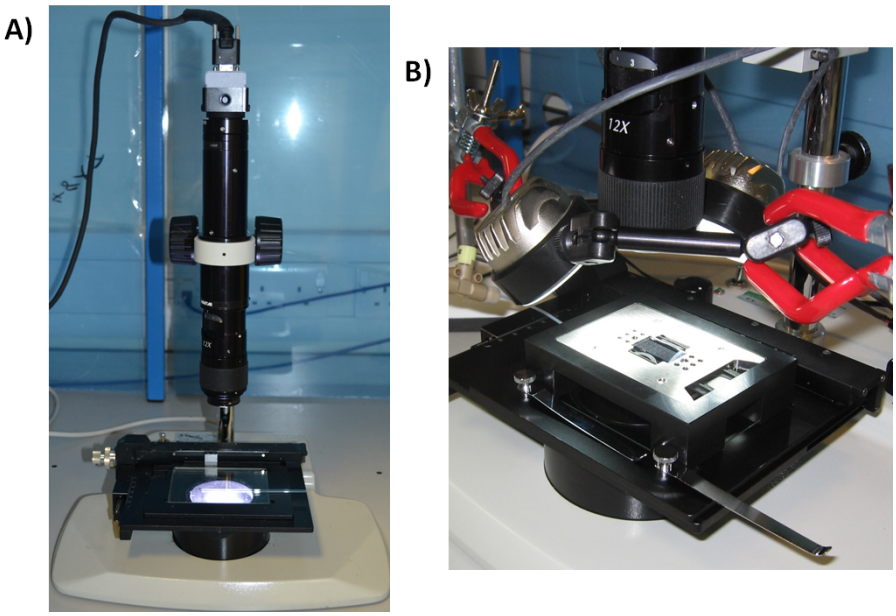


Figure 4.4.: A) HSVM set-up in transmitted light mode using the illuminated stage base B) HSVM set-up in reflected light mode using additional lighting from above

The selected imaging technique is then set to record before a droplet of the fluid was placed by the inlet of the capillary which would then spontaneously imbibe into the capillary. A 1 ml syringe (BD Plasipak, BD300013) was used with the fluids passed through a Millipore filter (Millex-MP 0.22 μm, Millipore) to limit foreign particles entering the capillary.

Image analysis. The videos were analysed in ImageJ (open source software). To begin with, the correct time is determined by dividing the frame by the experimental frame rate. Next the resolution of the image is calcu-

lated in terms of microns/pixel. To determine the distance the meniscus has travelled into the capillary, the line and measure capabilities of ImageJ are used, with the length of the line multiplied by the resolution to get the distance in microns.

4.3. Results and Discussion

The results for both smooth and rough capillaries are presented in Section 4.3.1 and Section 4.3.2, respectively. Finally, the conclusions are discussed in Section 4.4.

4.3.1. Smooth Capillaries

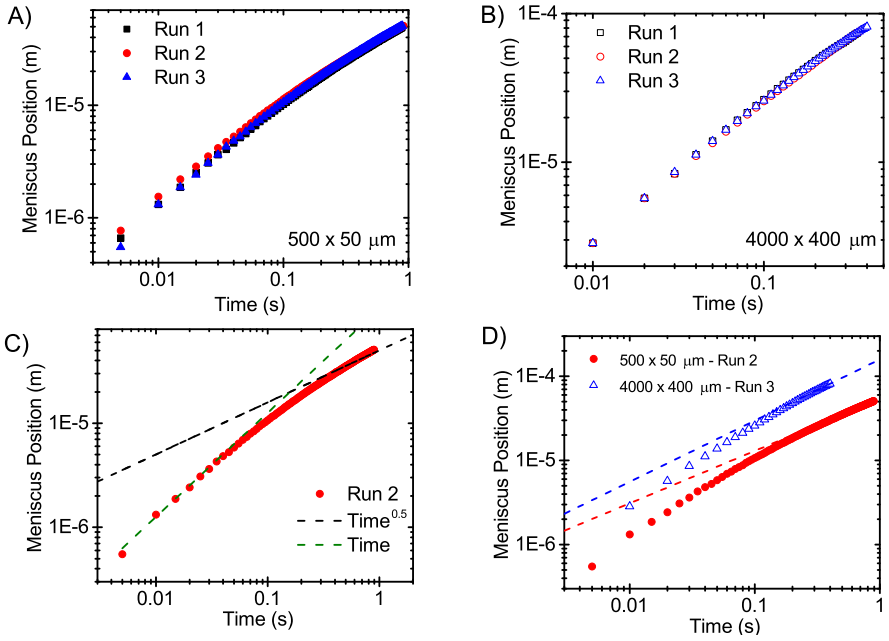


Figure 4.5.: Smooth capillary results A) 500 × 50 μm Runs 1-3 B) 4000 × 400 μm Runs 1-3 C) 500 × 50 μm Run 2 including trend lines for Time and Time$^{0.5}$ to illustrate the different time regimes D) 500 × 50 μm Run 2 and 4000 × 400 μm Run 3 including $t^{0.5}$ trend line with neither reaching the Lucas-Washburn regime.

Initial spontaneous imbibition experiments were conducted in smooth glass capillaries with DI water as the wetting phase. Two different size

capillaries were investigated – 500 × 50 μm and 4000 × 400 μm – the results are presented in Figures 4.5 A and B. Multiple runs were conducted for each size of capillary with a new clean capillary used each time. Figures 4.5 A and B, show the three runs for the 500 × 50 μm and 4000 × 400 μm capillaries. The reproducibility of these experiments is very good.

As discussed in Chapter 2.1.4, three distinct length vs. time regimes exist: inertial, visco-inertial and Lucas-Washburn. In this work only the visco-inertial and Lucas-Washburn regimes are expected to be observed. This is because the inertial regime is almost immediately overcome for the Ohnesorge numbers considered in this work, see section 2.1.4 for further detail. These regimes can be best observed by applying trend lines scaled to the data. As illustrated in Figure 4.5 C, in the 500 × 50 μm capillary data, at early time scales a $l \sim t$ relationship is observed, as displayed by the green dashed line. This behaviour correlates to the visco-inertial regime. However, with increasing time this linear regime is gradually lost. For times greater than 0.04 s, the exponent of $l \sim t$ relationship lies between 0.5 - 1. This illustrates that a transition phase between the visco-inertial regime and the Lucas-Washburn regime is observed. The $l \sim t^{0.5}$ trend of the Lucas-Washburn regime is displayed by the black dashed line in Figure 4.5 C. However, within these experiments the Lucas-Washburn regime is not reached. To definitively be in the Lucas-Washburn regime the slope should be 0.5 when plotted on a log-log scale. This observation can be quantified by calculating the linear slope in the later stages of the experiments. For the small capillaries the slope is 0.6, whilst the large capillary slope was found to be 0.7. Therefore, the small capillaries are closer to achieving the Lucas-Washburn regime as implied by the viscous time scale outlined in Section 2.1.4.

4.3.2. Rough Capillaries

Having established that the experimental methodology produces reproducible results, the effects of roughness on meniscus position within the capillary were investigated. It is not obvious from the standard form and formulation of the Lucas-Washburn equation that the capillary roughness should alter the meniscus behaviour. However, recent Molecuar Dynamics

(MD) computer simulation studies have indicated that the roughness can slow down the meniscus penetration by altering the dynamic contact angle and decreasing the hydrodynamic radius [103].



Figure 4.6.: Pinned meniscus taken with 50× objective, the imbibing DI water is blue whilst the empty capillary is orange

Initial rough capillary experiments were conducted with DI water as the wetting phase. During these experiments it was observed that in the roughest capillary the meniscus became pinned. Once the meniscus became pinned the micro-model was transferred onto the ILM for imaging. Figure 4.6 is an image of the pinned meniscus, with both DI water (blue/grey) and air (orange) present.

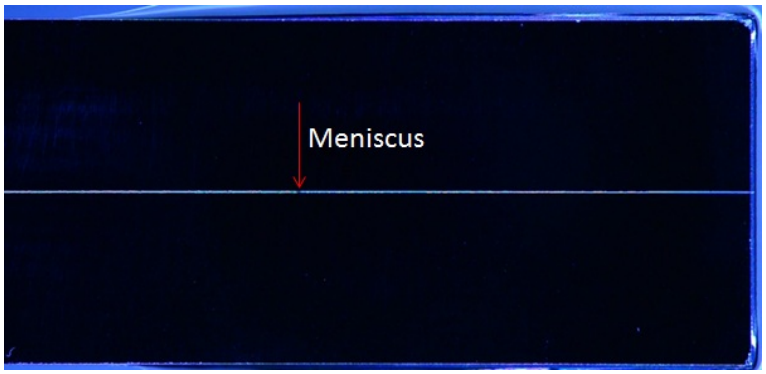


Figure 4.7.: Snap-shot of the meniscus within a rough capillary taken with the DSLR camera.

Unfortunately, these experiments were not reproducible. This is believed to be due to degradation of the oxidation layer within the models over time. This layer was responsible for making the micro-models water-wet. We

suggest that, over time, the models converted from water-wet to oil-wet. Due to this change in wettability, hexadecane was chosen as the WP. All of the experiments conducted with hexadecane were recorded via the DSLR at 60 fps. Figure 4.2 shows the increasing roughness of the capillaries from Cap_50_0, the smoothest, to Cap_50_4 the roughest. Figure 4.7 shows a snap-shot of hexadecane imbibing into the rough capillary.

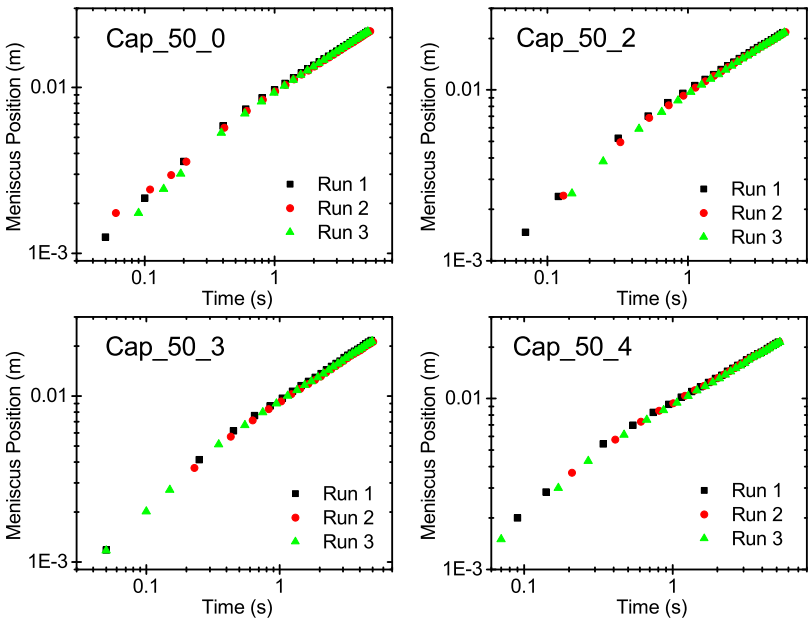


Figure 4.8.: Meniscus position vs time for capillaries of different roughness (Cap_50_0 – smoothest to Cap_50_4 – roughest)

Figure 4.8 plots the position of the meniscus within the capillary as a function of time for the capillaries shown in Figure 4.2. Multiple reproducible runs were conducted for each capillary, with the capillary cleaned with propanol and DI water between each experiment.

As shown by equation 2.7, the prefactor is dependent on the contact angle, capillary radius and viscosity. The increasing roughness is expected to decrease the meniscus velocity by altering both the dynamic contact angle and the radius. Martic *et al.* [138] have illustrated that the Lucas-Washburn equation can be rewritten as:

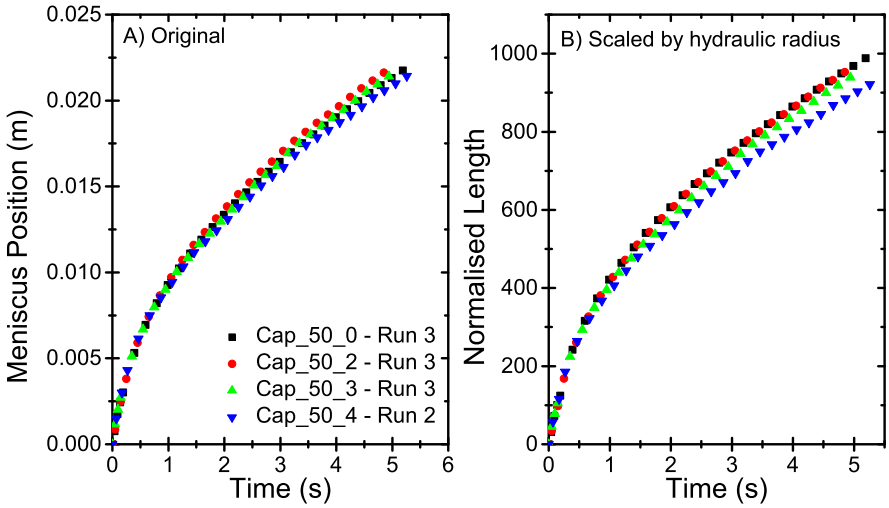


Figure 4.9.: A) Original data of selected runs of all the capillaries B) Normalised data for all the capillaries, in which the roughest capillary is also the slowest.

$$l(t) = -\frac{P_1}{P_2} + \sqrt{\frac{2t}{P_3} + \left(P_1 + \frac{P_2}{P_3}\right)^2} \tag{4.2}$$

where P_1 is $l(0)$, $P_2 = \frac{\xi}{\gamma_{LV} cos\theta^0}$ and $P_3 = \frac{4\eta}{R_H \gamma_{LV} cos\theta^0}$, where ξ is the coefficient of friction. Furthermore, the hydraulic radius (R_H) can be calculated from $R = \frac{R_D^2}{R_V}$, where R_D and R_V are the hydrodynamic and volumetric radius respectively. For long time scales equation 4.2 is dominated by P_3 and reverts to the standard Lucas –Washburn equation. However, Stukan *et al.* [103] illustrated that these variations lead to a linear relationship between increasing roughness and decreasing meniscus velocity.

The rough capillaries considered in this work display an array of capillary widths and etch depths which will mask the effect of the roughness. To remove this contribution, the results were normalised by the hydraulic radius. Furthermore, as hexadecane was used throughout, the viscosity remains constant. Therefore, the intercept of the log-log plot should only be dependent on the intrinsic contact angle and capillary roughness. In Figure 4.9 the original (A) and normalised (B) data for selected runs from each capillary roughness are shown. The normalised data now shows a trend in which the roughest capillary is also the slowest.

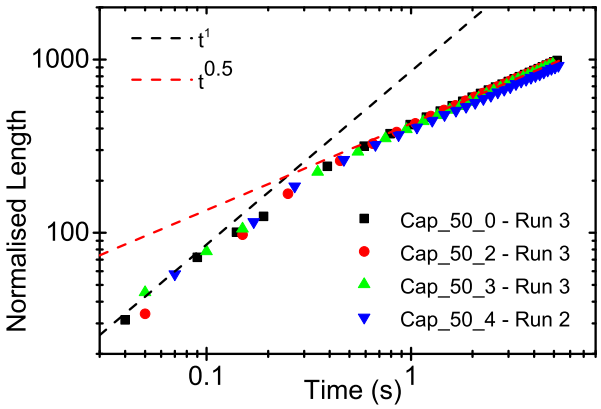


Figure 4.10.: Selected single runs from each capillary of difference roughness illustrating the transition from the visco-inertial regime (black dashed line) to the Lucas-Washburn regime (red dashed line).

As in the smooth capillaries, initially, the results are linear with time, indicating displacement in the visco-inertial regime. However, as the meniscus travels further into the capillary, the transition to the Lucas-Washburn regime is observed, as indicated by the 0.5 gradient in the high t region.

Table 4.1.: Properties of the rough capillaries investigated

Name	Mean Width (μm)	Roughness (μm)	Gradient	Intercept
Cap_50_0	40.7	0.97	0.508	2.631
Cap_50_2	40.4	1.89	0.509	2.629
Cap_50_3	39.6	3.22	0.514	2.616
Cap_50_4	40.6	4.01	0.515	2.593

To systematically investigate the effects of the capillary roughness, the intercept of the high t linear fit has been calculated for each capillary. In Figure 4.10 A-D, a single run for each capillary is displayed and the gradient and intercept from the log-log plots outlined in Table 4.1. As expected from Stukan *et al.* [103], the intercept gradually decreases with increasing roughness. Furthermore, Stukan *et al.* [103] suggested a direct correspondence between changes in the roughness and the intercept and, therefore P_3. However, a linear relationship between these parameters, as found by Stukan *et al.* [103], is not observed, as shown in Figure 4.11. Instead, we observe a quartic decrease of the intercept with increasing roughness ($\frac{Standard Deviation}{Mean}$), as shown in Figures 4.12 A and B.

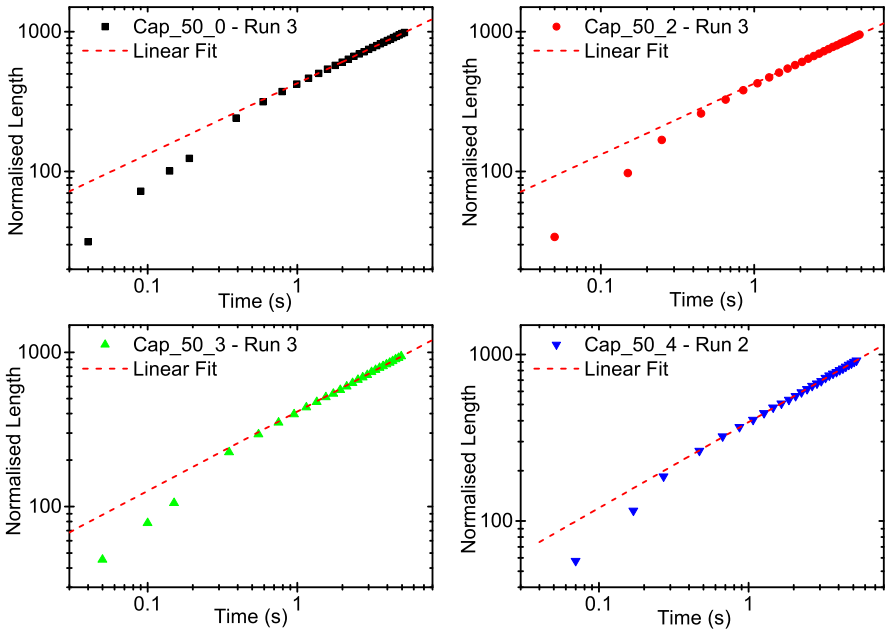


Figure 4.11.: Single runs of the different rough capillaries from Cap_50_-0 (smoothest) to Cap_50_4 (roughest) all presented with the linear fit at late times.

In addition to this discrepancy in the functional form, it is also clear that the changes in P_3 are significantly smaller than the changes in roughness, as observed from the difference in magnitude shown in Figure 4.12. This may be explained by realising that the capillaries utilised in this work are significantly wider than the nano-capillaries in the MD simulations. This implies that the relative effect of the capillary roughness may be reduced, as observed. Despite the correlation observed between the roughness and changes in the l vs. t relationship, it should be noted that variations in the wettability of the capillaries cannot be quantified. In the light of the observed pinning, it is clear that the capillary wettability treatment does change with time and that the intrinsic contact angle may be affected. Therefore, the changes outlined above may be related to this phenomenon and a separate methodology for experimentally deriving the actual contact angle is required.

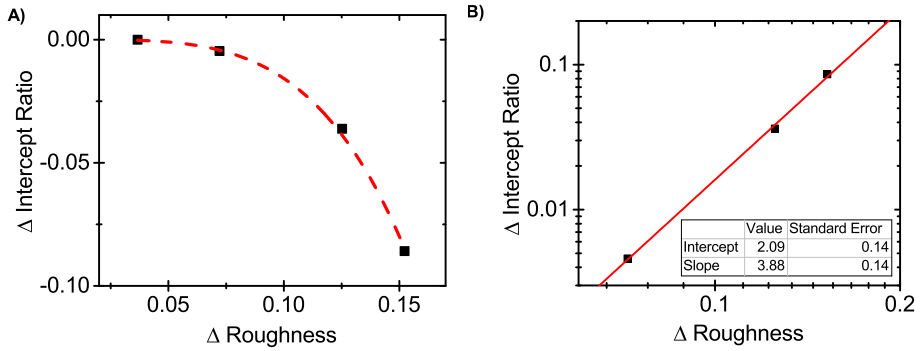


Figure 4.12.: Change in intercept vs change in capillary roughness.

4.4. Conclusions

Experiments were conducted to investigate the effect of wall roughness on capillary filling in comparison to the Lucas-Washburn prediction. To achieve this, different straight single capillaries were investigated. Initial experiments were conducted in smooth glass capillaries with a rectangular cross-section. Subsequently, capillaries were investigated in which the surface roughness was systematically altered.

All experiments were carried out with the capillary positioned horizontally at ambient temperature and pressure conditions. The following observations were noted:

1. Neither the smooth small (500 $\times$ 50 μm) nor large (4000 $\times$ 400 μm) glass capillaries reached the Lucas-Washburn regime. The results show that the capillary filling was quicker for the wider capillary, which is expected from the Lucas-Washburn equation. However, since the Lucas-Washburn regime was not reached, a quantitative analysis could not be conducted. Here a cross-over between the visco-inertial and L-W regimes is observed;

2. The advancing DI water meniscus became pinned within the roughest capillary;

3. A systematic decrease in the rate of imbibition with increasing roughness was observed. This decrease was not linear as in Stukan *et al.*[103] but quartic. However, in the light of the observed pinning, it is clear

that the capillary wettability changes with time and that the intrinsic contact angle may be affected;

4. Therefore, the changes outlined above may be related to this phenomenon and a separate methodology for experimentally deriving the actual contact angle is required.

5. Exploring the Young-Laplace Equation: Single Junctions

Abstract

The aim of this work is to improve our understanding of immiscible fluid displacement mechanisms at the pore scale in relation to capillary filling rules, especially for spontaneous imbibition. Using specifically designed single-junction micro-models, the role of pore geometry on fluid displacement during drainage and imbibition processes is investigated via quasi-static and spontaneous experiments under ambient conditions. The experimental results are directly compared to theory and Lattice Boltzmann Method (LBM) simulations. The experimental critical pore filling pressures observed for the quasi-static experiments agree well to those predicted by the Young-Laplace equation and follow the expected filling sequence. However, the experimental spontaneous imbibition results were found to be different from those predicted by the Young-Laplace equation: instead of entering the narrowest available downstream throat, the wetting phase enters an adjacent throat first. Thus, pore geometry plays a vital role as it becomes the main deciding factor in the displacement sequence. This observation may have serious implications for the prediction of displacement processes at the Darcy scale: current Pore Network Models (PNMs) adopt the Young-Laplace displacement sequence for spontaneous imbibition processes and may therefore need to be revised as they currently use the filling rules proposed by [8].

5.1. Introduction

Understanding the fundamentals of fluid displacement processes at the pore scale is essential. They are especially pertinent when needing to predict fluid migration in the subsurface for applications such as carbon sequestration and EOR. Due to the complexity of the pore space within porous media, it is often hard to unravel the contribution of varying factors, including pore geometry, surface roughness and wetting properties. Therefore, for this work well-defined single pore junctions have been investigated. Of particular interest are the displacement mechanisms controlling both drainage and imbibition [8, 107, 117, 139–141], especially with regards to capillary trapping during carbon sequestration. [26, 28, 142, 143]

The pioneering work of Lenormand *et al.* [8] investigated both drainage and imbibition fluid displacement events at the pore scale. They considered an array of straight throats of varying radii etched into resin to create a network. Multiple menisci displacement processes were identified: piston-like displacement, snap-off and pore body filling. When two immiscible fluids are present within the models (oil – air), Lenormand *et al.* [8] stated that the Young-Laplace equation was sufficient to describe all menisci displacement mechanisms:

$$P_C = P_{NWP} - P_{WP} = \gamma \cos\theta \left(\frac{1}{r_1} + \frac{1}{r_2} \right) \tag{5.1}$$

where P_C is the capillary pressure, P_{NW} and P_W are the pressures of the non-wetting and wetting phases, respectively, γ is the interfacial tension (IFT), θ is the contact angle and r_1 and r_2 are the principal radii of curvature.

Lenormand *et al.* [8] rigorously determined that drainage in single junctions indeed follows the Young-Laplace law. It was suggested that this is also the case for imbibition processes, but no direct evidence was provided [117]. Our aim is to directly investigate the displacement sequence for both drainage and imbibition processes using micro-fluidic methods. This is of great importance for the prediction of displacement processes at the Darcy (multi-pore) scale.

This chapter will focus on the displacement dynamics in a well-defined system of single pore geometries. The shape of the pore will be varied along with the size of the surrounding throats. Both primary drainage and imbibition processes have been investigated with two different techniques applied: quasi-static and dynamic, in order to investigate if displacement order is affected.

5.2. Experimental Set-up

All of the experiments in this chapter have been conducted using PMMA micro-models. The design and fabrication process for these models is discussed in Chapters 3.1 and 3.2, respectively. Three micro-model designs have been investigated. The first design consists of a pore body with throats of equal width. In contrast, for the second design the throats surrounding the pore body all have different widths to create a range of capillary entry pressures. The final model design is based on a pore body structure observed within a Berea sandstone. The dimensions for each of the micro-models will be given in the results section below.

Two imaging techniques were used during these experiments – inverted light microscopy (ILM) and high speed video microscopy (HSVM). The different microscopy techniques were used as each had their own advantages. The ILM allowed high resolution still images to be taken, but could not capture dynamic processes. On the other hand, the HSVM enabled dynamic processes to be captured easily and a larger field of view was possible; however, this reduced image resolution. A more detailed description of the equipment used for imaging is given in Chapter 3.3.

The experimental methodology has been subdivided into three sections: contact angle/throat geometry verification, drainage and imbibition methodology. Both the drainage and imbibition experiments were conducted via two techniques - quasi-static and dynamic – and each method will be described below. All experiments have been conducted at ambient temperature and pressure conditions.

Contact angle/throat geometry verification. Due to the unique fabrication of each individual micro-model, the contact angle and exact

throat geometry had to be determined individually. Initially the micro-models were imaged using ILM to ascertain the exact widths of the throats. The 20× objective was selected as it allowed the entire pore to be imaged at a high resolution. Figure 5.1 displays a pore body and surrounding throats of equal width taken using ILM. The calibrated AxioVision software was then used to measure the width of each throat, with an image resolution of 0.77 μm/pixel.

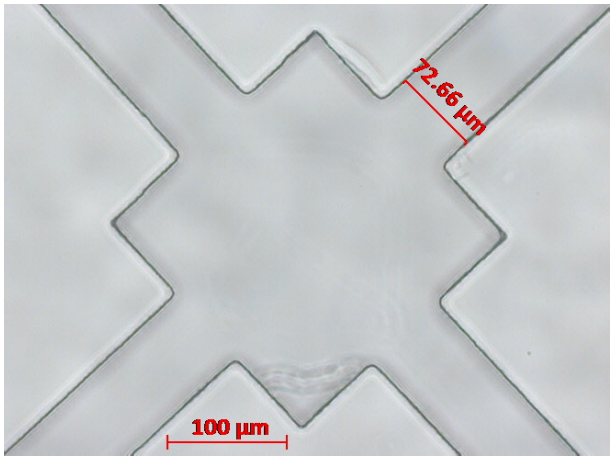


Figure 5.1.: Single junction micro-model with throat width measured using ILM and supporting software AxioVision.

As can be seen from Figure 5.1, the measured width of the throat was significantly lower than the prescribed width of 80 μm as given to the manufacturers. Discrepancies were measured between all throats and those selected for fabrication. Thus, if this was the case for the throat width, the same could be assumed for the etch depth. Therefore, the actual dimensions of each model were accurately determined before experiments began.

An approximate contact angle can be directly calculated from the image using a slightly altered version of Equation 2.5 to account for the rectangular cross-section of the throat: [144]

$$cos\theta = \frac{r_2}{(2r_C)} \tag{5.2}$$

where r_C is the radius of the superimposed circle, (see Figure 5.2). However, the contact angle was not calculated from images of the meniscus as

the image resolution at this scale was very pixilated, reducing the accuracy of the contact angle.

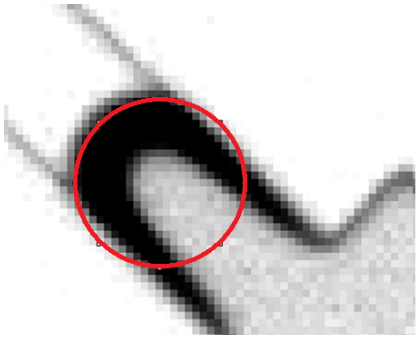


Figure 5.2.: Superimposed circle used to calculate the contact angle from static images. Open source software ImageJ was used to draw and measure the circle.

To determine the equilibrium contact angle experimentally, the following relationships were used:

$$P_C = \rho g h, \tag{5.3}$$

and

$$cos\theta = \frac{P_C(d * w)}{2\gamma(d + w),} \tag{5.4}$$

where P_C is the capillary pressure, g is the gravity constant, h is the height difference between the reservoir and the model; and d and w are the depth and width of the throat, respectively.

Thus, θ can be calculated by determining the height difference between the micro-model and reservoir when the meniscus is stationary within the micro-model throat. Experimentally this was achieved by connecting the model to a reservoir of the WP. The reservoir was then raised above the model to allow the WP to enter the model. Once the advancing the meniscus was in the main inlet throat, the reservoir was lowered slightly to slow the meniscus down. The reservoir was then lowered significantly once the meniscus entered the throat of interest. The height of the reservoir was then adjusted slightly until the meniscus remained stationary. Once the

meniscus had been stationary for 30 minutes it was assumed that the system had reached hydrostatic equilibrium and the height difference was recorded. Figure 5.3 displays the experimental set-up used to control P_C, including a schematic.

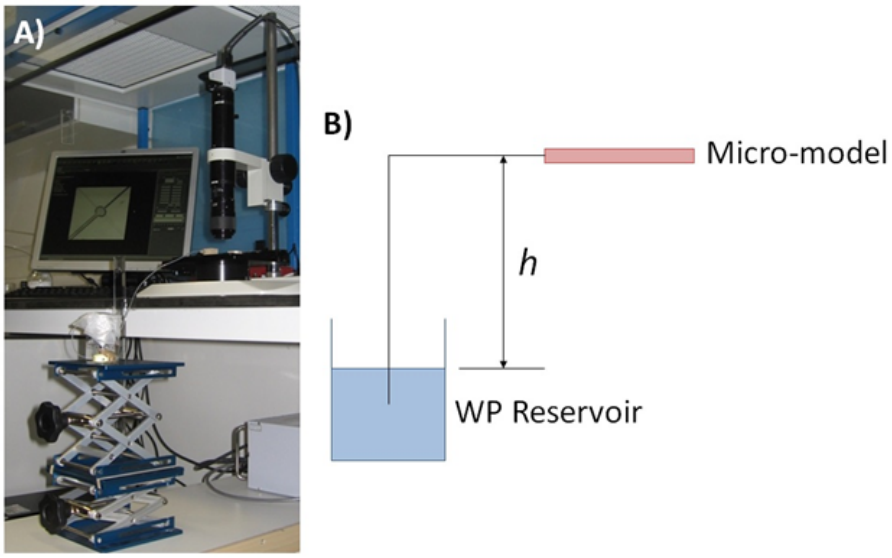


Figure 5.3.: A) Experimental set-up B) Schematic of experimental set-up illustrating the height measured.

Additionally, to ensure that the cross-sectional area of the micro-models was indeed rectangular, confocal microscopy was used. Initially a model was injected with a mixture of fluorescent resin and hardener. The mixture was allowed to set before cutting the micro-model to reveal the throat cross-section. Cutting the model allows imaging of the throat in the x-y plane where the confocal laser scanning microscope (CLSM) (LSM 700, Zeiss) has its highest resolution. The model was then set in more of the resin and hardener mixture, before being ground and polished mechanically (Ecomet 300 Pro and Automet 300 Pro, Buehler), to achieve an optically flat surface for imaging. The cross-sectional area of the throat is given in Figure 5.4. As can be seen the cross-section is indeed rectangular. Therefore the analysis can be confidently based on the depth and width of the throats. The sharp corners present in cross-section shown in Figure 5.4 will also allow WP films to develop and travel along the corners of model [145].

Primary drainage methodology. During drainage the micro-model is

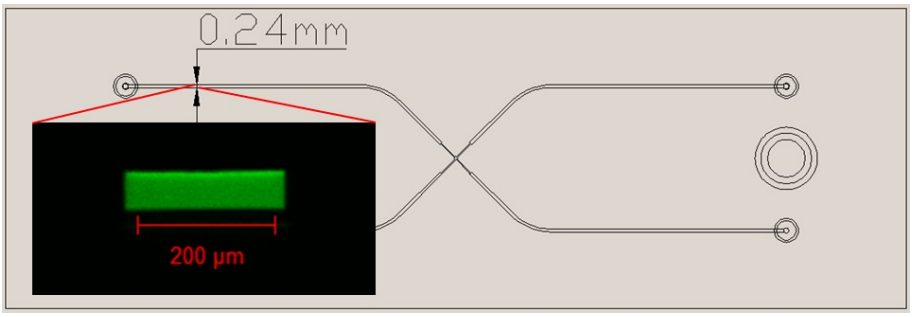


Figure 5.4.: Plan view of the PMMA micro-model design, including the cross-section of a micro-model imaged using the CLSM.

initially filled with the WP, before being displaced by the NWP. Two techniques were investigated – quasi-static and dynamic (forced) displacement. HSVM was used to image all drainage events.

The wetting phase fluid investigated during the drainage experiments was n-decane (viscosity (η_{Dec}) = 0.85 mPa s [146], γ = 0.024 N/m [147], density (ρ) = 730 kg/m^3, $\geq$ 99%, Sigma-Aldrich). The non-wetting phase fluids were DI water (η_{DI} = 0.89 mPa s, γ = 0.072 N/m, ρ = 1000 kg/m^3) and air (η_{Air} = 18.2 μPa s, ρ = 1.2 kg/m^3).

In the case of quasi-static drainage, the micro-model was connected to a reservoir of n-decane (wetting phase, WP). For this experiment, the narrowest channel was selected to connect to the reservoir. The model was connected to the reservoir via 1/16" tubing and flangeless PEEK fittings (XP-283, Kinesis). The narrowest throat was selected to ensure that the WP would drain into that throat last. Initially, the reservoir was positioned above the micro-model to ensure it was completely saturated with the WP. Once completely filled, the reservoir was lowered in incremental steps of 1 mm, corresponding to a pressure step of 7 Pa, every 15 minutes. This rate ensures that the pressure change is altered slowly to allow the system to reach hydrostatic equilibrium. Images were recorded once the air/n-decane interface was located in the largest throat. At this point the differential in height was recorded to calculate the capillary pressure at which drainage of that throat occurred. The reservoir was then lowered further to allow the non-wetting phase (NWP) to enter the remaining throats, recording the height for each drainage event.

For the forced drainage experiments, a programmable syringe pump (BS-8000, Braintree Scientific Ltd) was used to control the flow rate into the models. The micro-model was connected to a 1 ml syringe (BD Plasipak, BD300013) with the fluids passed through a Milipore filter (Millex-MP 0.22 μm, Millipore) to ensure the minimum amount of foreign particles reached the micro-model.

Primary Imbibition methodology. Like drainage, two techniques were implemented to investigate displacement mechanisms during imbibition – quasi-static and dynamic (spontaneous). In both cases, the micro-model was initially saturated with NWP which was then displaced by the WP.

During the quasi-static imbibition experiments the model was connected to a reservoir of n-decane. Depending on the displacement mechanism being investigated, the number of throats connected to the n-decane reservoir varied. For example in the case of an I1 pore filling event, three throats were connected to individual reservoirs, maintained at the same height. Individual reservoirs were used for ease of setting up the experiment. The reservoirs were then gradually raised, thereby increasing the wetting phase pressure (P_{WP}). The time step between each adjustment was 10 minutes to allow the system to achieve hydrostatic equilibrium.

Alternatively, the spontaneous imbibition experiments were achieved by placing a droplet of WP over the inlet of choice. A 1 ml syringe (BD Plasipak, BD300013) was used coupled with a filter unit (Millex-MP 0.22 μm, Millipore) to dispense the WP. The WP would then spontaneously imbibe into the model and HSVM was set to record once the meniscus was approaching the pore body. All spontaneous imbibition experiment videos were captured at 2000 fps.

5.3. Results and Discussion

The results are presented as a sequence of single snap-shot images illustrating the entire fluid displacement sequence clearly. In addition to the experimental results, corresponding LBM simulations have been conducted for certain experiments. The LBM simulations were conducted by Jianhui Yang.[148, 149] Both quasi-static and forced drainage results will be

presented in Section 5.3.1. Section 5.3.2 will discuss quasi-static and spontaneous imbibition results. Finally, conclusions will be given in Section 5.4.

5.3.1. Drainage Results

Two methods of performing drainage experiments were carried out: quasi-static and dynamic (forced). Both sets of experiments were conducted on a single square pore with unequal throats. The etch depth was 45 μm and the throat widths were 33, 51, 65 and 107 μm.

5.3.1.1. Quasi-static displacement.

Here the P_{WP} was decreased in small incremental, the position of the WP reservoir was moved in incremental steps of 1 mm, corresponding to a pressure step of 7 Pa. The fluid reservoir was connected to the model via the narrowest throat. By decreasing the P_{WP}, the NWP was able to enter the model. Figure 5.5 shows the displacement sequence of the quasi-static experiment. It can be seen that the largest throat was filled with NWP first before sequentially displacing WP from the throats following a sequence of decreasing throat radius. This displacement sequence is expected and predicted by the Young-Laplace law. Both the theoretical and experimental critical entry pressures were calculated for each throat, given in Table 5.1. In general, there was a good agreement between the two.

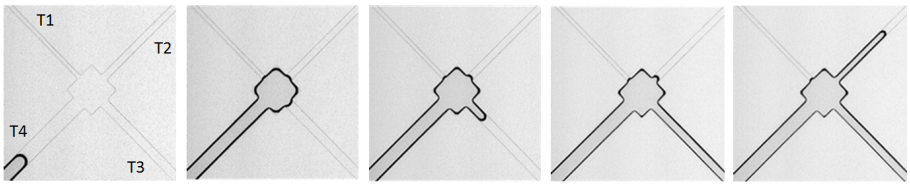


Figure 5.5.: Sequence of WP displacement during quasi-static primary drainage. The model was initially filled with WP (white) before being displaced by NWP (grey). The contact angle is 26°.

Table 5.1.: Critical pressures for drainage in throats 51, 65 and 107 μm in a model with unequal throat widths calculated via equation 5.1 and experimental data. Contact angle: 26°, etch depth: 45 μm, interfacial tension: 0.024N/m.

Throat	Young-Laplace Equation	Young-Laplace Critical Pressure (Pa)	Experimental Pressure (Pa)
4	$P_C = \gamma cos\theta \left(\frac{1}{r_1} + \frac{1}{r_2}\right)$	1357	1361 ± 7
3	$P_C = \gamma cos\theta \left(\frac{1}{r_1} + \frac{1}{r_2}\right)$	1620	1590 ± 7
2	$P_C = \gamma cos\theta \left(\frac{1}{r_1} + \frac{1}{r_2}\right)$	1794	1790 ± 7

Experimental error of ± 7 Pa was estimated from the 1 mm accuracy of the height of the reservoir.

5.3.1.2. Forced Drainage

Here the model was initially saturated with WP before the NWP was injected into the model at a constant flow rate. Two experiments were conducted with different wetting phases. Initially, DI water was selected as the NWP. DI water was injected into the model at 6 μl/hour. Images were captured at 500 fps. However, as can be seen in Figure 5.5, DI water was only weakly non-wetting. This is illustrated by the near 90° contact angle. Advancement of the DI water along the selected channel was slow, before more rapid expansion of the meniscus once inside the pore. This phenomenon is known as the Haines Jump [123, 150, 151]. The time taken for the meniscus to cross the pore was 88 ms. This time is similar to other experimental observations of Haines jumps in micro-model experiments of comparable junction size [123]. The displacement pathway observed in Figure 5.5 was that predicted by the Young-Laplace law, even though throats T1 and T3 are encountered by the NWP before T4, as their high capillary entry pressure prohibits entry.

Next, in order to observe a more strongly non-wetting system, the fluid pair was changed to *n*-decane/air. Here the model was initially filled with *n*-decane before air was injected at a constant flow rate of 0.5 ml/min. The displacement is shown in Figure 5.5 A. Similar to the DI water forced drainage experiments, a Haines jump was observed over the pore. Here the



Figure 5.6.: Forced drainage experiment with corresponding LBM simulations in which DI water is injected at a flow rate of 6μl/hour. The displacement pathway observed corresponds with the Young-Laplace law prediction; even though throats *1* and *3* are encountered by the NWP before *4*, their high capillary entry pressure prohibits entry.

time of the Haines jump was 12 ms.

Complementary LBM simulations were performed in exactly the same geometry as the experiments, see Figure 5.6. In addition to the geometry, Ca and contact angle were also matched to the experimental values. The Ca for this experiment was calculated to be 5.8 $\times 10^{-4}$ and the contact angle was 26°. When considering Ca at the pore scale, a value of 10^{-3} or smaller is reasonable as the viscous and capillary pressure drops are of the same magnitude [52]. As can be seen in both cases, the largest downstream throat was displaced by the NWP (light grey/blue in Figure 5.7) first.

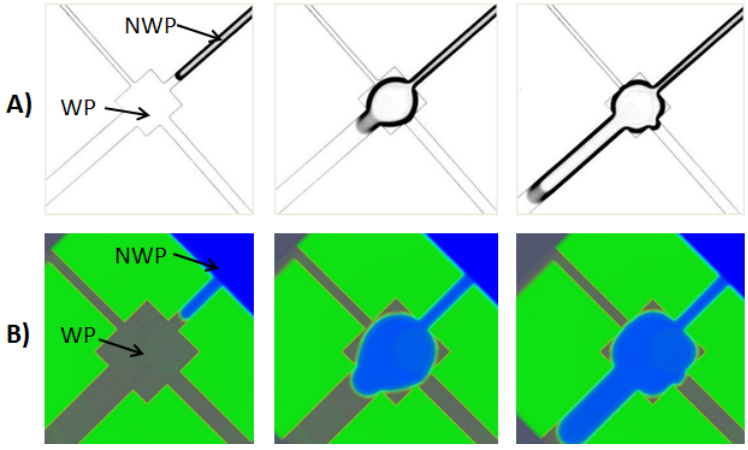


Figure 5.7.: Primary drainage images: A) experimental images of forced injection of NWP at 0.5 ml/min; B) corresponding LBM simulations. WP – wetting phase (n-decane). NWP – non-wetting phase (air).

Like the quasi-static experiments, the displacement sequence predicted by

the Young-Laplace law was observed in all the forced drainage experiments. Furthermore, good agreement can be seen between the simulations and experiments, thus validating the displacement sequence. Furthermore, only piston-like displacement was observed in all the experiments, as expected.

5.3.2. Imbibition

Our hypothesis is that imbibition is controlled by pore geometry and displacement processes are more complex compared to drainage. In addition to piston-like displacement, snap-off and pore filling events can be the displacement mechanisms. As in the case of the drainage experiments, both quasi-static and dynamic (spontaneous) imbibition experiments were conducted. Experiments were conducted in a range of models – a square pore with equal throat widths, a more complex pore shape with unequal throat widths and a Berea pore. The dimensions of the models will be given below.

5.3.2.1. Quasi-static imbibition

Initially experiments were conducted on models in which the throat radii were equal (etch depth: 56 μm, throat width: 73 μm, pore width: 238 μm). Here I1, I2, I2A and I3 pore filling events were investigated, shown in Figure 5.8. For I1 the WP is located in three throats. Once the critical pressure of the pore is overcome, the final throat can be filled. For each pore filling situation, the critical pressure was calculated. Both the theoretical and experimental filling values are presented in Table 5.2. The critical radii were modified for each pore filling event, with the horizontal critical radii shown in red in Figure 5.8. Depending on the shape of the menisci, the Young-Laplace equation was also modified. The modifications are given in Table 5.2. In the case of an I2A pore filling event, the critical meniscus is straight; therefore, only the meniscus in the depth direction (r_1) was influencing the pore filling event as r_2 is assumed to tend to infinity. For I3 filling events, the meniscus bulged out into the pore, thus the critical radius (r_2) is negative.

As can be seen in Table 5.2, all of the theoretical and experimentally determined critical pressures are close in value. Good agreement was achieved

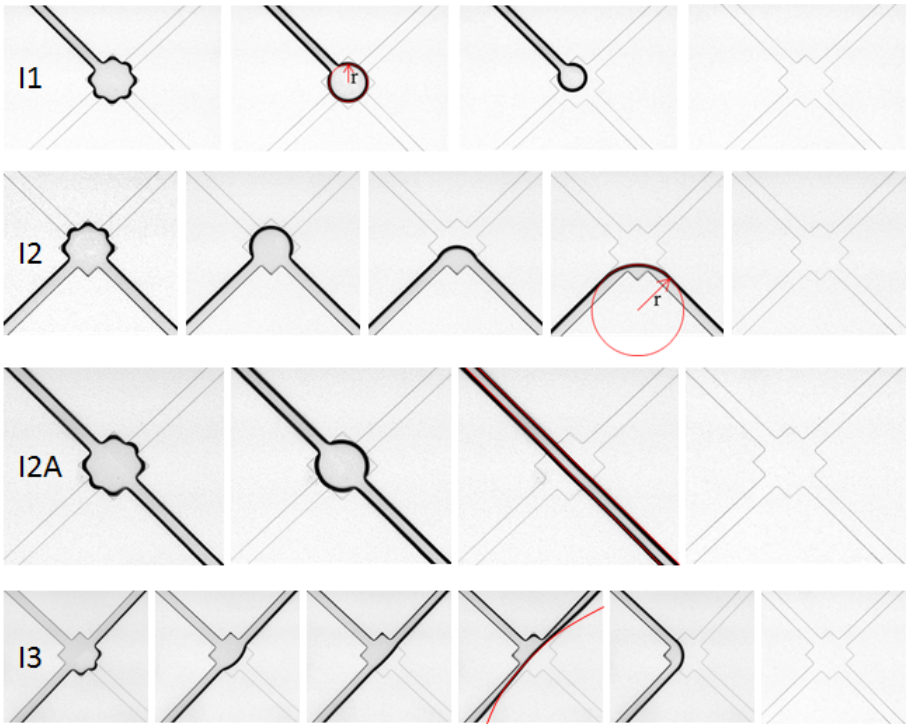


Figure 5.8.: Quasi-static I1, I2, I2A and I3 imbibition experimental results (WP is white, NWP grey). The critical radii used to calculate the displacement pressures for each case are also illustrated in red.

since the exact pore geometry is known; the meniscus shape is clearly visible, allowing the critical radii to be well defined.

Quasi-static experiments were also conducted in a micro-model with unequal throat widths (etch depth: 55 μm, throat widths: 27, 47, 60, 100 μm pore: 155, 236 μm). The contact angle of this model was found to be 16°. Using the exact pore geometry and contact angle, the predicted displacement sequence using the Young-Laplace equation is shown in Figure 5.9 . The first displacement event predicted to occur was snap-off (P_S) within the narrowest throat at 1240 Pa. Next the pore body was predicted to fill via piston like displacement (P_P) at 869 Pa. The experimental value at which snap-off occurred was 1238.9 $\pm$ 7 Pa, which is very similar to the theoretical value. The pore body was filled by piston-like displacement at 880.8 $\pm$ 7 Pa. The experimental error was $\pm$ 7 Pa due to the 1mm accuracy that could be achieved with the height measurements. Here snap-off was able to occur as

Table 5.2.: Critical pressures for I1, I2, I2A and I3 pore filling events within a micro-model with equal throat widths. Critical pressures calculated via equation 5.1 and experimental data. Contact Angle: 28°, etch depth: 56 μm, throat width: 73 μm, pore width: 238 μm, γ: 0.024 N/m.

Throat	Young-Laplace Equation	Young-Laplace Critical Pressure (Pa)	Experimental Pressure (Pa)
I1	$P_p = \gamma cos\theta \left(\frac{1}{r_1} + \frac{1}{r_2}\right)$	931	932 ± 7
I2	$P_p = \gamma cos\theta \left(\frac{1}{r_1} + \frac{1}{r_2}\right)$	838	838 ± 7
I2A	$P_p = \gamma cos\theta \left(\frac{1}{r_1}\right)$	745	754 ± 7
I3	$P_p = \gamma cos\theta \left(\frac{1}{r_1} + \frac{1}{r_2}\right)$	709	708 ± 7

An experimental error of ± 7 Pa was estimated from the 1 mm accuracy of the height of the reservoir.

there was time for the advancing WP films to develop ahead of the main meniscus. These films gradually swell and become unstable, causing snap-off [152, 153]. Figure 5.10 displays the filling sequence and the wetting films can be clearly seen as the darker lines outlining the model geometry. This sequence was as predicted, using both piston-like and snap-off equations, discussed in Chapter 2.

5.3.2.2. Spontaneous imbibition

The spontaneous imbibition experiments were restricted to I3 displacement processes. This was due to the difficulties in getting the advancing menisci to arrive at the pore body simultaneously for I1, I2 and I2A experiments. In all of these experiments no external pressure has been applied.

Initial experiments were conducted in geometries with equal throat widths surrounding the pore body. It was observed that the displacement pathway varied during different experimental tests. Figure 5.11 illustrates the different pathways taken within one model over different runs.

Reasons for these different displacement pathway could be due to subtleties in the advancing meniscus. These changes could be caused due to a particle of dirt furthermore upstream – causing a slight delay in that side

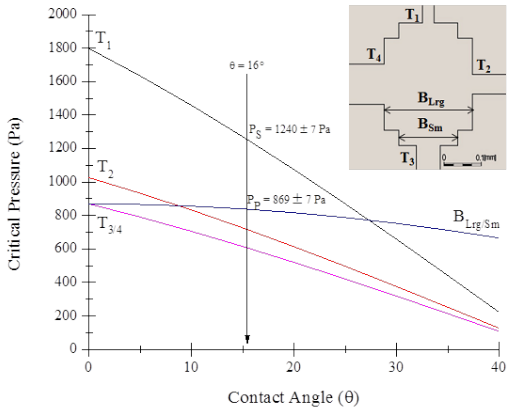


Figure 5.9.: Predicted displacement sequence for Quasi-static I3 imbibition using the Young-Laplace equation for a contact angle of 16°, with the narrowest throat filling first via snap-off (P_S) followed by the body filling through piston-like displacement (P_P).

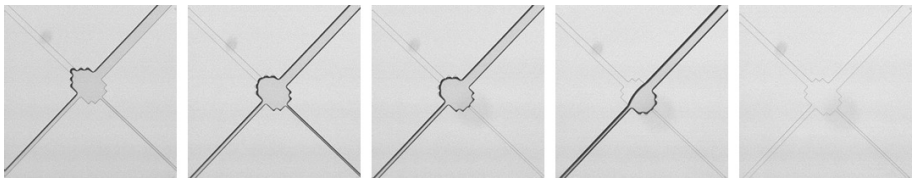


Figure 5.10.: Quasi-static I3 imbibition experimental results (WP: white, NWP: grey, Wetting films: black). Snap-off occurs in the narrowest throat before the meniscus enters the pore as predicted by the Young-Laplace equation.

of the meniscus entering the pore body.

Next spontaneous imbibition experiments were conducted in a geometry in which the throats surrounding the pore body varied in size, creating a range of capillary entry pressures. Figure 5.12 shows the displacement pathway for an I3 pore body filling event. Based on the predictions from the Young-Laplace equation, it was expected that the WP would fill the narrowest throat first. However, Figure 5.12 shows this was not the case. Instead of filling T1, an adjacent throat (T2) was filled first. This was because the WP films did not have sufficient time to develop ahead of the advancing meniscus; therefore snap-off was not possible. Thus, the Young-Laplace equation is insufficient to predict the order of filling and therefore, the throat the

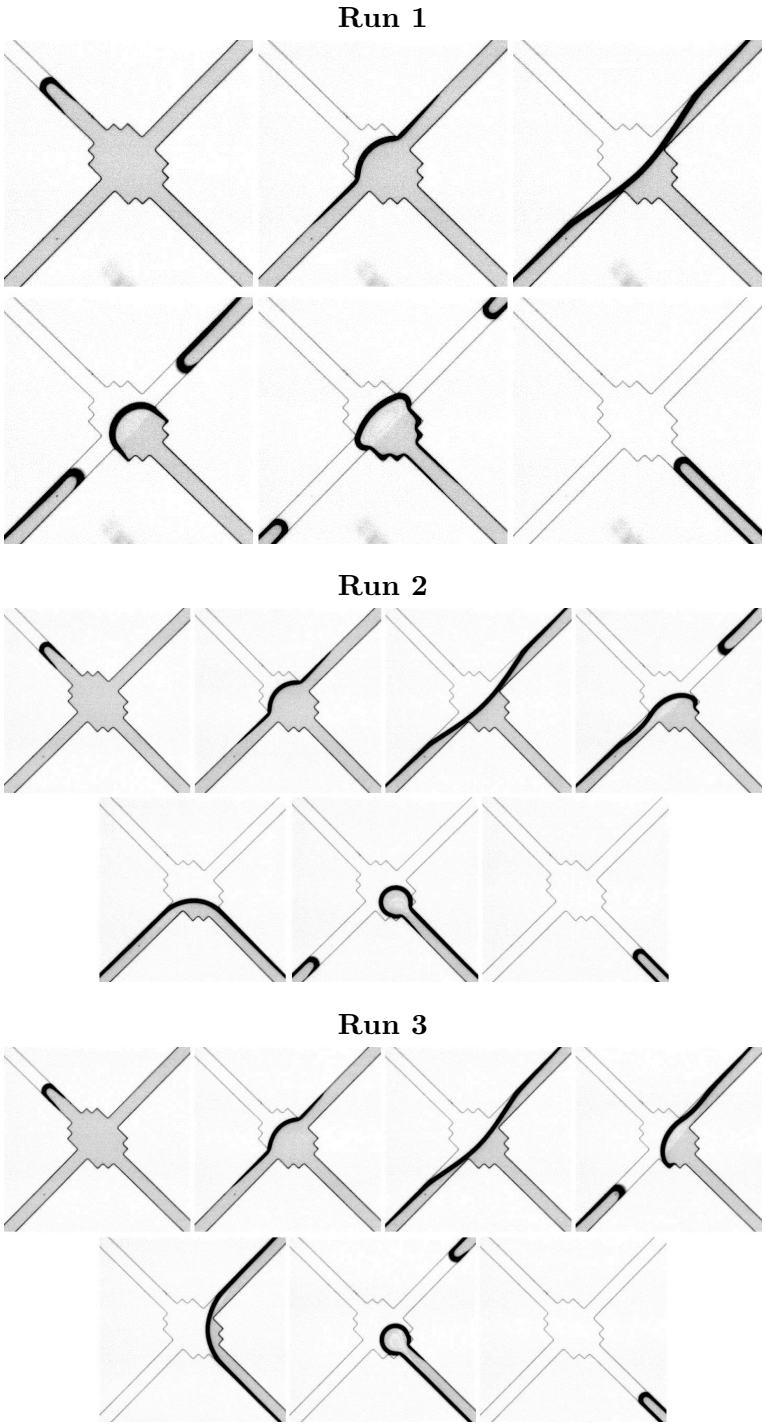


Figure 5.11.: Quasi-static I3 imbibition experimental results (WP: white, NWP: grey, Wetting films: black). Snap-off occurs in the narrowest throat before the meniscus enters the pore as predicted by the Young-Laplace equation.

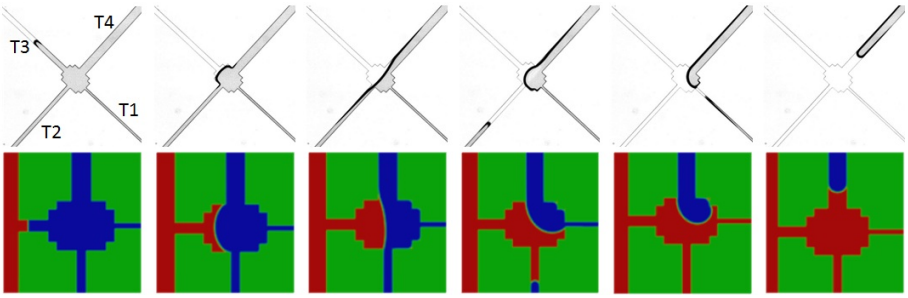


Figure 5.12.: Spontaneous I3 imbibition experimental results (top row, throat widths: r_2(T1) = 27 μm, r_2(T2) = 47 μm, r_2(T3) = 60 μm, r_2(T4) = 100 μm, etch depth = 55 μm), with the corresponding LBM simulations (bottom row); here the WP travels down the adjacent throat first. This behaviour is not predicted by the Young-Laplace law (5.1).

meniscus encounters first is filled first. This is understandable, as once the capillary entry pressure of the pore body has been overcome, the advancing meniscus was able to enter any downstream throat as the critical entry pressures had already been exceeded.

I3 spontaneous imbibition experiments were also conducted in a micromodel with a pore shape more representative of actual rock pore space. Figure 5.13 displays the I3 displacement sequence in a pore shape extracted from a Berea thin section. The corresponding LBM simulations are also presented for comparison. The displacement sequence in both the experiment and LBM simulation correspond to each other well. Both the spontaneous imbibition experiments and LBM simulations directly confirm the suggestion proposed by Lenormand [117]: when no WP films are present, the advancing meniscus will advance down an adjacent throat first. Therefore, displacement pathways do not always occur in the order predicted by the Young-Laplace equation. Hence, the pore body geometry becomes a key factor in determining in which order the downstream throats will fill.

Finally, analysis has been conducted on tracking the meniscus in Figure 5.14 (Throat 3) as a function of time. Figure 5.14 illustrates that the displacement of the meniscus scales linearly with time. Initially, this was surprising as the viscosity ratio between the WP and NWP was approximately 50. This value should be large enough to observe Lucas-Washburn $\sqrt{time}$

behaviour. LBM simulations have been conducted by Ioannis Zacharoudiou in which displacement as a function of time has been calculated. The purpose was to examine the dynamics of capillary filling and question if this affects the pore body filling sequence once the interface reaches the pore body. The dimensional considerations for dynamic capillary filling, including the Ohnesorge number Oh, have been detailed in Chapter 2.1.4.

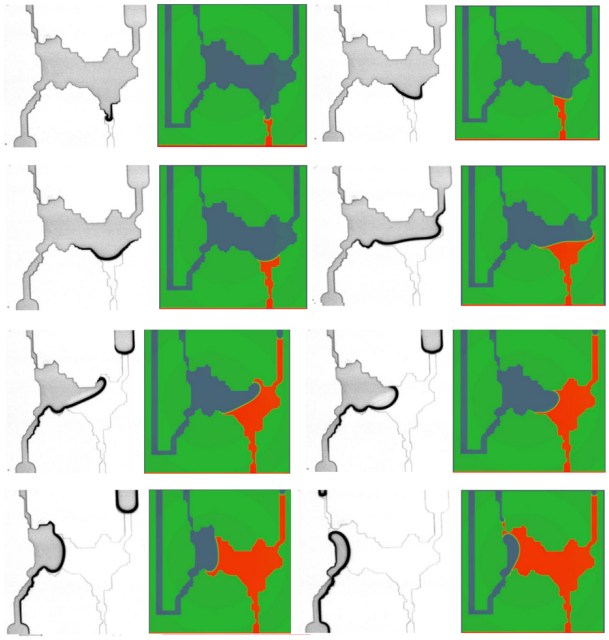


Figure 5.13.: Spontaneous Imbibition I3 experiment in a pore shape representative of Berea sandstone with corresponding LBM simulations. Here the WP travels down the adjacent throat first. This behaviour is not predicted by the Young-Laplace law (5.1).

In the experiments the Oh was $\sim 3.8 \times 10^{-2}$, whilst the LBM simulations varied the range of 7.3×10^{-2} to 2.1. The variation in Oh number was achieved primarily by varying the viscosities of the two fluids, whilst maintaining the viscosity ratio fixed at $r_n = 50.5$. As shown in Figure 5.14 B, LBM $sims_1$ had an Oh number of 2.1 and displayed a $l \sim t^{0.5}$ dependency. As the Oh number decreases, there is no longer time to reach the Lucas-Washburn regime. The LBM simulation ($Oh = 7.3 \times 10^{-2}$) is in the linear regime $l \sim t$. Therefore, as the experimental Oh value is even smaller than in the LBM $sims_3$, the linear dependency is justified.

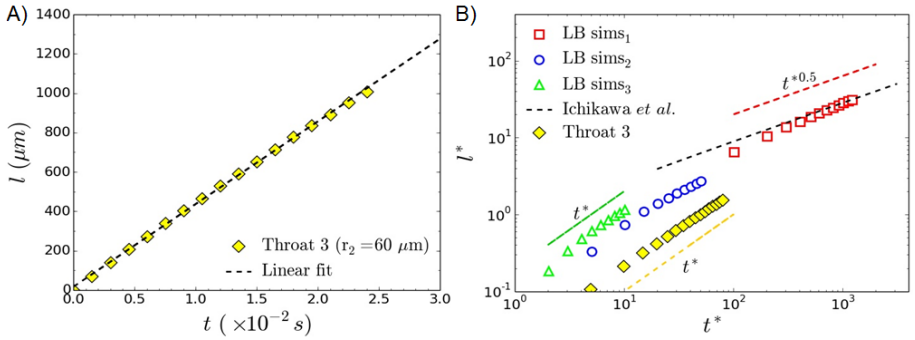


Figure 5.14.: A) Interface tracking of the meniscus in throat 3 as a function of time for the experiments. B) Rescaled length as a function of dimensionless time for both experiment and LB simulations. Ohnesorge numbers: Oh=2.1 (sims_1), Oh=1.6 $\times 10^{-1}$ (sims_2), $Oh = 7.3 \times 10^{-2}$ (sims_3).

5.4. Conclusions

Experiments were conducted to investigate the role of pore geometry on fluid displacement mechanisms for both drainage and imbibition processes. To achieve this, single junction micro-models were fabricated with varying pore shapes and a range of throat dimensions to achieve a range of capillary entry pressures.

During both quasi-static and dynamic primary drainage experiments the displacement pathway was as predicted by the Young-Laplace law – the widest downstream throat filled first. The LBM simulations also followed these displacement predictions. Furthermore, the theoretical and experimental critical pressures for the displacement events during quasi-static drainage were in good agreement. Therefore, the rules currently employed within PNMs for drainage should predict displacement processes correctly.

The quasi-static and spontaneous imbibition experiments produced different results. The quasi-static results were in line with Young-Laplace predictions. The calculated theoretical and experimental critical pressures for the different quasi-static displacement events were similar. Therefore, quasi-static displacement pathways can be predicted by the Young-Laplace equation.

However, the displacement pathway experimentally observed during spon-

taneous imbibition did not follow the Young-Laplace prediction. Instead of filling the narrowest throat first, the advancing meniscus made contact with the corner of the pore and traveled down an adjacent throat first. The reason is that, once the critical entry pressure of the pore is exceeded, any downstream throat is able to fill. Furthermore, due to the short time scales, a WP film did not have chance to develop ahead of the advancing meniscus, suppressing snap-off. This displacement pathway was suggested by Lenormand [117], but no direct evidence was given. Here, the hypothesis has been proved, for the first time, both in experimental and LBM simulation results. Therefore, pore geometry and the location of WP films is very important when predicting displacement pathways. The implications of the absence of WP films within PNMs has not been investigated.

Predicting the displacement pathways in well defined micro-models is very different to actual porous media due to the complexity of the pore structures. In micro-models the critical radii are known, however, implementing this into real pore networks requires the capibility of establishing pore shape. Computational studies [154, 155] have begun investigating meniscus shapes in 3D structures to establish displacement pathways.

6. 'Abstract' Network Models

Abstract

The aim of this work is to expand upon the findings of Chapter 5. By examining whether the observed divergence from the expectations of the Young-Laplace equation in single junction displacement pathways affect more complex network structures. In particular, how the residual saturation of networks may be altered by this observation during spontaneous imbibition. This of great importance in comprehending how much CO_2 can be stored once injection has ceased. To generate more realistic subsurface conditions supercritical CO_2 experiments should be conducted. Such experiments require micro-models capable of withstanding high pressures. To achieve this glass micro-models have been fabricated and tested up to 100 bar.

6.1. Introduction

To investigate whether the displacement pathways observed during spontaneous imbibition experiments in Chapter 5 have an impact at a larger scale it is necessary to consider networks of connected pore and throats. Therefore, two more complicated 'abstract' network micro-models have been designed and fabricated. The initial micro-model design considered is a continuation of the single junctions in which the four throat sizes (30, 50, 64 and 104 μm) have been randomly distributed to create a model of an appropriate size. These models were fabricated in PMMA and the design is given below in Section 6.2. Due to experimental difficulties outlined below, the 'abstract' PMMA model design required alteration. Therefore, an additional glass micro-model was fabricated with a matrix design based on the pore and throat size distribution of a Berea sandstone. The design and fabrication

process for this model are given in Section 3.1 and 3.2, respectively.

A detailed description of the experimental set-up for this set of experiments will be given in Section 6.2. The results will be presented in Section 6.3, followed by conclusions in Section 6.4.

6.2. Experimental Set-up

The 'abstract' PMMA micro-model design is given in Figure 6.1. Here the four throat widths (30, 50, 64 and 104 μm) used in the single junctions have been randomly distributed to create a large network model. This allows exploration of the effects observed in the single junctions but now in a matrix of junctions. The design of the glass micro-model can be found in Chapter 3.1.

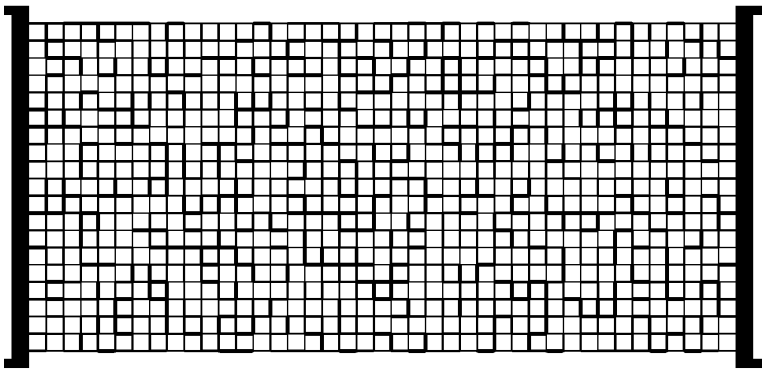


Figure 6.1.: 'Abstract' network model design fabricated in PMMA. Four throat widths (30, 50, 64 and 104 μm) randomly distributed to create a larger model.

The experiments for both the PMMA and glass micro-models have been captured using the DSLR camera as it provided the largest field of view, enabling the entire micro-model to be imaged at once. A more detailed description of the DSLR camera set-up is given in Chapter 3.3.

The experimental methodology has been subdivided into three sections: gravity driven drainage/imbibition experiments, image processing and pressure testing of glass micro-models. Both drainage and imbibition experiments were conducted via quasi-static methods. The drainage and imbibi-

tion results presented were conducted at ambient temperature and pressure. Furthermore, initial pressure testing has been conducted on the glass micro-models validating the potential to conduct experiments at pressures up to 100 bar.

Gravity driven drainage/imbibition methodology. All of the experiments were conducted with the micro-model positioned horizontally at ambient temperature and pressure conditions. The fluids investigated were hexadecane (viscosity (η_H) = 3 mPa s, interfacial tension (γ) = 0.027 N/m, density (ρ_H) = 770 kg/m^3) and DI water (η_{DI} = 0.89 mPa s, γ = 0.072 N/m, ρ_{DI} = 1000 kg/m^3) to replicate the single junction studies.

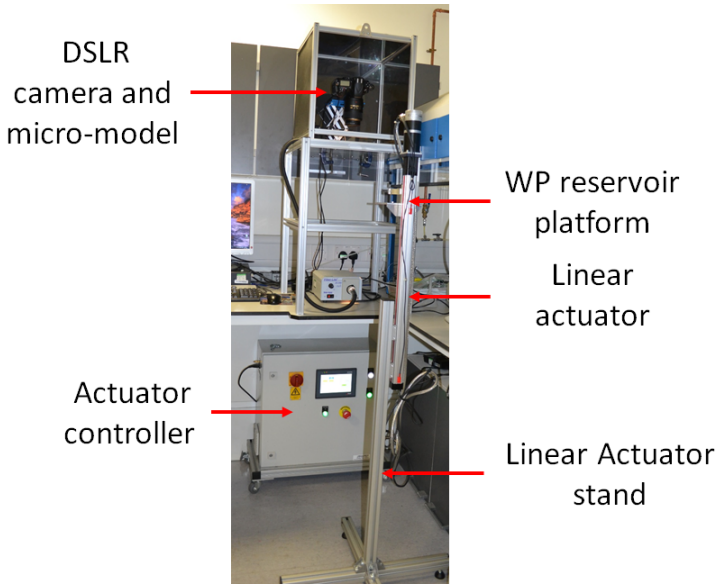


Figure 6.2.: Experimental set-up of the gravity driven flow micro-model experiments.

The decision to use gravity driven flow was made as it allows more accurate control of the capillary pressure within the model compared to injection pumps. Furthermore, injection pumps tend to be operated by a stepper motor, with one step administrating a volume of fluid greater than the entire model. However, to exceed the capillary entry pressures of the models, the entire micro-model set-up needed to be positioned above the fluid reservoir requiring a bespoke rack and stand to securely hold the DSLR camera and micro-model. In Figure 6.3 A the modified camera stand including the G-clamps (542-447, RS Components Ltd) is displayed. This stand is then

positioned on the rack shown in Figure 6.2.

With the micro-model set at a constant height to change the capillary pressure, it is necessary to change the wetting phase (WP) reservoir height. This is achieved using a specially commissioned linear actuator (MicroMech), as shown in 6.2. This allows accurate, stable control of the WP phase reservoir height. Furthermore, it allows automation of the experimental process.

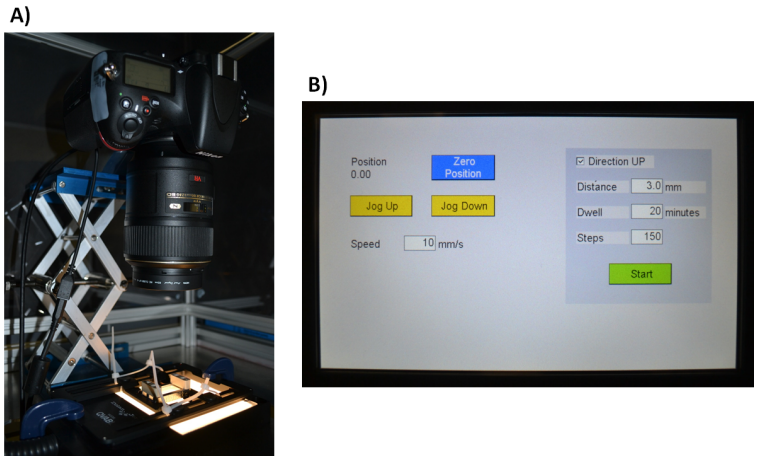


Figure 6.3.: A) Modified camera stand B) Linear actuator control panel.

Initially, the micro-model is fully saturated with the WP via a programmable syringe pump (BS-8000, Braintree Scientific Ltd). The injected fluid enters the model at the end opposite to that connected to the WP reservoir. Whilst injecting, all air bubbles must be expelled from the model. When ready, the linear actuator can then be programmed to either travel up or down at predefined step distances, dwell time and number of steps using the control panel shown in Figure 6.3 B. The DSLR camera can also be programmed to image the micro-model at set intervals via specialised software (Camera Control Pro2). During all of the experiments the system was captured just before the next pressure step occurred, allowing maximum time for the model to equilibrate.

Image Processing. In order to extract quantitative data from the captured images, image processing is required. All the image processing was carried out in ImageJ (open source software). Initially all the images were cropped and registered using the in-built registration function. Due to a

slight gradient on the back light all the captured images had a slight colour gradient from left to right. Before image segmentation could occur, this experimental artefact was removed using the Background Correction macro shown in Appendix B. Once removed, the difference between the image of interest and the 100% saturated micro-model was calculated using the Image Variation macro, shown in Appendix B. The resulting image was then segmented with the NWP shown in white using the Image Segmentation shown in Appendix B.

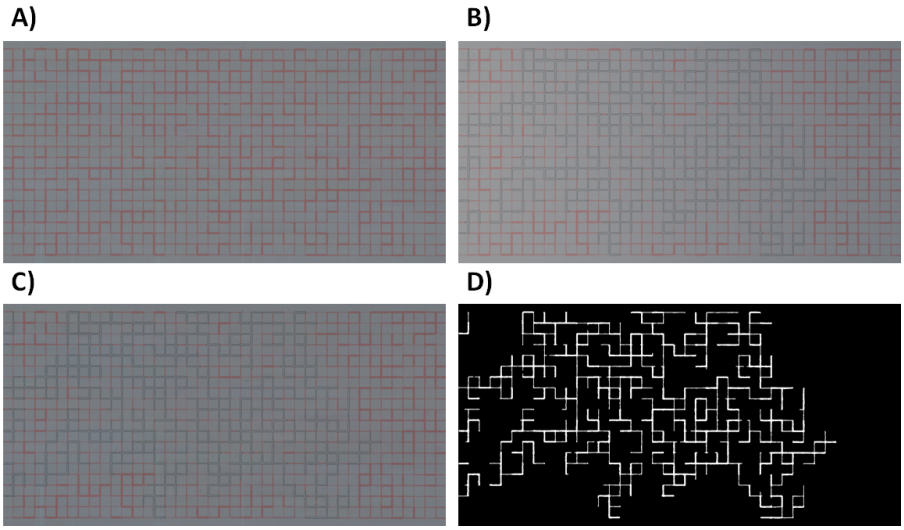


Figure 6.4.: A) Image of micro-model 100 % saturated with *n*-decane + Oil Red EGN B) Micro-model after drainage C) Micro-model after drainage + Background correction applied D) Segmented image, white - air (non-wetting phase, NWP).

Glass micro-model pressure testing. For supercritical CO_2 ($scCO_2$) experiments to be conducted, the glass micro-models had to pressure tested. Pressure testing was conducted with DI water and the micro-models were tested to 100 bar, to ensure that in future experiments $scCO_2$ can be used in the supercritical regime.[156] During testing, one inlet was connected to a Quizix pump (Quizix Q5000 Pump System, Chandler Engineering) whilst the opposite outlet was connected to a back pressure regulator.

Gradually the pressure was built up with DI water against the back pressure regulator. Initial pressure tests with the micro-model holder provided by The Dolomite Centre Ltd failed at pressures well below 100 bar, due

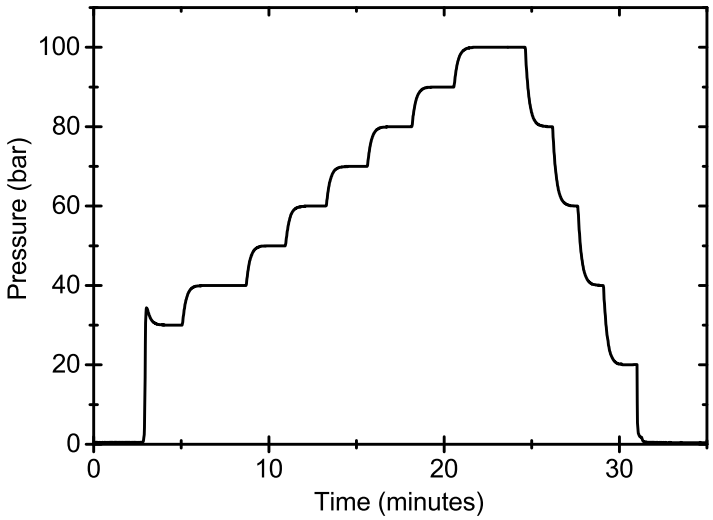


Figure 6.5.: Pressure testing of glass micro-model.

to the plastic ferrule failing to seal properly on the glass micro-model. To alleviate this problem, another micro-model holder was designed and made by the internal Imperial College workshop. The new design is provided in Section 3.1. With this new holder, the micro-models have been successfully pressure tested to 100 bar (see Figure 6.5).

6.3. Results and Discussion

6.3.1. PMMA micro-models

Initial 'abstract' network model experiments were conducted using the PMMA models at ambient temperature and pressure. In these experiments the WP was n–decane with the addition of Oil Red EGN (234117-25G, Sigma-Aldrich) to allow easier image segmentation. Here the model was initially saturated with the n-decane before the WP reservoir was lowered, allowing the non-wetting phase (NWP, air) to enter the network matrix. The reservoir was lowered in incremental steps of 1 mm, corresponding to a pressure step of 10 Pa, every 30 minutes. Images of the system were taken just before each pressure step. Figure 6.6 shows the pressure/saturation curve for a drainage/imbibition experiment calculated from segmented im-

ages. Several key points can be observed from Figure 6.6. During drainage there are very few pressure steps due to the limited capillary entry pressure values associated with the four throat sizes used. Furthermore, drainage was stopped before the capillary entry pressure of the narrowest throat was exceeded to prohibit breakthrough into the fracture channel. This was required so that imbibition would begin with a flat front. It is this limitation that caused the limited saturation values.

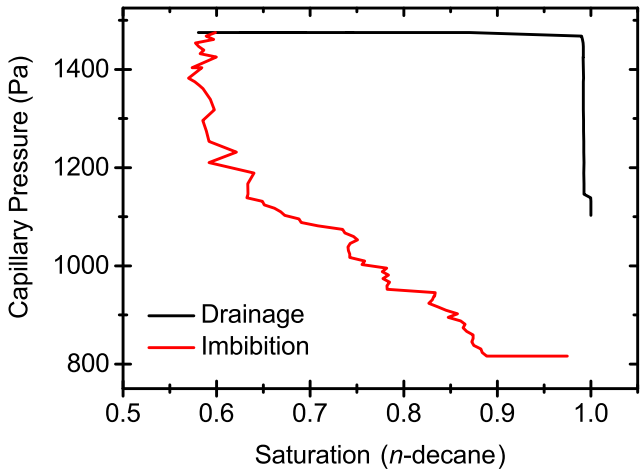


Figure 6.6.: Saturation curve for PMMA micro-model drainage/imbibition cycle.

6.3.2. Glass micro-models

After conducting these experiments and observing the results, it was decided to change the design of the micro-models for the glass models. These changes include the addition of a 'porous plate' to allow greater saturation values to be achieved. Furthermore, a greater range of pore and throat widths were used based on the distribution of a Berea sandstone. A more detailed description of these changes has been provided in Section 3.1.

Initial ambient experiments have been conducted using the glass micro-models. In these experiments, the WP was DI water with the addition of Methyl Blue (95290-5G, Sigma-Aldrich) to allow easier image segmentation. During initial experiments the WP reservoir was lowered in 1 mm

increments every 30 minutes. However, several challenges were encountered which are in the process of being resolved. Some of these issues are illustrated in Figure 6.7. These images have not been background corrected, illustrating the extent to which the back light affects the captured images. Figure 6.7 B shows the system at the end of drainage, whilst Figure 6.7 C, shows the system during imbibition. It was observed that the system continued to drain even when imbibition had begun. This suggests that the time interval between each pressure step is too short and equilibrium has not been reached. This could potentially be an issue for later comparisons with PNMs, which assume hydrostatic equilibrium. At the currently applied experimental reservoir stepping rate, a full drainage/imbibition experiment lasts approximately 10 days, which is a significant period of time to retain constant experimental parameters. Therefore, increasing the time of the experiment may raise further difficulties. Clearly, it is essential to systematically explore the required time for equilibration to occur. However, a major limiting factor in increasing the experimental time scale is the observation of the dye fading with time. Indeed, by the end of the 10 days, the Methyl Blue dye had faded so significantly that image segmentation was not possible. Furthermore, it appears the dye may be adsorbing on the walls of the model, suggested by the dark outlines of the pore structures even when no fluid is present. This is an issue for image analysis and also could be altering the wettability of the models.

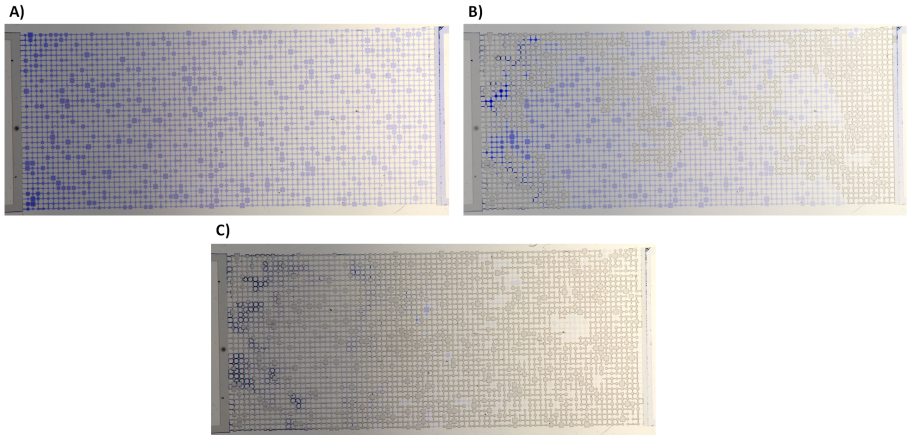


Figure 6.7.: A) Image of DI water + Methyl Blue saturated glass micro-model before drainage/imbibition began B) Micro-model at the end of drainage C) Micro-model after imbibition.

6.4. Conclusions

In conclusion, preliminary experiments were carried out to explore the large-scale drainage and imbibition behaviour in network models. The experimental methodology and set-up has been shown to work, although some refinement is still necessary. Initial experiments indicated that the original PMMA network model, of limited throat width distribution, needed to be modified due to the limited capillary entry pressures and saturation values. To achieve this the matrix design of the new glass micro-models included a wider range of capillary entry pressures based on the distribution of a Berea sandstone. Furthermore, a 'porous plate' structure was added to one end to allow greater NWP saturations to be achieved. Ambient condition tests in the glass micro-models raised issues with regards to achieving equilibrium and the selected dye fading over time which require further research.

Finally, the glass micro-models proved to be able to withstand pressures of up to 100 bar. This implies that future experiments involving $scCO_2$ are possible in these models. Such experiments would be very interesting for comparison of residual saturation results with those of PNMs using the same network design.

7. Phase Identification using Raman Spectroscopy within Micro-models

Abstract

One method for enhanced oil recovery (EOR) is the injection of surfactants in the reservoir to improve oil recovery. This works by decreasing the interfacial tension (IFT) between the residual oil and brine, as discussed in Chapter 2.2. This process is improved if a micro-emulsion forms between the surfactant and the oil causing ultra-low IFT. Whilst there is a general understanding of how the flow properties of the oil phase behaves subsurface, understanding the flow properties of the micro-emulsion phase is lacking [157]. The aim of this work is to consider a Raman spectroscopy methodology to investigate these properties. Furthermore, to achieve the best recovery factor, surfactants need to be designed for individual injection sites. However, there are several factors which need to be taken into consideration when planning an EOR injection project: the crude oil present, the salinity of the brine, temperature and pressure. Additional considerations include sweep efficiency, surfactant retention, concentration, and commercial availability of the surfactants [12].

The process of understanding the formation of the micro-emulsion uses solely in-lab techniques and their applicability to real reservoirs is not completely comprehended. Therefore, a high fidelity technique which can accurately determine the spatial and chemical distribution of the phases would be ideal. Raman spectroscopy appears an excellent potential solution as it should be capable of achieving this. In this preliminary work, we have begun to consider the capabilities of Raman spectroscopy for this task.

7.1. Introduction

In micro-model experiments phase identification is very challenging. Currently, the addition of a dye to at least one phase is used to aid phase identification. However, this raises issues of whether the dye alters the IFT between the phases and may also adsorb on the walls of the model changing wettability.[158] Furthermore, identification of concentration gradients for multicomponent phases is not feasible by these optical methods. This is due to the difficulties in visualising the different phases.

Micro-emulsions add a further complication to this situation as they represent a third homogeneous phase. Raman spectroscopy offers a novel way to distinguish between species and phases, including formation of micro-emulsions, without the need to add a dye.

7.1.1. Introduction to Raman Spectroscopy

Raman spectroscopy is a powerful technique which has been gaining interest in recent years, with applications ranging from analytical chemistry to forensic science and even deployment in the field including deep-sea hydrothermal vents [159] and missions to Mars.[160] Many micro-fluidic applications which have utilised Raman spectroscopy have been in the biological field, including: DNA, pharmaceuticals and forensic science.[161] However, there is no literature available which addresses EOR processes within micro-models using Raman spectroscopy to probe the fluid phases.

The first theoretical prediction of inelastic scattering by optical photons (Raman Scattering) is attributed to the Austrian physicist Adolf Smekal in 1923, [162] though, it would be a further five years until it was experimentally verified. The first experimental observations were reported in 1928 by Raman and Krishnan;[163] they declared the discovery of a new type of light scattering which was observed via a beam of sunlight passed through a telescope objective into a scattering material (either a liquid or dust-free vapor), the presence of modified scattered radiation was then detected by the observers eyes via a filter. Further publications provide a more comprehensive insight into the experimental techniques with sunlight being replaced by a mercury arc lamp [164, 165]. However, it would not be until the 1960s that

Raman Spectroscopy became a more conventional tool in chemical analysis, owing to the advent of commercially available lasers – which provide an extremely monochromatic, narrow beam and high intensity light source ideal for Raman spectroscopy.

Now, Raman spectroscopy is one of the most used forms of vibrational spectroscopy – along with mid-infrared (IR) and near-IR – and provides a method of determining and identifying molecular structure through fundamental molecular vibrations. It is a versatile technique as it is possible to investigate a wide range of sample types: liquid, gas or solid in either bulk or microscopic quantities.[166] Furthermore, it is a non-destructive and non-invasive technique. Following acquisition, analysis can range from simple identification to more in-depth qualitative and quantitative analysis, as the technique is information rich, including chemical identification and characterization of molecular structures.[166]

During a typical Raman experiment the sample is exposed to monochromatic light from a laser source. This causes the light to either reflect, absorb or scatter. Of these, the inelastically scattered light is analysed during Raman spectroscopy, which reveals information about the molecular structure. Figure 7.1 is a schematic of the optical path within the LabRAM HR Evolution spectrometer (Horiba-Jobin-Yvon) used throughout these experiments. The laser (either an internal, E1 or external laser, E2) is directed by two mirrors M1 and M2 though a polarizer, P1, and laser intensity absorption filter, F3. The filter is used to moderate the laser intensity and had nine possible positions: 100%, 50%, 25%, 10%, 5%, 3%, 1%, 0.1% and 0.001%. The laser beam was then focused on the pinhole, H1 via a lens, L1. Next the resulting laser image was focused by the lens, L3, via the mirror, M7 on the notch filter, F4. The angle must be correct in order for the laser beam to be completely reflected towards the sample. The L2 lens produced a parallel beam that was focused on the sample by the microscope objective.

The Raman scattered light collected by the microscope objective is passed back through the L2 lens to the spectrograph. Figure 7.2 shows the optic path within the spectrograph with the scattered light terminating at the CCD detector.

In Raman spectroscopy, the molecules are excited to a ‘virtual state’ and

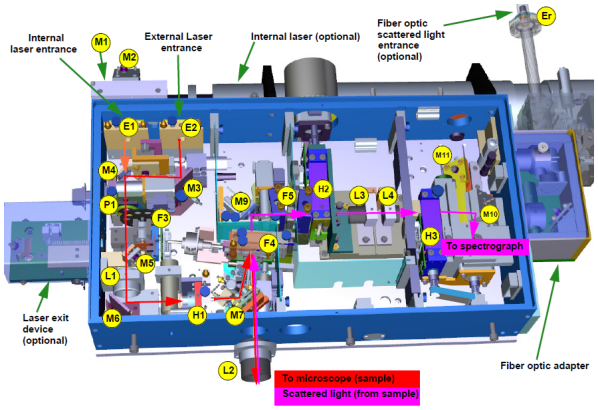


Figure 7.1.: Optical path for visible light in LabRAM HR Evolution Raman spectrometer. The red line is route the laser light travels to the sample. Whilst the pink line is the route the scattered light travels from the sample to the CCD detector. HORIBA Scientific.

then allowed to relax. The changes caused by this scattering process are commonly quantified by:

$$\Delta w = \left(\frac{1}{\lambda_0} + \frac{1}{\lambda_1} \right), \tag{7.1}$$

where Δw is the Raman shift in wave frequency (cm^{-1}), λ_0 and λ_1 are the incident and Raman radiation wavelengths respectively. From this, the energy difference between the initial and Raman scattered light may be

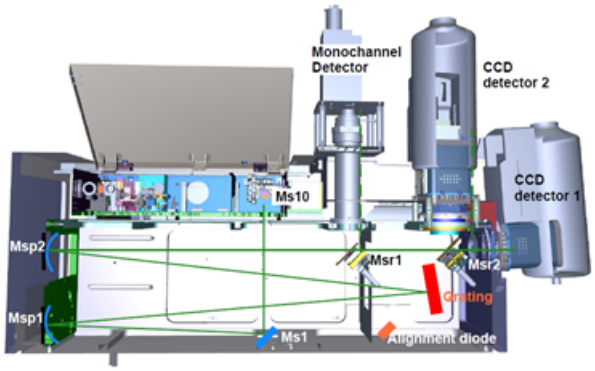


Figure 7.2.: Spectrograph optic path for LabRam HR Evolution Raman spectrometer. HORIBA Scientific.

calculated. Three types of scattered light may be defined, as seen in Figure 7.3:

1. **Rayleigh (elastic) scattering** occurs when an excited electron returns to its original ground state. In this case there is no change in energy and no Raman shift. This accounts for the majority of scattered light, approximately 10^{-3} of the incident beam. Rayleigh scattering is the reason the sky exhibits colours.

2. **Stokes Raman (inelastic) scattering** occurs when an excited electron returns to a higher energy state than originally, leading to a decrease in the scattered light energy and therefore a positive Raman shift. The Stokes Raman response is normally considered as the Raman signal.

3. **anti-Stokes Raman (inelastic) scattering** occurs when an electron is excited from an originally excited energy level but returns to the ground state. This leads to a relative increase in the recorded spectral energy and therefore a negative Raman shift. As anti-Stokes requires the electrons to exist in an excited state before scattering its magnitude is usually significantly less than the Stokes scattering component unless considerable sample heating has occurred. Therefore, monitoring of the anti-Stokes scattering magnitude can be used to ensure that the Raman spectroscopy is not affecting the sample's electronic properties.

Raman scattering (Stokes and anti-Stokes) is much less probable than Rayleigh scattering and only accounts for roughly 10^{-6} of the incident beam. In order to be Raman active, the vibration must cause a change in the polarisability (α) in the molecule with respect to displacement dx, in other words $(d\alpha/dx) \neq 0$ and therefore not all vibrations are Raman active. For a vibration to be IR active, the dipole moment (ϖ) must change with respect to displacement from equilibrium distance: dx, in other words $(d\varpi/dx) \neq 0$. In general, the symmetry – or lack of – of a molecule determines whether vibrations are Raman and IR active. Using the symmetry of a molecule allows the relationship between the molecular structure and the vibrational spectrum to be understood. As a rule of thumb symmetric/in-phase/non-polar group vibrations are Raman active, and asymmetric/out-

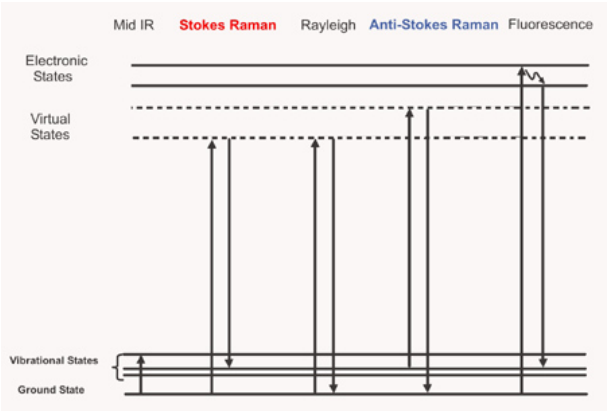


Figure 7.3.: Possible Raman frequencies. Of interest is inelastic scattered light - Stokes Raman and Anti-Stokes Raman. HORIBA Scientific [11].

of-phase/polar group vibrations are IR active. For molecules with a centre of symmetry then vibrations cannot be active in both Raman and IR spectra, known as the Principle of mutual exclusion. If a molecule has different elements of symmetry then certain bands may be active in Raman, IR, both or neither. Furthermore, for more complex molecules which have no centre of symmetry, vibrations can be active in both Raman and IR. However, it is possible that vibrations are not observed even if theoretically possible if they are intrinsically too weak or obscured by stronger neighbouring bonds.

The molecular motion contains internal vibrational degrees of freedom. These are $3n-6$ and $3n-5$, for linear and non-linear molecules, respectively [167] where n is the number of atoms in a molecule, reduced by 3 translational + 3 rotational degrees of freedom for non-linear molecules, and 3 translational + 2 rotational degrees of freedom for linear molecules. For two examples, the number of vibrational modes is given by:

$$H_2O : 3(3) - 6 = 3 \tag{7.2}$$

$$CO_2 : 3(3) - 5 = 4 \tag{7.3}$$

We present here preliminary work on the novel use of Raman spectroscopy

for multi-phase flow characterization in micro-models using systems relevant to EOR applications. This utilizes many of Raman spectroscopic benefits: small sample volumes, non-destructive and non-invasive and ability to characterise phases and compositions therein based on the spectral shift, intensity and band shape without the need for sampling or additive compounds.

7.2. Experimental Set-up

Fluids Investigated. For chemical EOR floods it has been found that anionic surfactants give the best performance/cost profile in sandstone reservoirs.[168] Anionic surfactants can have different hydrophilic groups: carboxylates, sulphates, sulphonates and phosphates.[81] In this work, a previously demonstrated surfactant system comprising of a sulphonate head group and hydrocarbon tail capable of stable micro-emulsion formation is used. It has been shown experimentally that the use of branched surfactants, including twin-tailed internal olefin sulphonates (IOS), are desirable for surfactant EOR.[12, 168, 169] Benefits of using IOS include: the formation of micro-emulsion phase, minimising ordering the oil/water interface and prevention of the formation of more viscous macro-emulsion phases [12]. This is beneficial for EOR processes as ordered structures may potentially block the porous medium reducing the recovery rate. Furthermore, the formation of ordered structures would lead to surfactant retention resulting in decreased sweep efficiency. These factors could result in the project not being economically feasible.

The main surfactant species investigated are twin-tailed isomers of alkene sulphonates and a range of twin-tailed isomers of hydroxyalkane sulphonates, the chemical structure of each is illustrated in Figure 7.4.

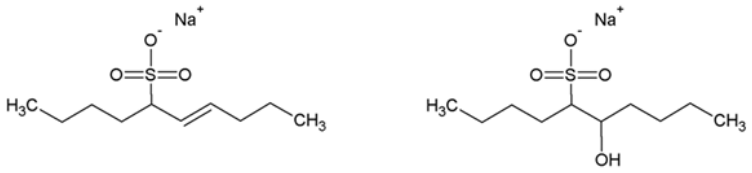


Figure 7.4.: Chemical structure of Internal olefin sulphonates investigated Left: Alkene sulphonate Right: Hydroxy alkane sulphonate.

In this study, different surfactant concentrations were investigated: 1, 2, 3, 4, 5 wt%. Analogue hydrocarbons were used in place of crude oil. This was done to avoid micro-model contamination. The analogue oils selected were *n*-decane (Sigma-Aldrich, 99%) and deuterated decane (*d*-decane) (Magni-Solv, 99%). The substitution of hydrogen atoms by deuterium in decane, was used for distinguishing oil from the surfactant species in the Raman spectra; see Figure 7.5 for the chemical structure.

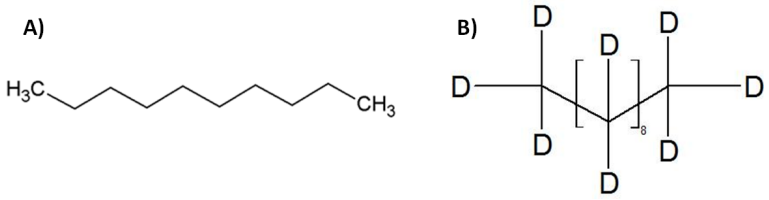


Figure 7.5.: Chemical structure of A) *n*-decane and B) *d*-decane, where the hydrogen molecules have been replaced with deuterium.

Experimental Equipment. An integrated Raman confocal system was used to investigate phase identification within micro-models. All of these experiments have been conducted in glass micro-models (Micronit Microfluidics). The micro-model design consisted of a homogeneous array of circular pore bodies (width – 60μm) with a coordination number of 6. The width of the throats was 13 μm with a 20 μm distance between pore bodies, shown in Figure 7.6.

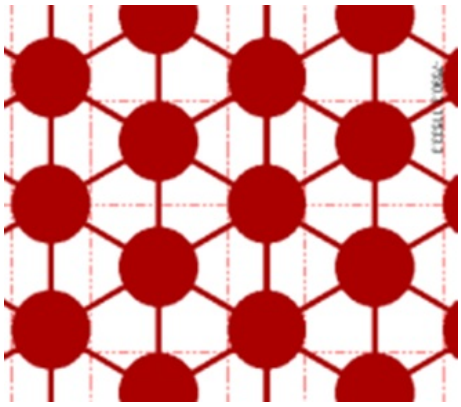


Figure 7.6.: Schematic of homogeneous micro-model matrix pattern used in this study. Pattern consisted of pore bodies with a width – 60μm, throat width – 13μm, etch depth – 5μm and a coordination number of 6 (personal communication).

All experiments were conducted at ambient temperature and pressure conditions. A general methodology for the Raman experiments is given below. This includes preparation of the micro-models, fluid injection, spectral acquisition and processing.

Fluid Injection. Initially, the micro-model is fixed into a special holder to allow secure, leak-tight connections to syringes via tubing. The holder also prevents the model moving during experiments. Furthermore, the holder is mounted on a motorised stage which allows accurate positioning of the model under the microscope objective directing the laser beam on the sample.

In these experiments, two ports were used to inject the fluid whilst the other two act as outlets to ambient conditions. Injection is achieved via 100 μl syringes (1810 RN SYR, Hamilton) operating at a controlled flow rate achieved by a programmable syringe pump (PicoPlus Elite Pump II, Harvard Apparatus). The configuration used is able to support low flow rates over the range from 115 pl/min to 120 μl/min, as required for microfluidic work.

During two-phase experiments, the model was initially filled with the oil phase. Once completely saturated with oil, the tubing connections were removed at the model. The syringes were then filled with the second phase and the lines filled before re-connecting to the model. During re-connection the pumps were injecting at a very low flow rate to avoid air entering the model.

Furthermore, to ensure that the micro-emulsion phase form within the model, the connections were opened at the model rather than further upstream at the syringe. This is particularly important in the case of optimum surfactant concentration, micro-emulsion formation was observed within the tubing before reaching the model when the tubing was reconnected at the syringe.

Visualisation. The system used was an integrated confocal Raman system (LabRAM HR Evolution Raman Spectrometer, Horiba-Jobin-Yvon) resulting in spatial resolutions comparable to a standard confocal microscope. Therefore, submicron lateral resolution and axial performance better than 2 μm is possible. To aid in visualisation of the micro-models the system was

equipped with a white light illumination source (LE.5210, Euromex). The micro-model was illuminated via transmitted light which passes through the selected objective, allowing accurate positioning of the micro-model before scanning begins. In addition there is a camera which allows images to be captured before and after spectral acquisition to observe fluid rearrangement during scanning.

There were four possible objectives to choose from: 10×, 50×, 50× LWD (long working distance) and 100×. Higher magnification, leads to better the resolution and improved focusing of the laser source. Therefore, the 50xLWD was used throughout this study as it provided the best balance between magnification and field of view. Furthermore, the size of the confocal pinhole was adjustable from several μm to 1200 μm, and was set using the software (LabSpec 6). The size of the pinhole defines the size of the volume to be analysed within the micro-model. Thus, the smaller the pinhole the smaller the volume analysed and therefore more accurate spectra are acquired. However, smaller pinhole sizes result in a much faster Raman signal drop when not in focus.

The size of the pinhole is also an important factor when planning maps of the region of interest. A map is created by acquiring spectra at predefined points positioned over a region of interest. Figure 7.7 displays a square grid over a single pore for mapping. The shape of the grid is defined by the user. Several mapping options were available: rectangle, circle, polygon, line and points maps depending on the purpose of the map. The size of the pinhole is important, especially when the distances between the points are close together. Therefore, the closer the grid spacing the smaller the pinhole should be resulting in smaller volumes analysed. Maps could be programmed to record spectra in x, y, and z directions. Furthermore, maps could be set to record repeated data sets for the same grid spaced at user defined time intervals.

When the area of interest was larger than the field of view it was possible to stitch multiple microscope images together to create a larger image. The size of the image was programmed through the software and immediately displayed once acquired. Once the image was captured it was possible to create a map over the area of interest.

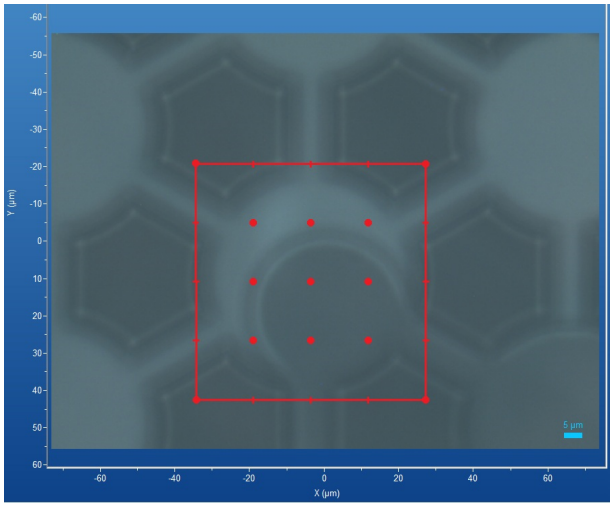


Figure 7.7.: Example of a square grid used for mapping purposes.

Spectra acquisition. To ensure power stability, the laser was allowed to heat up for 30 minutes before any measurement. The micro-model was then positioned appropriately in the z-direction to ensure that the best focus was achieved. For reproducible experimental measurements, the spectra were taken with the most highly focused laser spot to ensure maximum intensity. Once the micro-model was in position, spectra could be acquired. There are multiple parameters which can be tuned to achieve better results. Parameters include: laser wavelength, objective, spectral range, acquisition time, number of accumulations and the size of the pin hole. The majority of these are controlled through the specialist software: LabSpec6 (Horiba Scientific).

In this study the spectrometer was equipped with two lasers: green laser (λ_{em} - 532nm) and a NIR laser (λ_{em} – 785nm). All results presented were taken using the green laser. The acquired spectral range from 400 to 4000 cm^{-1}, was maintained throughout these preliminary experiments. This provides an overview of the Raman response allowing the entire range of peak locations to be identified. No significance change time dependence of the Raman spectra was observed, suggesting that sample heating was not an issue.

General settings for all experiments conducted include 532 nm laser, 50x LWD objective, typically 400 - 4000 cm^{-1}, 30 s acquisition time, 2 accumu-

lations, either 50 μm or 200 μm pinhole size and 1800 g/mm grating.

Cleaning/Drying micro-models. In order to re-use the micro-models, they were cleaned and dried prior to each experiment. If only DI water had been injected into the micro-model then the model went directly into the vacuum oven (VTR 5060, Heraeus) for drying at 100°C for a minimum of 10 minutes. If other compounds were injected, then the models were first flushed with isopropanol followed by water before being dried in the oven. This step was needed as otherwise the compounds could potentially alter the wettability of the micro-model and influence composition and fluid distribution.

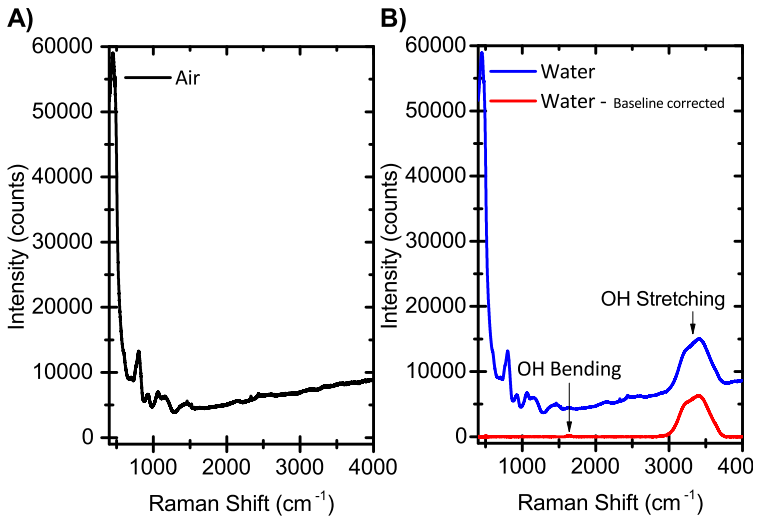


Figure 7.8.: A) Raman spectra for an empty micro-model used as the reference spectra B) Raman spectrum of water before (blue line) and after (red line) baseline correction.

Processing Spectra. To allow the spectra of the oil and surfactant phases to be determined and quantified it is necessary to baseline correct the measured spectra. Throughout this work we subtracted the spectrum of the empty micro-model from all sample measurements to account for the spectral effects caused by the glass. This process is outlined in Figure 7.8, using a micro-model filled with water as an example. Initially, the Raman response of an empty micro-model was measured, as the reference signal for all other spectra (black line in Figure 7.8 A. The peaks observed can be linked to the Si-O-Si vibrational spectrum with a strong Raman shift

in the 450 - 550 cm^{-1} domain.[11] The effects of baseline correction can be seen in Figure 7.8 B. This process illustrates that the main peak of the water spectrum is the OH stretching band at ca. 3200 cm^{-1}, which is demonstrated clearly in the baseline corrected spectra, Figure 7.8 B. The other peak related to water is the OH bending band at ca. 1600 cm^{-1}, however, this is much less prominent.

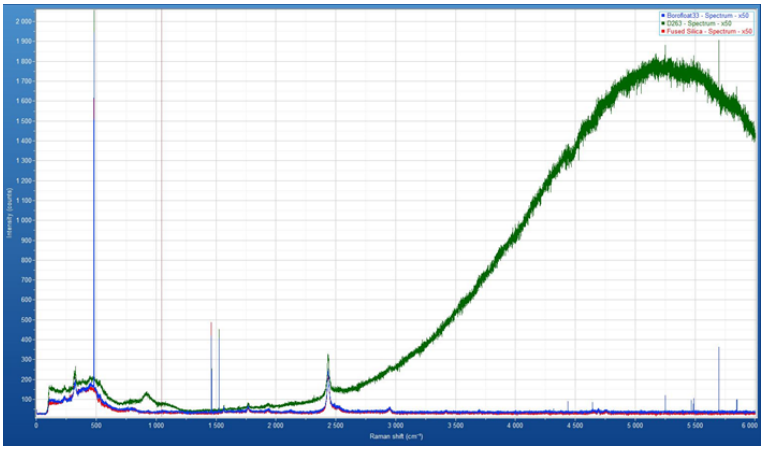


Figure 7.9.: Spectra of other possible materials to fabricate micro-models – Borofloat 33, D 263 glass and fused Silica. All have a response ca. 450 – 500 cm^{-1} due to the Si-O-Si bonds present.

Other types of glass have been considered for fabricating the micro-models. The spectra for Borofloat 33, D263 glass and fused silica are shown in Figure 7.9. As can be seen all produce peaks ca. 450 – 550 cm^{-1} due to the Si-O-Si bonds within the glass. Additionally, the fused silica spectrum shows a large amount of fluorescence from ca. 2500 cm^{-1} to 6000 cm^{-1}, therefore, silica micro-models are not ideal for Raman spectroscopy experiments.

7.3. Results and Discussion

Raman spectroscopy seemingly offers the ideal experimental technique to evaluate the effects of surfactants on fluid-fluid displacements in micro-models. However, much work is necessary to understand the applicability of the technique. This work will begin to answer the fundamental experimental problems. For Raman spectroscopy to have any potential use it is

necessary to illustrate that the surfactant and oil phases can be accurately determined. In Section 7.3.1, we will introduce our work on this aspect as well as preliminary experiments on the varying surfactant concentrations. Secondly, the generation and identification of micro-emulsions in microfluidics is an extremely important capability. Therefore, in Section 7.3.2 we will consider whether Raman spectroscopy can be utilised to understand the manifestation of these micro-emulsions. All results presented in Section 7.3 have been baseline corrected as described above.

7.3.1. Calibration of Single Surfactant Phases

Initial experiments were conducted to investigate pure single phases within a micro-model. These allow us to identify the characteristic peaks of these phases which can then be applied to the multi-phase experiments. Furthermore, we consider a range of surfactant concentrations - 1-5 wt% - to assess the capability and sensitivity of the Raman unit in determining these varying surfactant concentrations.

In Figure 7.10 A) the difference between the water and 5% surfactant spectra can be clearly observed. In both spectra the OH stretching and bending peaks (ca. 3200 cm^{-1} and 1600 cm^{-1}, respectively) are present. The additional peaks present in the 5% surfactant spectrum are contributions from the sulphonate head group and hydrocarbon tail. The sulphonate head group bonds detected are SO_3 (ca. 980 cm^{-1}) and S=O (ca. 1044 cm^{-1}), however, both have very low intensity counts. Furthermore, the peaks from the sulphonate head group are concealed by the fluorescence of the glass. The more prominent peaks, mainly in the 2800-300 cm^{-1} domain, relate to the hydrocarbon backbone of the surfactant. Table 7.1 lists the different CH_2 and CH_3 peaks corresponding to the hydrocarbon chain.

It is important to note that the recorded surfactant spectra are influenced by the surfactant concentration: this can be seen in both the whole range spectra and the sulphonate signatures as shown in Figures 7.10 B and C, respectively. As shown in Figure 7.10 B, the surfactant concentration seemingly suppresses the 3200 cm^{-1} water signature, therefore, the water peak at ca. 1600 cm^{-1} was used. Furthermore, the peaks ca. 2800 cm^{-1} corresponding to the hydrocarbon chain increased with increasing concentration.

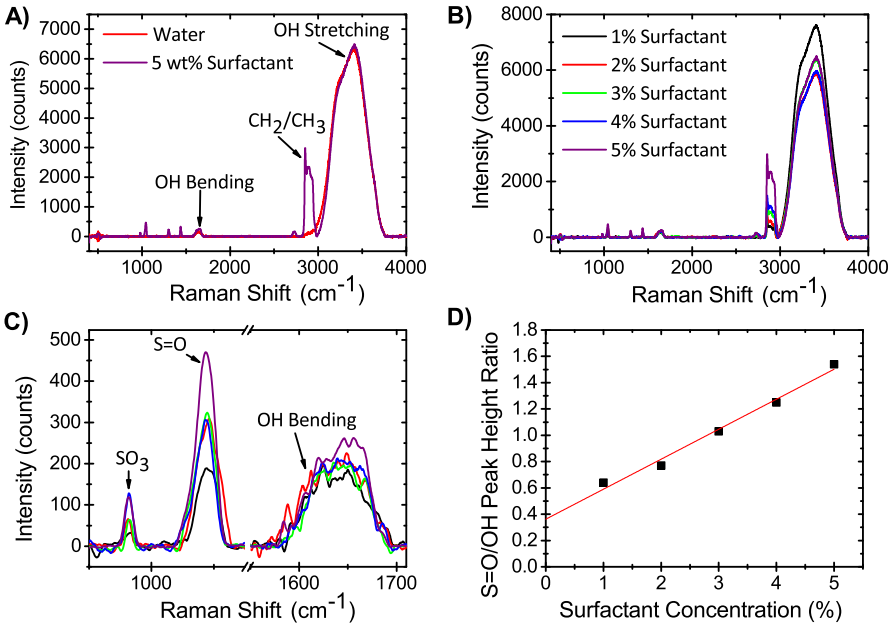


Figure 7.10.: A) Water (red) and 5 wt% surfactant (purple) spectra illustrating the difference between the two especially at ca. 2800 cm^{-1} B) Spectra for 1 – 5 wt% surfactant solutions, C) S03 and S=O peaks relating to the sulphonate head group and the OH bending peak ca. 1600 cm^{-1}. D) Peak height ratio for S=O/OH bending peak.

In Figure 7.10 C, the sulphonate head peak and OH bending region is illustrated. The peak ca. 980 cm^{-1} corresponds to SO_3, whilst the peak ca. 1044 cm^{-1} is S=O and ca. 1600 cm^{-1} is the OH bending region. In comparison to the 3200 cm^{-1} H_2O, the intensity of these peaks is very low. It can be seen that the Raman response increases with the concentration of surfactant. This is most clearly seen by the S=O/OH peak height ratio (using the OH bending mode (1600 cm^{-1})). As shown in Figure 7.10 D, there is a linear correlation between the surfactant concentration and relative intensity of the sulphonate peak.

To begin testing the behaviour of micro-emulsions, an optimum micro-emulsion was injected into the micro-model. This micro-emulsion was formed during a phase behaviour test. During a phase behaviour test surfactant/oil/water mixtures are investigated. Initially a set amount of surfactant solution was placed into a borosilicate glass pipette. Next the same

Table 7.1.: Raman shift locations of CH_2 and CH_3 corresponding to the hydrocarbon chain

Raman Shift (cm^{-1})	Bond Type
1300	$(CH_2)_n$ Twist
1440	CH_2 Bend deformation
2853	CH_2 In-phase stretching
2875	CH_3 In-phase stretching
2898	CH_2 Fermi resonance
2937	CH_2 Out-phase stretching
2963	CH_3 Out-phase stretching

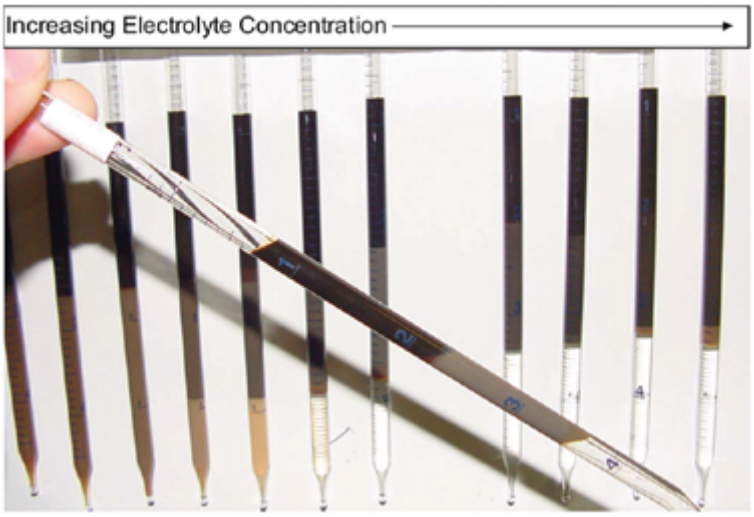


Figure 7.11.: Phase behaviour test conducted within a pipette. The middle phase is a Winsor III micro-emulsion. [12]

amount of the oil phase was added to the pipette and placed within an oven to achieve reservoir conditions. Once conditions are achieved the pipettes were removed from the oven and contents are mixed by repeatedly inverting the pipettes for several minutes. Phase volumes can then be observed along with the formation of a third micro-emulsion phase if conditions are correct. Figure 7.11 shows a micro-emulsion which had formed during a phase behaviour test. To acquire the micro-emulsion spectra a small amount of micro-emulsion was removed from a phase behaviour test and injected into the micro-model. The solutions used in the phase behaviour test were: *n*-decane and 2% surfactant + 2.2% NaCl.

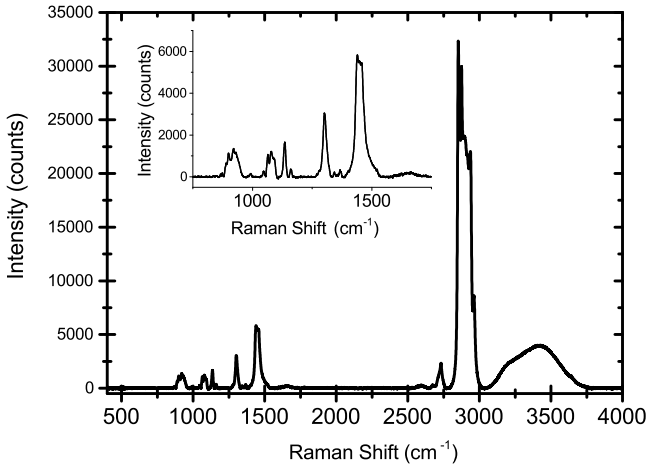


Figure 7.12.: Spectrum for an optimum micro-emulsion created from 2% Surfactant + 2.2% NaCl during a phase behavior test, where oil phase was *n*-decane. Both the water peak and CH_2/CH_3 peaks can be seen, however, cannot distinguish how much of the CH_2/CH_3 peak is from the surfactant and *n*-decane, In addition the surfactant head peaks are difficult to identify (inset)

In Figure 7.12 the spectra obtained from this optimum micro-emulsion is displayed. As can be seen the OH, CH_2/CH_3 peaks can be observed; however, the peaks relating in the sulphonate head group are obscured. The inset for Figure 7.12 focusses on the sulphonate head group region, the S=O peak ca. 1000 cm^{-1} can be observed but, as expected, is diminished in magnitude.

Therefore, it is clear that Raman Spectroscopy can ascertain the individual phases and their relative concentrations. In the later sections, we will apply this knowledge for more complex experiments.

7.3.2. Micro-emulsion and Multiple Phases in Micro-models

Having established the validity of Raman spectroscopy, experiments were carried out in which two phases were injected into the micro-model to replicate EOR injection processes. To this end, we considered the 5% surfactant

solution and n-decane, which is a crude oil analogue. Initially, the model was completely filled with 5% surfactant before n-decane was injected at a flow rate of 200 pl/min. The slow flow rate was selected so that it was possible to visualise the oil phase entering the model aiming at stopping flow when approximately half the model was filled with n-decane. This volume of n-decane was selected to ensure that the model did not entirely fill with n-decane. In Figure 7.13 A, two phases can be clearly seen in a pore body of the micro-model.

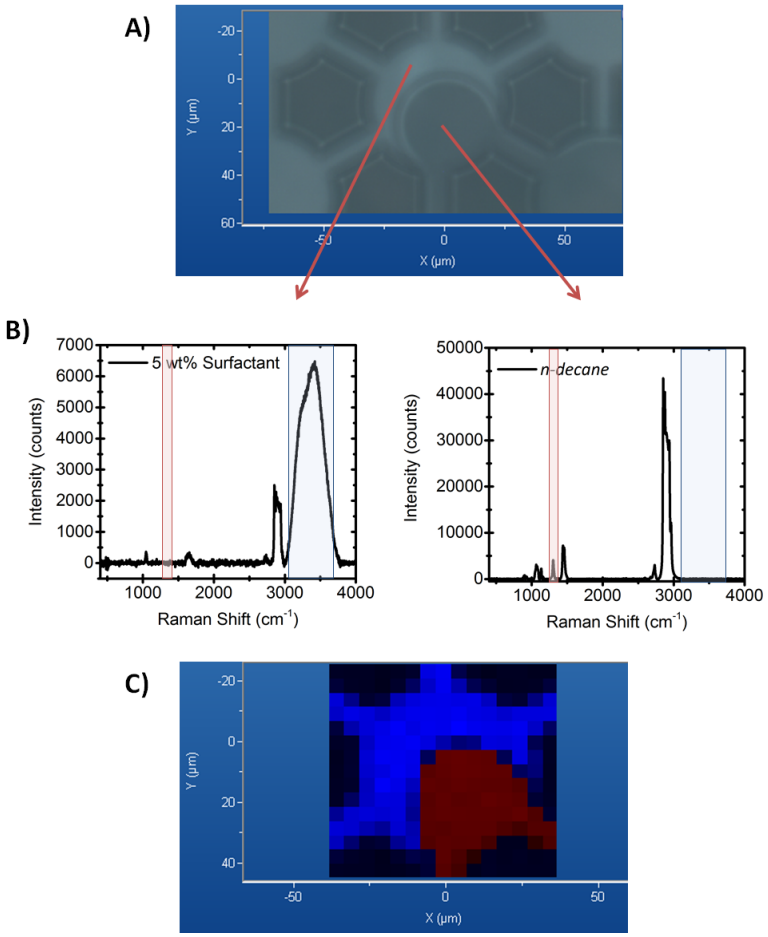


Figure 7.13.: A) Optical image of a pore body within the micro-model in which two phases are present B) Spectra acquired for the different phases within the pore body, Acq. Time 5 s, Accumulations 2, Range 400-4000 cm-1, 50× LWD objective, 1800 gr/mm grating and 200 hole size. C) Intensity map relating to the peaks highlighted in the spectra

A detailed map of measured points was collected over one entire pore to establish the ability of Raman to distinguish the different phases present. Figure 7.13 B, presents a spectrum for each of the phases present within the pore body. At these short but practical acquisition times (5 s) the peaks relating to the sulphonate head group were not detected within the 5% surfactant spectrum. Therefore, the OH stretching peak – highlighted in blue – was chosen to represent the surfactant phase since it is not present in the *n*-decane phase. As both the surfactant and *n*-decane phases contain a hydrocarbon chain, the CH_2/CH_3 peaks ca. 2800 cm^{-1} were not used. Instead the peak ca. 1300 cm^{-1} corresponding to the CH_2 twist was selected, highlighted in red in Figure 7.13 B. Figure 7.13 C, is an intensity map of the pore illustrating that Raman is able to accurately separate the two phases. In this particular experiment, a micro-emulsion would not form between the surfactant and the *n*-decane. This was because the 5% surfactant was too unstable and optimum conditions were not achieved. Furthermore, in field applications 5% surfactant would not be used due to the high costs associated with producing the surfactants.

However, when performing experiments in which a micro-emulsion could form in-situ, determining the contributions from the surfactant and oil phases is difficult. Unfortunately, at short acquisition time the sulphonate peaks are difficult to detect, therefore, another peak needs to be selected for analysis. When looking at the chemical structure of both *n*-decane and the surfactant, it is obvious that the main component of both is a hydrocarbon chain. Therefore, to distinguish between them a slight change is needed in the chemical structure of one phase. Since the surfactant structure must remain the same, another analogue oil was selected, *d*-decane. *d*-decane was selected as it has similar properties to *n*-decane; however, the hydrogen molecules have been replaced with deuterium.

Figure 7.14 illustrates the difference between *n*-decane and *d*-decane spectrum. As the *d*-decane solution was only 99% pure there were still some CH bonds remaining. However, as can be seen from Figure 7.14 a significantly smaller CH_2/CH_3 peaks at ca. 2900 cm^{-1} are present in the *d*-decane spectrum compared to the *n*-decane spectrum. Therefore, the pure *d*-decane spectrum was used as a reference to compare potential micro-emulsions and estimate the concentration of surfactant through the difference in peak in-

tensity between *d*-decane and micro-emulsion.

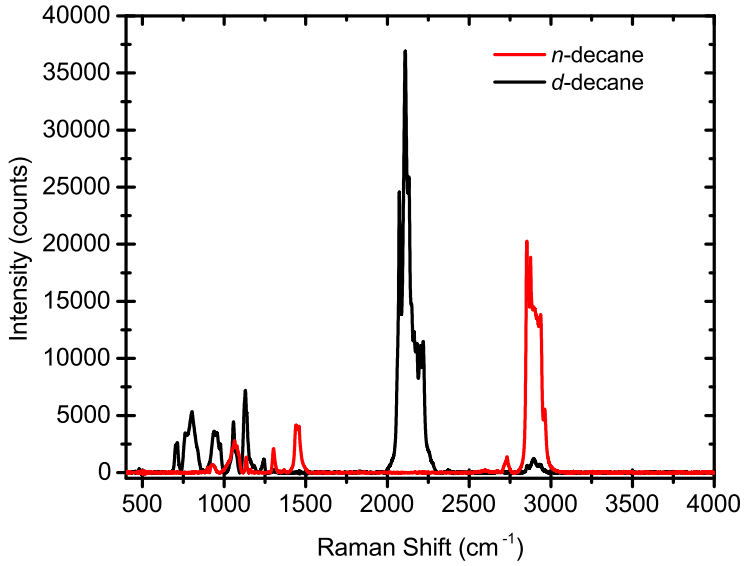


Figure 7.14.: Spectra for both *n*-decane and *d*-decane, illustrating the shift in peak locations due to the change in bonds from hydrogen to deuterium. Some CH_2/CH_3 peaks are still present in the *d*-decane due to its 99% purity.

Next, experiments were conducted to create a micro-emulsion within the micro-model. To achieve this, the same surfactant solution was used as in the above phase behaviour test: 2% surfactant + 2.2% NaCl. During the experiment the micro-model was initially saturated with *d*-decane before the surfactant solution was injected at 200 pl/min. The slow flow rates were selected to allow visualisation of micro-emulsion formation and acquiring spectra to check. Figure 7.15 A, is the spectra of a micro-emulsion formed in-situ within the micro-model. It can be determined as a micro-emulsion as the three necessary phases are present: water/oil/surfactant.

From the spectra all three phases which should be in a micro-emulsion can be identified: water (OH peaks at ca 1600 and 3200 cm^{-1}), oil (ca. 2100 cm^{-1}) and surfactant (ca. 2800 cm^{-1}). Both the *d*-decane and micro-emulsion spectra are presented in Figure 7.15 B. Figure 7.15 C, clearly shows that there is a difference in intensity between the surfactant and *d*-decane peaks. This difference can be attributed to the hydrocarbon backbone of the surfactant.

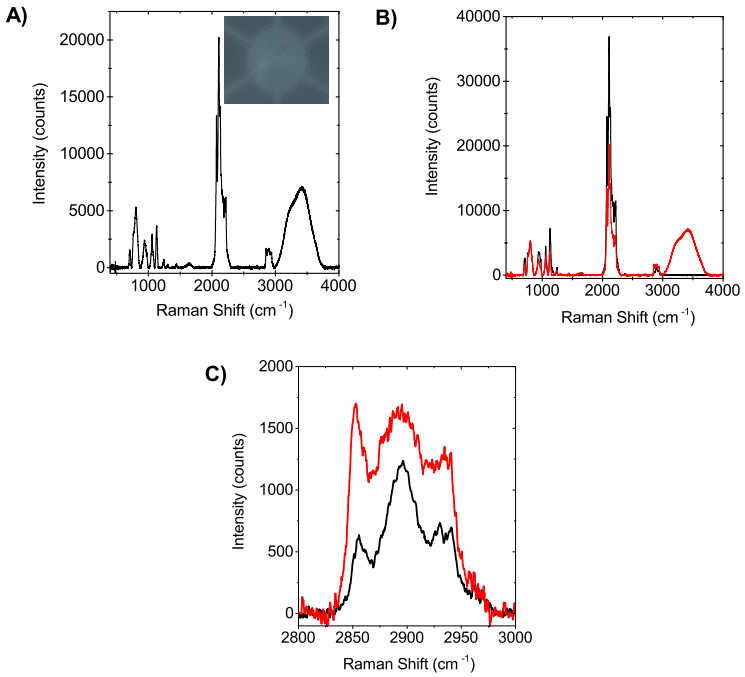


Figure 7.15.: A) Micro-emulsion spectra including, with the insert of the micro-emulsion within the micro-model. B) Spectra illustrating the difference between the micro-emulsion and the *d*-decane. Three phases can be clearly identified: water, surfactant and *d*-decane. C) illustrates the difference between the CH_2/CH_3 peaks in B.

7.4. Conclusions

Preliminary experiments were conducted to record spectra for individual phases within a glass micro-model. These included surfactants of varying concentration ($1 - 5$ wt%) and analogue oils - *n*-decane and *d*-decane. The spectrum for an empty micro-model was used as the reference signal with all other spectra corrected based on this signal. This was done to remove the observed fluorescence from the glass. All experiments were conducted at ambient conditions. The following findings were observed:

1. The spectra for the different surfactant concentrations show that with increasing concentration the water peak is suppressed whilst the peaks ca. 200 cm^{-1} relating to the hydrocarbon backbone are amplified.

Therefore, based on these preliminary results the use of Raman spectroscopy for phase identification and relative concentrations is achievable;

2. More complex systems were then investigated in which two phases – *n*-decane and surfactant – were injected into the micro-model. The experiment in which 5 wt% surfactant and *n*-decane were both present within the micro-model illustrated that Raman spectroscopy is capable of identifying both phases;

3. At realistic acquisition times, the signature surfactant peaks (sulphonates) are difficult to detect. Furthermore, due to the similar nature of the chemical structure of both the surfactant and *n*-decane the hydrocarbon chain peaks cannot be used to differentiate the two phases. Therefore, *d*-decane must be used as the analogue oil phase;

4. The injection of 2% surfactant + 2.2% NaCl and *d*-decane resulted in the formation of a micro-emulsion within the micro-model. Spectra were recorded which clearly indicated the formation of a micro-emulsion as water, oil, and surfactant peaks were all present.

Future work includes optimising the system to allow dynamic processes to be recorded. Now that the main peaks of interest have been identified, spectral acquisition time could be decreased. Furthermore, more focused spectral acquisitions could be acquired instead of the entire 400 – 4000 cm^{-1} spectral range further deceasing the acquisition time.

Phase behaviour tests could be conducted using *d*-decane as the oil phase and 2% surfactant + 2.2% NaCl to establish whether over-, under- or optimum micro-emulsion was formed in-situ in the micro-models. Once the optimum surfactant solution has been determined, more extensive, systematic micro-model experiments can be conducted. The nature of these experiments will depend on the area of interest with regards to EOR applications. Some areas of interest could be investigating whether there is a change in surfactant concentration gradient along the length of the micro-model. Additionally, how the surfactant/micro-emulsion front moves through the micro-model, especially with improved acquisition parameters. This could be linked to the entire flooding process and focus on the changes in compo-

sition of one trapped oil ganglia during surfactant flooding.

8. Conclusions and Future Work

This thesis presents a suite of micro-fluidic experiments, investigating fundamental multiphase flow at the pore scale. Throughout, fluid flow in specifically designed micro-models has been imaged using both optical and Raman microscopy. The micro-model designs ranged from simple capillaries to networks more representative of porous media. Most experiments were conducted at ambient temperatures and pressures. High pressure experiments were carried out to ensure that the glass micro-models can be used up to a pressure of 100 bar for future CO_2 applications. The conclusions and recommendations for future work are presented in Sections 8.1 and 8.2 respectively.

8.1. Conclusions

The simplest geometries investigated were single capillaries, used to measure the dynamics of imbibition. The Lucas-Washburn equation predicts that the distance a meniscus travels within a smooth cylindrical capillary is proportional to the square root of time, provided that the viscosity contrast between the displacing and displaced fluid is sufficiently high. Initial experiments were conducted in **Smooth Capillaries** with a rectangular cross-section. Reproducible results in both the small (500×50 μm) and large (4000×400 μm) smooth rectangular glass capillaries were observed. The results show that the capillary filling was quicker for the wider capillary, which is expected from the Lucas-Washburn equation. However, the visco-inertial regime ($l \sim t$) was observed in all experiments as the limited field of view of the capillary prohibited the Lucas-Washburn regime from being observed: the slope of the results at later times when plotted on a log scale was found to be 0.6 and 0.7 for the small and large capillaries, respectively.

As the Lucas-Washburn regime was not reached, further quantitative analysis could not be conducted. In real rocks there are few, if any, long straight channels and meniscus dynamics are therefore likely to remain in the inertial or visco-inertial regimes. Furthermore, smooth single capillaries are not representative of porous media. Therefore, capillaries were investigated in which the surface **roughness** of the capillaries had been systematically increased.

In the **Rough Capillaries** it was found that, with time, the wettability of the capillaries slowly changed from water-wet to oil-wet, due to chemical degradation of the initial water-wet surface coating. Initial water-wet experiments found that the advancing DI water meniscus became pinned within the roughest capillary (Cap_50_4). However, while continuing the investigation of this phenomenon, the capillary became non-water wet. Therefore, later experiments were conducted with hexadecane as the wetting phase (WP) which continued to imbibe. It is clear that the surface chemistry of the capillaries changes progressively with time. In the hexadecane experiments, a systematic decrease in the rate of imbibition with increasing roughness was observed as predicted in nano-capillaries by Stukan *et al.*[103]. However, this change did not show a linear trend as predicted but was quartic in nature. However, in the light of the observed changes in wettability, it cannot be ascertained whether the increase in roughness and/or capillary wettability are driving these observations. Therefore, a separate methodology for experimentally deriving the actual contact angle is required.

Next, **Single Junctions** were considered which were comprised of a single pore body surrounded by throats of varying widths. The widths were chosen to create a range of different capillary entry pressures. It is commonly assumed in Pore Network Models (PNMs) that the sequence of filling for multiple throats connected to a pore is determined by the Young-Laplace equation. This was validated for **Drainage** experiments in which the non-wetting phase (NWP) saturation was continuously increased. In the case of **Imbibition** the quasi-static experimental results were in line with the theoretical predictions of the Young-Laplace equation. However, when spontaneous imbibition experiments were conducted, the fluid displacement pathway selected was different to the predictions. Instead of the narrowest throat filling first, the advancing meniscus travelled down the nearest throat

first. This occurs as, once the critical entry pressure of the pore is exceeded, any downstream throat is able to fill. This could explain why PNMs are unable to accurately predict imbibition processes (private correspondence).

Finally preliminary experiments were conducted to investigate whether **Raman spectroscopy** can be utilised in distinguishing individual phases within micro-models for surfactant enjanced oil recovery (EOR) processes. Initially, individual surfactants of varying concentration (1 – 5 wt%) and analogue oils - *n*-decane and *d*-decane were investigated to record and understand spectra. It was found that Raman spectroscopy is sensitive to the increasing surfactant concentration. Furthermore, the injection of 2% surfactant + 2.2% NaCl and *d*-decane resulted in the formation of a micro-emulsion within the micro-model. Spectra were recorded which clearly indicated the formation of a micro-emulsion as water, oil, and surfactant peaks were all present. Therefore, based on these preliminary results, the validity of Raman spectroscopy for phase identification and relative concentrations in micro-model EOR studies was shown.

8.2. Recommendations for Future Work

The experimental findings can be separated into three distinct concepts: the applicability of the Lucas-Washburn equation and PNM filling rules derived from the Young-Laplace equation and the potential of Raman spectroscopy for surfactant EOR applications. Future work is recommended in each of these avenues.

8.2.1. Lucas-Washburn Studies

Having potentially established a correlation between capillary roughness and rate of imbibition, further work is necessary to validate the findings. Initially, comprehensive studies to ascertain the equilibrium contact angle for each individual capillary are essential. This could be achieved by using the gravity based technique outlined in Section 5.2. However, in the case of the rough capillaries used in this work, there are a number of difficulties. The main issue arises from the construction of the capillaries in two

different materials – silicon and glass – resulting in two different contact angles within the models. Furthermore, the oxidation treatment of the silicon wafer - to produce two water-wet surfaces - has degraded with time, causing wettability uncertainties. It is recommended to fabricate a new set of rough capillaries of a single material, including a completely smooth capillary. Ideally, this would be glass which is water-wet when untreated. However, at present the capabilities of glass etching techniques do not allow micro-models to be fabricated at the desired scale and resolution. Therefore, the best option in the short term may be to consider treating the type of capillaries used in this thesis to controllably alter the wettability. Furthermore, experiments could be conducted to investigate the dynamic contact angle. This could be achieved by observing a small section of the capillary at high resolution. Again, pure glass micro-models would be beneficial as they allow easy illumination of the capillary and uniform contact angles on all surfaces. Dynamic contact angle measurements would also allow accurate comparisons with Lattice Boltzman Model simulations which predict both the equilibrium and dynamic contact angles.

8.2.2. Young-Laplace Studies

The experiments discussed in Chapter 5 have verified that drainage and quasi-static imbibition are well understood and adequately represented in PNMs. Therefore, future work should focus on spontaneous and forced imbibition. In terms of the single junctions, considering secondary imbibition – where the initially WP saturated model is injected with NWP before the WP is allowed to re-enter the micro-model – is of interest. This would allow confirmation of existing literature and the creation of an experimental methodology which could be applied to the more complex network models. In particular, finding a fluid pair in which one fluid is sufficiently wetting to allow spontaneous imbibition is necessary for the PMMA models considered in this work.

As outlined in Chapter 6, preliminary experiments using a network of varying pores and throats were conducted. Initially, full drainage and imbibition experiments need to be conducted at ambient temperature and pressure via a gravity driven process, which provides accurate control of the

capillary pressure. Once the experimental technique is established, experiments with supercritical CO_2 should be performed. The results of these experiments could be compared to existing PNMs which are able to predict drainage but have problems with imbibition. The preliminary experiments have already indicated some technological challenges. Firstly, the system must achieve equilibrium between each pressure step for the experiments to be comparable to PNMs. However, from current observations, this can take hours, leading to difficulties maintaining the experimental conditions throughout the measurement. Furthermore, the dye currently used demonstrates a clear fading with time such that by the end of the experiment ascertaining the phases is difficult. Therefore, the ideal experimental technique still needs to be established.

8.2.3. Raman Spectroscopy

The work outlined in Chapter 7 has established that Raman spectroscopy is an exceptional technique for distinguishing the separate phases present in micro-models. Raman spectroscopy is information-rich, potentially allowing calculation of not only the presence of different phases but also their concentrations. Therefore, applying Raman spectroscopy to any system where a distribution of concentrations is expected would be potentially interesting. In this thesis, the phases considered were surfactants and analogous oils (n-decane and d-decane), which potentially lead to the creation of micro-emulsions. Unlike conventional optical methods, the micro-emulsion phase could be easily and quickly identified with Raman spectroscopy. Therefore, continuing these experiments and understanding how the micro-emulsion behaves is of interest. Ideally, establishing the optimum micro-emulsion conditions would be beneficial. To do this, phase behaviour tests between d-decane and 2% surfactant and 2.2% NaCl need to be conducted. It would then be possible to examine micro-emulsion and surfactant behaviour at the pore scale across the entire network model.

Beyond continuing these experiments, optimising the system to allow dynamic processes to be captured more easily should have a multitude of applications. In the case of EOR applications, this could include investigating the development of the micro-emulsion phase and the evolution of

the trapped oil phase with time when micro-emulsion is present. Furthermore, this technique could be used in other applications such as carbon sequestration by investigating Ostwald-ripening using supercritical CO_2.

Bibliography

[1] T. F. Stocker, D. Qin, G.-K. Plattner, M. Tignor, S. K. Allen, J. Boschung, A. Nauels, Y. Xia, V. Bex, and P. M. Midgley, "Climate change 2013: The physical science basis," *Intergovernmental Panel on Climate Change, Working Group I Contribution to the IPCC Fifth Assessment Report (AR5)(Cambridge Univ Press, New York)*, 2013.

[2] P. Tans and R. Keeling, "Trends in Atmospheric Carbon Dioxide," 2014. [Online]. Available: http://www.esrl.noaa.gov/gmd/ccgg/trends/

[3] "Carbon Dioxide Gas Storage," 2014. [Online]. Available: http://www.CO2captureproject.org/media/3_CCP_infographic.jpg

[4] J. Bear, *Dynamics of Fluids in Porous Media*. Courier Dover Publications, 2013.

[5] P. H. Valvatne, "Predictive Pore-scale Modelling of Multiphase Flow," Ph.D. dissertation, Imperial College London, 2004.

[6] M. Buijse, K. Tandon, and S. Jain, "Surfactant optimization for EOR using advanced chemical computational methods," *SPE Improved Oil Recovery Symposium*, pp. 1–12, 2012. [Online]. Available: https://www.onepetro.org/conference-paper/SPE-154212-MS

[7] I. Fatt, "The network model of porous media," *AIME Petroleum Transactions*, vol. 207, pp. 144–181, 1956.

[8] R. Lenormand, C. Zarcone, and A. Sarr, "Mechanisms of the displacement of one fluid by another in a network of capillary ducts," *Journal of Fluid Mechanics*, vol. 135, pp. 337–353, Apr. 1983. [Online]. Available: http://journals.cambridge.org/abstract_S0022112083003110

[9] M. Yanuka, F. Dullien, and D. Elrick, "Percolation processes and porous media: I. geometrical and topological model of porous media using a three-dimensional joint pore size distribution," *Journal of colloid and interface science*, vol. 112, no. 1, pp. 24–41, 1986.

[10] VitroCom, "Rectangle - Miniature Hollow Glass Tubing (VitroTubes™)." [Online]. Available: https://www.vitrocom.com/categories/view/69/Miniature-Hollow-Rectangle-Tubing-VitroTubes

[11] Horiba Scientific, "Introduction to Raman Spectroscopy." [Online]. Available: http://www.horiba.com/uk/scientific/products/raman-spectroscopy/raman-academy/raman-tutorial/raman-scattering/

[12] D. Levitt, A. Jackson, C. Heinson, L. N. Britton, T. Malik, V. Dwarakanath, and G. A. Pope, "Identification and Evaluation of High-Performance EOR Surfactants," in *SPE/DOE Symposium on Improved Oil Recovery*, no. April. Tulsa: Society of Petroleum Engineers, Apr. 2006, pp. 243–253. [Online]. Available: https://www.onepetro.org/journal-paper/SPE-100089-PA

[13] B. O. Metz, H. C. Davidson, M. L. de Coninck, and L. A. M. (eds.), "IPCC Special Report on Carbon Dioxide Capture and Storage," Working Group III of the Intergovernmental Panel on Climate Change, Cambridge, Tech. Rep., 2005. [Online]. Available: http://www.ipcc.ch/pdf/special-reports/srccs/srccs_wholereport.pdf

[14] T. A. Boden, G. Marland, and R. J. Andres, "Global, regional, and national fossil-fuel CO_2 emissions," *Carbon Dioxide Information Analysis Center, Oak Ridge National Laboratory, US Department of Energy, Oak Ridge, Tenn., USA*, vol. 10, 2009.

[15] S. Bachu and J. Adams, "Sequestration of CO_2 in geological media in response to climate change: capacity of deep saline aquifers to sequester CO_2 in solution," *Energy Conversion and Management*, vol. 44, no. 20, pp. 3151–3175, Dec. 2003. [Online]. Available: http://linkinghub.elsevier.com/retrieve/pii/S0196890403001018

[16] K. S. Lackner, "Climate change. A guide to CO_2 sequestration."

Science (New York, N.Y.), vol. 300, no. 5626, pp. 1677–8, Jun. 2003. [Online]. Available: http://www.ncbi.nlm.nih.gov/pubmed/12805529

[17] S. Bachu, "Sequestration of CO_2 in geological media: criteria and approach for site selection in response to climate change," *Energy Conversion and Management*, vol. 41, no. 9, pp. 953–970, Jun. 2000. [Online]. Available: http://linkinghub.elsevier.com/retrieve/pii/S0196890499001491

[18] S. Bachu, "Screening and ranking of sedimentary basins for sequestration of CO_2 in geological media in response to climate change," *Environmental Geology*, vol. 44, no. 3, pp. 277–289, 2003. [Online]. Available: http://dx.doi.org/10.1007/s00254-003-0762-9

[19] R. Juanes, E. J. Spiteri, F. M. Orr, and M. J. Blunt, "Impact of relative permeability hysteresis on geological CO_2 storage," *Water Resources Research*, vol. 42, no. 12, pp. 1–13, Dec. 2006. [Online]. Available: http://doi.wiley.com/10.1029/2005WR004806

[20] Y. Tanino and M. J. Blunt, "Capillary trapping in sandstones and carbonates: Dependence on pore structure," *Water Resources Research*, vol. 48, no. 8, pp. 1–13, Aug. 2012. [Online]. Available: http://doi.wiley.com/10.1029/2011WR011712

[21] R. Qi, T. Laforce, and M. Blunt, "Design of carbon dioxide storage in aquifers," *International Journal of Greenhouse Gas Control*, vol. 3, no. 2, pp. 195–205, Mar. 2009. [Online]. Available: http://linkinghub.elsevier.com/retrieve/pii/S1750583608000765

[22] E. H. Oelkers, S. R. Gislason, and J. Matter, "Mineral Carbonation of CO_2," *Elements*, vol. 4, no. 5, pp. 333–337, Oct. 2008. [Online]. Available: http://elements.geoscienceworld.org/cgi/doi/10.2113/gselements.4.5.333

[23] W. D. Gunter, B. Wiwehar, and E. H. Perkins, "Aquifer disposal of CO_2-rich greenhouse gases: Extension of the time scale of experiment for CO_2-sequestering reactions by geochemical modelling," *Mineralogy and Petrology*, vol. 59, no. 1-2, pp. 121–140, 1997. [Online]. Available: http://link.springer.com/10.1007/BF01163065

[24] S. Bachu, W. Gunter, and E. Perkins, "Aquifer disposal of CO_2: Hydrodynamic and mineral trapping," *Energy Conversion and Management*, vol. 35, no. 4, pp. 269–279, Apr. 1994. [Online]. Available: http://www.sciencedirect.com/science/article/pii/0196890494900604

[25] S. M. Benson and D. R. Cole, "CO_2 Sequestration in Deep Sedimentary Formations," *Elements*, vol. 4, no. 5, pp. 325–331, Oct. 2008. [Online]. Available: http://elements.geoscienceworld.org/cgi/doi/10.2113/gselements.4.5.325

[26] S. Taku Ide, K. Jessen, and F. M. Orr, "Storage of CO_2 in saline aquifers: Effects of gravity, viscous, and capillary forces on amount and timing of trapping," *International Journal of Greenhouse Gas Control*, vol. 1, no. 4, pp. 481–491, Oct. 2007. [Online]. Available: http://linkinghub.elsevier.com/retrieve/pii/S1750583607000916

[27] M. A. Hesse, F. M. Orr, and H. A. Tchelepi, "Gravity currents with residual trapping," *Journal of Fluid Mechanics*, vol. 611, pp. 35–60, Aug. 2008. [Online]. Available: http://www.journals.cambridge.org/abstract_S002211200800219X

[28] C. Chalbaud, M. Robin, S. Bekri, and P. Egermann, "Wettability Impact on CO_2 Storage in Aquifers: Visualisation and Quantification using Micromodel Tests, Pore Network Model and Reservoir Simulations," in *SCA International Symposium*, Calgary, Canada, 2007. [Online]. Available: http://www.scaweb.org/assets/papers/2007_papers/09.pdf

[29] C. Chalbaud, J.-M. Lombard, F. Martin, M. Robin, H. Bertin, and P. Egermann, "Two Phase Flow Properties of Brine-CO_2 Systems in a Carbonate Core: Influence of Wettability on Pc and kr." in *Proceedings of SPE/EAGE Reservoir Characterization and Simulation Conference*. Abu Dhabi, U.A.E.: Society of Petroleum Engineers, Oct. 2007, pp. 1–10. [Online]. Available: http://www.spe.org/elibrary/servlet/spepreview?id=SPE-111420-MS

[30] P.-E. Øren, S. Bakke, and O. Arntzen, "Extending Predictive Capabilities to Network Models," *SPE Journal*, vol. 3, no. 04, pp.

324–336, Apr. 1998. [Online]. Available: http://www.onepetro.org/doi/10.2118/52052-PA

[31] P. Øren and S. Bakke, "Process based reconstruction of sandstones and prediction of transport properties," *Transport in Porous Media*, vol. 46, pp. 311–343, 2002. [Online]. Available: http://link.springer.com/article/10.1023/A:1015031122338

[32] P. l.-E. Øren and S. Bakke, "Reconstruction of Berea sandstone and pore-scale modelling of wettability effects," *Journal of Petroleum Science and Engineering*, vol. 39, pp. 177–199, Sep. 2003. [Online]. Available: http://linkinghub.elsevier.com/retrieve/pii/S0920410503000627

[33] P. Valvatne and M. J. Blunt, "Predictive pore-scale network modeling," in *SPE Annual Technical Conference and Exhibition*, Denver, Colorado, 2003. [Online]. Available: http://www.onepetro.org/mslib/servlet/onepetropreview?id=00084550&soc=SPE

[34] V. Alvarado and E. Manrique, "Enhanced Oil Recovery: An Update Review," *Energies*, vol. 3, no. 9, pp. 1529–1575, Aug. 2010. [Online]. Available: http://www.mdpi.com/1996-1073/3/9/1529/

[35] R. G. Miller and S. R. Sorrell, "The future of oil supply," *Philosophical Transactions of the Royal Society of London A: Mathematical, Physical and Engineering Sciences*, vol. 372, no. 2006, 2013.

[36] A. Muggeridge, A. Cockin, K. Webb, H. Frampton, I. Collins, T. Moulds, and P. Salino, "Recovery rates, enhanced oil recovery and technological limits," *Philosophical Transactions of the Royal Society of London A: Mathematical, Physical and Engineering Sciences*, vol. 372, no. 2006, 2013.

[37] R. Al-Mjeni, S. Arora, P. Cherukupalli, J. van Wunnik, J. Edwards, B. Felber, O. Gurpinar, G. J. Hirasaki, C. A. Miller, C. Jackson, M. Kristensen, F. Lim, and R. Ramamoorthy, "Has the Time Come for EOR?" *Oilfield Review*, vol. 6, no. 6, pp. 16–35, 2010. [Online]. Available: https://www.slb.com/~/media/Files/resources/oilfield_review/ors10/win10/eor.pdf

[38] I. Sandrea and R. Sandrea, "Global oil reserves - recovery factors leave vast target for EOR technologies," *Oil and Gas Journal*, pp. 1–8, 2007. [Online]. Available: http://www.ipc66.com/publications/Global_Oil__EOR_Challenge.pdf

[39] F. A. L. Dullien, *Porous Media Fluid Transport and Pore Structure*. London: Academic Press Inc, 1992.

[40] E. Washburn, "The dynamics of capillary flow," *Physical Review*, vol. 17, no. 3, p. 273, 1921. [Online]. Available: http://prola.aps.org/abstract/PR/v17/i3/p273_1

[41] M. Dreyer, A. Delgado, and H. Rath, "Capillary rise of liquid between parallel plates under microgravity," *Journal of Colloid and interface science*, vol. 163, pp. 158–168, 1994. [Online]. Available: http://www.sciencedirect.com/science/article/pii/S0021979784710927

[42] N. Ichikawa and Y. Satoda, "Interface dynamics of capillary flow in a tube under negligible gravity condition," *Journal of colloid and interface science*, vol. 162, pp. 350–355, 1994. [Online]. Available: http://www.sciencedirect.com/science/article/pii/S0021979784710496

[43] D. Petrash, T. Nelson, and E. Otto, "Effect of surface energy on the liquid-vapor interface configuration during weightlessness," *NASA*, 1963.

[44] D. Quéré, "Inertial capillarity," *EPL (Europhysics Letters)*, vol. 39, pp. 533–538, 1997. [Online]. Available: http://iopscience.iop.org/0295-5075/39/5/533

[45] R. Siegel, "Transient capillary rise in reduced and zero-gravity fields," *Journal of Applied Mechanics*, vol. 83, pp. 165–170, 1961. [Online]. Available: http://appliedmechanics.asmedigitalcollection.asme.org/article.aspx?articleid=1394496

[46] B. Zhmud, F. Tiberg, and K. Hallstensson, "Dynamics of Capillary Rise," *Journal of colloid and interface science*, vol. 228, no. 2, pp. 263–269, Aug. 2000. [Online]. Available: http://www.ncbi.nlm.nih.gov/pubmed/10926465

[47] E. K. Rideal, "CVIII. On the flow of liquids under capillary pressure," *Philosophical Magazine Series 6*, vol. 44, no. 264, pp. 1152–1159, Dec. 1922. [Online]. Available: http://www.tandfonline.com/doi/abs/10.1080/14786441008634082

[48] C. Bosanquet, "LV. On the flow of liquids into capillary tubes," *Philosophical Magazine Series 6*, vol. 45, no. 267, pp. 525–531, Mar. 1923. [Online]. Available: http://www.tandfonline.com/doi/abs/10.1080/14786442308634144

[49] J. Szekely, A. Neumann, and Y. Chuang, "The rate of capillary penetration and the applicability of the Washburn equation," *Journal of Colloid and Interface Science*, vol. 35, no. 2, pp. 273–278, 1971. [Online]. Available: http://linkinghub.elsevier.com/retrieve/pii/0021979771901202

[50] M. Stange, M. E. Dreyer, and H. J. Rath, "Capillary driven flow in circular cylindrical tubes," *Physics of Fluids*, vol. 15, no. 9, pp. 2587–2601, Sep. 2003. [Online]. Available: http://scitation.aip.org/content/aip/journal/pof2/15/9/10.1063/1.1596913

[51] G. Mason and N. R. Morrow, "Capillary behavior of a perfectly wetting liquid in irregular triangular tubes," *Journal of Colloid and Interface Science*, vol. 141, no. 1, pp. 262–274, Jan. 1991. [Online]. Available: http://www.sciencedirect.com/science/article/pii/002197979190321X

[52] M. Blunt and H. Scher, "Pore-level modeling of wetting," *Physical Review E*, vol. 52, no. 6, pp. 6387–6403, 1995. [Online]. Available: http://pre.aps.org/abstract/PRE/v52/i6/p6387_1

[53] X. Lopez, P. H. Valvatne, and M. J. Blunt, "Predictive network modeling of single-phase non-Newtonian flow in porous media," *Journal of Colloid and Interface Science*, vol. 264, no. 1, pp. 256–265, Aug. 2003. [Online]. Available: http://linkinghub.elsevier.com/retrieve/pii/S0021979703003102

[54] P. Meakin and A. M. Tartakovsky, "Modeling and simulation of pore-scale multiphase fluid flow and reactive transport in fractured

and porous media," *Reviews of Geophysics*, vol. 47, no. 3, pp. 1–47, Jul. 2009. [Online]. Available: http://doi.wiley.com/10.1029/2008RG000263

[55] T. W. Patzek, "Verification of a Complete Pore Network Simulator of Drainage and Imbibition," *SPE Journal*, vol. 6, no. 02, pp. 144–156, Apr. 2001. [Online]. Available: http://www.onepetro.org/doi/10.2118/71310-PA

[56] P. H. Valvatne and M. J. Blunt, "Predictive pore-scale modeling of two-phase flow in mixed wet media," *Water Resources Research*, vol. 40, no. 7, pp. 1–12, Jul. 2004. [Online]. Available: http://doi.wiley.com/10.1029/2003WR002627

[57] J. P. Crawshaw and E. S. Boek, "Multi-scale Imaging and Simulation of Structure, Flow and Reactive Transport for CO_2 Storage and EOR in Carbonate Reservoirs," *Reviews in Mineralogy and Geochemistry*, vol. 77, no. 1, pp. 431–458, Nov. 2013. [Online]. Available: http://rimg.geoscienceworld.org/cgi/doi/10.2138/rmg.2013.77.12

[58] R. Benzi, S. Succi, and M. Vergassola, "The lattice Boltzmann equation: theory and applications," *Physics Reports*, vol. 222, no. 3, pp. 145–197, 1992. [Online]. Available: http://www.sciencedirect.com/science/article/pii/037015739290090M

[59] H. Chen, S. Chen, and W. Matthaeus, "Recovery of the navier-stokes equations using a lattice-gas boltzmann method," *Phys. Rev. A*, vol. 45, pp. R5339–R5342, Apr 1992. [Online]. Available: http://link.aps.org/doi/10.1103/PhysRevA.45.R5339

[60] G. D. Doolen, *Lattice gas methods for partial differential equations: a volume of lattice gas reprints and articles, including selected papers from the workshop on large nonlinear systems, held August, 1987 in Los Alamos, New Mexico.* Addison-Wesley, 1990.

[61] S. Succi, *The Lattice-Boltzmann Equation.* Oxford university press, Oxford, 2001.

[62] M. C. Sukop and D. T. J. Thorne, *Lattice Boltzmann Modeling: An*

Introduction for Geoscientists and Engineers, 1st ed. Springer Publishing Company, Incorporated, 2007.

[63] A. Cancelliere, C. Chang, E. Foti, D. H. Rothman, and S. Succi, "The permeability of a random medium: Comparison of simulation with theory," *Physics of Fluids A: Fluid Dynamics (1989-1993)*, vol. 2, no. 12, pp. 2085–2088, 1990. [Online]. Available: http://scitation.aip.org/content/aip/journal/pofa/2/12/10.1063/1.857793

[64] M. Swift, E. Orlandini, W. Osborn, and J. Yeomans, "Lattice boltzmann simulations of liquid-gas and binary fluid systems," *Phys. Rev. E*, vol. 54, pp. 5041–5052, Nov 1996. [Online]. Available: http://link.aps.org/doi/10.1103/PhysRevE.54.5041

[65] M. Swift, W. Osborn, and J. Yeomans, "Lattice Boltzmann simulation of nonideal fluids," *Physical Review Letters*, vol. 75, no. 5, pp. 830–834, 1995. [Online]. Available: http://journals.aps.org/prl/abstract/10.1103/PhysRevLett.75.830

[66] D. D'Humières, I. Ginzburg, M. Krafczyk, P. Lallemand, and L.-S. Luo, "Multiple-relaxation-time lattice Boltzmann models in three dimensions." *Philosophical transactions. Series A, Mathematical, physical, and engineering sciences*, vol. 360, no. 1792, pp. 437–51, Mar. 2002. [Online]. Available: http://www.ncbi.nlm.nih.gov/pubmed/16214687

[67] J. Eastoe, "Surfactant Chemistry." [Online]. Available: http://www.chm.bris.ac.uk/eastoe/Surf_Chem/Surfactant.htm

[68] M. J. Rosen, "Characteristic Features of Surfactants," in *Surfactants and Interfacial Phenomena*. New York: Wiley, 2004, ch. 1, pp. 1–33.

[69] J. J. Sheng, "Surfactant Flooding," in *Modern Chemical Enhanced Oil Recovery: Theory and Practice*. Elsevier, 2011, ch. 7, pp. 239–335.

[70] L. Uren and E. Fahmy, "Factors Influencing the Recovery of Petroleum from Unconsolidated Sands by Waterflooding," *Transactions of the AIME*, vol. 77, no. 01, pp. 318–335, Apr. 1927. [Online]. Available: https://www.onepetro.org/journal-paper/SPE-927318-G

[71] G. Hirasaki, C. A. Miller, and M. Puerto, "Recent Advances in Surfactant EOR," in *SPE Annual Technical Conference and Exhibition*, vol. 16, no. 04, Denver, Colorado, Apr. 2008, p. SPE115386. [Online]. Available: https://www.onepetro.org/journal-paper/SPE-115386-PA

[72] J. R. Barnes, J. Smit, J. Smit, G. Shpakoff, K. H. Raney, and M. Puerto, "Development of Surfactants for Chemical Flooding at Difficult Reservoir Conditions," in *SPE Symposium on Improved Oil Recovery*. Society of Petroleum Engineers, Apr. 2013. [Online]. Available: https://www.onepetro.org/conference-paper/SPE-113313-MShttp://op.spe.semcs.net/doi/10.2118/113313-MS

[73] I. Chatzis and N. R. Morrow, "Correlation of Capillary Number Relationships for Sandstone," *Society of Petroleum Engineers Journal*, vol. 24, no. 05, pp. 555–562, Apr. 2013. [Online]. Available: http://www.onepetro.org/doi/10.2118/10114-PA

[74] E. C. Donaldson, G. V. Chilingarian, and T. F. Yen, *Enhanced Oil Recovery 2: Processes and Operations*. Amsterdam; Oxford: Elsevier, 1989.

[75] T. F. Tadros, "Introduction," in *Applied Surfactants: Principles and Applications*. Weinheim: Wiley-VCH, 2006, ch. 1, pp. 1–16.

[76] S. Global, "ENORDET Surfactants," 2014. [Online]. Available: http://www.shell.com/global/products-services/solutions-for-businesses/chemicals/products/alpha-olefins-detergent-alcohols/enordet-surfactants.html

[77] P. Winsor, "Hydrotropy, solubilisation and related emulsification processes," *Transactions of the Faraday Society*, no. 1942, pp. 376–398, 1948. [Online]. Available: http://pubs.rsc.org/EN/content/articlepdf/1948/tf/tf9484400376

[78] T. P. Hoar and J. H. Schulman, "Transparent Water-in-Oil Dispersions: the Oleopathic Hydro-Micelle," *Nature*, vol. 152, no. 3847, pp. 102–103, Jul. 1943. [Online]. Available: http://adsabs.harvard.edu/abs/1943Natur.152..102H

[79] J. H. Schulman, W. Stoeckenius, and L. M. Prince, "Mechanism of Formation and Structure of Micro Emulsions by Electron Microscopy," *The Journal of Physical Chemistry*, vol. 63, no. 10, pp. 1677–1680, Oct. 1959. [Online]. Available: http://pubs.acs.org/doi/abs/10.1021/j150580a027

[80] I. Danielsson and B. Lindman, "The definition of microemulsion," *Colloids and Surfaces*, vol. 3, no. 4, pp. 391–392, Dec. 1981. [Online]. Available: http://linkinghub.elsevier.com/retrieve/pii/0166662281800649

[81] T. F. Tadros, "Microemulsions," in *Applied Surfactants: Principles and Applications*. Weinheim: Wiley-VCH, 2006, ch. 10, pp. 309–334.

[82] R. Nelson and G. Pope, "Phase relationships in chemical flooding," *Society of Petroleum Engineers Journal*, pp. 325–338, 1978. [Online]. Available: https://www.onepetro.org/journal-paper/SPE-6773-PA

[83] P. Tabeling, *Introduction to Microfluidics*. Oxford: Oxford University Press, 2005.

[84] N. K. Karadimitriou and S. M. Hassanizadeh, "A Review of Micromodels and Their Use in Two-Phase Flow Studies," *Vadose Zone Journal*, vol. 11, no. 3, 2012. [Online]. Available: https://www.soils.org/publications/vzj/abstracts/11/3/vzj2011.0072

[85] A. Chatenever and J. C. Calhoun, "Visual Examinations of Fluid Behavior in Porous Media - Part I," *Journal of Petroleum Technology*, vol. 4, no. 06, pp. 149–156, Apr. 1952. [Online]. Available: http://www.onepetro.org/doi/10.2118/135-G

[86] C. Mattax and J. Kyte, "Ever see a water flood?" *Oil and Gas Journal*, vol. 59, pp. 115–128, 1961.

[87] J. Davis Jr. and S. Jones, "Displacement Mechanisms of Micellar Solutions," *Journal of Petroleum Technology*, vol. 20, no. 12, pp. 1415–1428, Apr. 1968. [Online]. Available: https://www.onepetro.org/journal-paper/SPE-1847-2-PA

[88] M. McKellar and N. Wardlaw, "A method of making two-dimensional glass micromodels of pore systems," *Journal of Canadian Petroleum*

Technology, vol. 21, no. 04, pp. 39–41, 1982. [Online]. Available: https://www.onepetro.org/journal-paper/PETSOC-82-04-03

[89] J. Hornbrook, L. Castanier, and P. Pettit, "Observation of Foam/Oil Interactions in a New, High-Resolution Micromodel," in *SPE Annual Technical Conference and Exhibition*. Society of Petroleum Engineers, Apr. 1991, pp. 377–382. [Online]. Available: http://www.onepetro.org/doi/10.2118/22631-MS

[90] J. Bell and F. Cameron, "The flow of liquids through capillary spaces," *The Journal of Physical Chemistry*, vol. 10, no. 8, pp. 658–674, 1906. [Online]. Available: http://pubs.acs.org/doi/abs/10.1021/j150080a005

[91] N. R. Tas, J. Haneveld, H. V. Jansen, M. Elwenspoek, and A. van den Berg, "Capillary filling speed of water in nanochannels," *Applied Physics Letters*, vol. 85, no. 15, pp. 3274–3276, 2004. [Online]. Available: http://scitation.aip.org/content/aip/journal/apl/85/15/10.1063/1.1804602

[92] A. Hamraoui, K. Thuresson, T. Nylander, and V. Yaminsky, "Can a Dynamic Contact Angle Be Understood in Terms of a Friction Coefficient?" *Journal of Colloid and Interface Science*, vol. 226, no. 2, pp. 199–204, Jun. 2000. [Online]. Available: http://linkinghub.elsevier.com/retrieve/pii/S0021979700968309

[93] M. Heshmati and M. Piri, "Experimental investigation of dynamic contact angle and capillary rise in tubes with circular and noncircular cross sections." *Langmuir*, vol. 30, no. 47, pp. 14 151–62, Dec. 2014. [Online]. Available: http://pubs.acs.org/doi/abs/10.1021/la501724y

[94] T. E. Mumley, C. Radke, and M. C. Williams, "Kinetics of liquid/liquid capillary rise I. Experimental Observations," *Journal of Colloid and Interface Science*, vol. 109, no. 2, pp. 398–412, Feb. 1986. [Online]. Available: http://www.sciencedirect.com/science/article/pii/0021979786903188

[95] A. Siebold, M. Nardin, J. Schultz, A. Walliser, and M. Oppliger, "Effect of dynamic contact angle on capillary rise phenomena,"

Colloids and Surfaces A: Physicochemical and Engineering Aspects, vol. 161, no. 1, pp. 81–87, Jan. 2000. [Online]. Available: http://linkinghub.elsevier.com/retrieve/pii/S0927775799003271

[96] S. Ma, G. Mason, and N. Morrow, "Effect of contact angle on drainage and imbibition in regular polygonal tubes," *Colloids and Surfaces A: Physicochemical and Engineering Aspects*, vol. 117, pp. 273–291, 1996. [Online]. Available: http://www.sciencedirect.com/science/article/pii/0927775796037028

[97] J. Bico, C. Tordeux, and D. Quéré, "Rough wetting," *EPL (Europhysics Letters)*, vol. 55, no. July, pp. 214–220, 2001. [Online]. Available: http://iopscience.iop.org/0295-5075/55/2/214

[98] R. Lenormand and C. Zarcone, "Role Of Roughness And Edges During Imbibition In Square Capillaries," in *SPE Annual Technical Conference and Exhibition*. Society of Petroleum Engineers, Apr. 1984, pp. 1–17. [Online]. Available: http://www.onepetro.org/doi/10.2118/13264-MS

[99] N. R. Morrow, "The Effects of Surface Roughness On Contact: Angle With Special Reference to Petroleum Recovery," *Journal of Canadian Petroleum Technology*, vol. 14, no. 04, pp. 42–53, Apr. 1975. [Online]. Available: http://www.onepetro.org/doi/10.2118/75-04-04

[100] D. Quéré, "Wetting and Roughness," *Annual Review of Materials Research*, vol. 38, no. 1, pp. 71–99, Aug. 2008. [Online]. Available: http://www.annualreviews.org/doi/abs/10.1146/annurev.matsci.38.060407.132434

[101] R. N. Wenzel, "Surface Roughness and Contact Angle." *The Journal of Physical and Colloid Chemistry*, vol. 53, no. 9, pp. 1466–1467, Sep. 1949. [Online]. Available: http://pubs.acs.org/doi/abs/10.1021/j150474a015

[102] D. Dimitrov, A. Milchev, and K. Binder, "Capillary rise in nanopores: Molecular dynamics evidence for the lucas-washburn equation," *Phys. Rev. Lett.*, vol. 99, p. 054501, Jul 2007. [Online]. Available: http://link.aps.org/doi/10.1103/PhysRevLett.99.054501

[103] M. Stukan, P. Ligneul, J. Crawshaw, and E. Boek, "Spontaneous imbibition in nanopores of different roughness and wettability." *Langmuir*, vol. 26, no. 16, pp. 13 342–52, Aug. 2010. [Online]. Available: http://pubs.acs.org/doi/abs/10.1021/la101995t

[104] F. Diotallevi, L. Biferale, S. Chibbaro, G. Pontrelli, F. Toschi, and S. Succi, "Lattice Boltzmann simulations of capillary filling: Finite vapour density effects," *The European Physical Journal Special Topics*, vol. 171, no. 1, pp. 237–243, May 2009. [Online]. Available: http://www.springerlink.com/index/10.1140/epjst/e2009-01034-6

[105] C. M. Pooley, H. Kusumaatmaja, and J. M. Yeomans, "Modelling capillary filling dynamics using lattice Boltzmann simulations," *The European Physical Journal Special Topics*, vol. 171, pp. 63–71, May 2009. [Online]. Available: http://www.springerlink.com/index/10.1140/epjst/e2009-01012-0

[106] D. Avraam, G. Kolonis, T. Roumeliotis, G. Constantinides, and A. Payatakes, "Steady-state two-phase flow through planar and nonplanar model porous media," *Transport in porous media*, vol. 16, pp. 75–101, 1994. [Online]. Available: http://link.springer.com/article/10.1007/BF01059777

[107] L.-C. Chang, J.-P. Tsai, H.-Y. Shan, and H.-H. Chen, "Experimental study on imbibition displacement mechanisms of two-phase fluid using micro model," *Environmental Earth Sciences*, vol. 59, no. 4, pp. 901–911, Feb. 2009. [Online]. Available: http://www.springerlink.com/index/10.1007/s12665-009-0085-6

[108] D. Chen, L. J. Pyrak-Nolte, J. Griffin, and N. J. Giordano, "Measurement of interfacial area per volume for drainage and imbibition," *Water Resources Research*, vol. 43, no. 12, pp. 1–6, Dec. 2007. [Online]. Available: http://doi.wiley.com/10.1029/2007WR006021

[109] J.-D. Chen and D. Wilkinson, "Pore-scale viscous fingering in porous media," *Phys. Rev. Lett.*, vol. 55, pp. 1892–1895, Oct 1985. [Online]. Available: http://link.aps.org/doi/10.1103/PhysRevLett.55.1892

[110] M. Y. Corapcioglu, S. Yoon, and S. Chowdhury, "Pore-Scale Analysis of NAPL Blob Dissolution and Mobilization in Porous Media," *Transport in Porous Media*, vol. 79, no. 3, pp. 419–442, Jan. 2009. [Online]. Available: http://link.springer.com/10.1007/s11242-008-9331-8

[111] C. Cottin, H. Bodiguel, and A. Colin, "Drainage in two-dimensional porous media: From capillary fingering to viscous flow," *Physical Review E*, vol. 82, no. 4, p. 046315, Oct. 2010. [Online]. Available: http://link.aps.org/doi/10.1103/PhysRevE.82.046315

[112] D. Crandall, G. Ahmadi, M. Ferer, and D. H. Smith, "Distribution and occurrence of localized-bursts in two-phase flow through porous media," *Physica A: Statistical Mechanics and its Applications*, vol. 388, no. 5, pp. 574–584, Mar. 2009. [Online]. Available: http://linkinghub.elsevier.com/retrieve/pii/S0378437108009539

[113] C. Tsakiroglou, M. Theodoropoulou, V. Karoutsos, D. Papanicolaou, and V. Sygouni, "Experimental study of the immiscible displacement of shear-thinning fluids in pore networks," *Journal of Colloid and Interface Science*, vol. 267, no. 1, pp. 217–232, Nov. 2003. [Online]. Available: http://linkinghub.elsevier.com/retrieve/pii/S0021979703006350

[114] C. Tsakiroglou, O. Vizika-Kavvadias, and R. Lenormand, "Use of micromodels to study multiphase flow in porous media," in *International Symposium of the Society of Core Analysts*, Napa Valley, California, 2013, pp. 1–13. [Online]. Available: http://www.scaweb.org/assets/papers/2013_papers/SCA2013-038.pdf

[115] M. Ferer, C. Ji, G. Bromhal, J. Cook, G. Ahmadi, and D. Smith, "Crossover from capillary fingering to viscous fingering for immiscible unstable flow: Experiment and modeling," *Physical Review E*, vol. 70, no. 1, pp. 1–7, Jul. 2004. [Online]. Available: http://link.aps.org/doi/10.1103/PhysRevE.70.016303

[116] J. W. Grate, C. Zhang, T. W. Wietsma, M. G. Warner, N. C. Anheier, B. E. Bernacki, G. Orr, and M. Oostrom, "A note on the visualization of wetting film structures and a nonwetting immiscible

fluid in a pore network micromodel using a solvatochromic dye," *Water Resources Research*, vol. 46, no. 11, pp. 1–6, Nov. 2010. [Online]. Available: http://doi.wiley.com/10.1029/2010WR009419

[117] R. Lenormand, "Liquids in porous media," *Journal of Physics: Condensed Matter*, vol. 79, pp. 79–88, 1990. [Online]. Available: http://iopscience.iop.org/0953-8984/2/S/008

[118] E. Rangel-German, S. Akin, and L. Castanier, "Multiphase-flow properties of fractured porous media," in *SPE Western Regional Meeting*, vol. 51, no. 3-4, May 1999, p. SPE 54591. [Online]. Available: http://linkinghub.elsevier.com/retrieve/pii/S0920410506000118

[119] E. R. Rangel-German and A. R. Kovscek, "A micromodel investigation of two-phase matrix-fracture transfer mechanisms," *Water Resources Research*, vol. 42, no. 3, pp. 1–13, Mar. 2006. [Online]. Available: http://doi.wiley.com/10.1029/2004WR003918

[120] E. Rangel-German and A. Kovscek, "Experimental and analytical study of multidimensional imbibition in fractured porous media," *Journal of Petroleum Science and Engineering*, vol. 36, no. 1-2, pp. 45–60, Oct. 2002. [Online]. Available: http://linkinghub.elsevier.com/retrieve/pii/S0920410502002504

[121] C. Zhang, M. Oostrom, T. W. Wietsma, J. W. Grate, and M. G. Warner, "Influence of Viscous and Capillary Forces on Immiscible Fluid Displacement: Pore-Scale Experimental Study in a Water-Wet Micromodel Demonstrating Viscous and Capillary Fingering," *Energy & Fuels*, vol. 25, no. 8, pp. 3493–3505, Aug. 2011. [Online]. Available: http://pubs.acs.org/doi/abs/10.1021/ef101732k

[122] H. Amani, M. H. Sarrafzadeh, M. Haghighi, and M. R. Mehrnia, "Comparative study of biosurfactant producing bacteria in MEOR applications," *Journal of Petroleum Science and Engineering*, vol. 75, no. 1-2, pp. 209–214, Dec. 2010. [Online]. Available: http://linkinghub.elsevier.com/retrieve/pii/S0920410510002524

[123] R. Armstrong and S. Berg, "Interfacial velocities and capillary pressure gradients during haines jumps," *Phys. Rev. E*, vol. 88, p.

043010, Oct 2013. [Online]. Available: http://link.aps.org/doi/10.1103/PhysRevE.88.043010

[124] C. M. Crescente, A. Rekdal, A. Abraiz, O. Torsaeter, L. Hultmann, A. Stroem, K. Rasmussen, and E. Kowalewski, "A Pore Level Study of MIOR Displacement Mechanisms in Glass Micromodels Using *Rhodococcus* sp. 094," in *SPE Symposium on Improved Oil Recovery*. Tulsa, Oklahoma: Society of Petroleum Engineers, Apr. 2008, pp. 1–20. [Online]. Available: http://www.onepetro.org/doi/10.2118/110134-MS

[125] M. Dong, Q. Liu, and A. Li, "Micromodel Study of the Displacement Mechanisms of Enhanced Heavy Oil Recovery by Alkaline Flooding," in *International Symposium of the Society of Core Analysts*, Calgary, Canada, 2007, pp. 1–6. [Online]. Available: http://scaweb.org/assets/papers/2007_papers/47.pdf

[126] H. Hematpour, M. Mardi, S. Edalatkhah, and R. Arabjamaloei, "Experimental Study of Polymer Flooding in Low-Viscosity Oil Using One-Quarter Five-Spot Glass Micromodel," *Petroleum Science and Technology*, vol. 29, no. 11, pp. 1163–1175, Apr. 2011. [Online]. Available: http://www.tandfonline.com/doi/abs/10.1080/10916460903514964

[127] A. Keller, M. Blunt, and A. Roberts, "Micromodel observation of the role of oil layers in three-phase flow," *Transport in Porous Media*, vol. 26, no. 3, pp. 277–297, 1997. [Online]. Available: http://www.springerlink.com/index/r728v5681vu271lq.pdf

[128] N.-T. Nguyen and S. T. Wereley, *Fundamentals and Applications of Microfluidics*. Boston; London: Artech House, 2002.

[129] M. Nourani, H. Panahi, A. Mohebbi, M. Haghighi, R. Roostaazad, and D. Biria, "Laboratory Studies of MEOR in the Micromodel as a Fractured System," in *Eastern Regional Meeting*. Lexington, Kentucky: Society of Petroleum Engineers, Apr. 2013, pp. 1–8. [Online]. Available: http://www.onepetro.org/doi/10.2118/110988-MS

[130] M. Riazi, M. Sohrabi, M. Jamiolahmady, S. Ireland, and C. Brown, "Oil Recovery Improvement Using CO2-Enriched Water Injection," in *EUROPEC/EAGE Conference and Exhibition.* Amsterdam, The Netherlands: Society of Petroleum Engineers, Apr. 2013, pp. 1–10. [Online]. Available: http://www.onepetro.org/doi/10.2118/121170-MS

[131] N. Sagar and L. Castanier, "Oil-foam interactions in a micromodel," *SUPRI-TR110 Report, Stanford University*, 1997. [Online]. Available: http://geo.stanford.edu/ERE/research/supria/publications/public/tr110.pdf

[132] M. Sohrabi, A. Danesh, and M. Jamiolahmady, "Visualisation of Residual Oil Recovery by Near-miscible Gas and SWAG Injection Using High-pressure Micromodels," *Transport in Porous Media*, vol. 74, no. 2, pp. 239–257, Jan. 2008. [Online]. Available: http://www.springerlink.com/index/10.1007/s11242-007-9193-5

[133] M. Sohrabi, G. Henderson, D. Tehrani, and A. Danesh, "Visualisation of Oil Recovery by Water Alternating Gas (WAG) Injection Using High Pressure Micromodels - Water-Wet System," in *SPE Annual Technical Conference and Exhibition.* Dallas, Texas: Society of Petroleum Engineers, Apr. 2000, pp. 1–8. [Online]. Available: http://www.onepetro.org/doi/10.2118/63000-MS

[134] M. Sohrabi, D. Tehrani, A. Danesh, and G. Henderson, "Visualization of Oil Recovery by Water-Alternating-Gas Injection Using High-Pressure Micromodels," *SPE Journal*, vol. 9, no. 3, pp. 290–301, Apr. 2004. [Online]. Available: http://www.onepetro.org/doi/10.2118/89000-PA

[135] J. Wang, M. Dong, and K. Asghari, "Effect of Oil Viscosity on Heavy Oil-Water Relative Permeability Curves," in *SPE/DOE Symposium on Improved Oil Recovery.* Tulsa, Oklahoma: Society of Petroleum Engineers, Apr. 2006, pp. 1–9. [Online]. Available: http://www.onepetro.org/doi/10.2118/99763-MS

[136] B. Yadali Jamaloei and R. Kharrat, "Analysis of microscopic displacement mechanisms of dilute surfactant flooding in oil-

wet and water-wet porous media," *Transport in Porous Media*, vol. 81, no. 1, pp. 1–19, Apr. 2009. [Online]. Available: http://www.springerlink.com/index/10.1007/s11242-009-9382-5

[137] N. S. K. Gunda, B. Bera, N. K. Karadimitriou, S. K. Mitra, and S. M. Hassanizadeh, "Reservoir-on-a-chip (ROC): a new paradigm in reservoir engineering." *Lab on a chip*, vol. 11, no. 22, pp. 3785–92, Nov. 2011. [Online]. Available: http://pubs.rsc.org/en/content/articlehtml/2011/lc/c1lc20556k

[138] G. Martic, F. Gentner, D. Seveno, D. Coulon, J. De Coninck, and T. D. Blake, "A Molecular Dynamics Simulation of Capillary Imbibition," *Langmuir*, vol. 18, no. 21, pp. 7971–7976, Oct. 2002. [Online]. Available: http://pubs.acs.org/doi/abs/10.1021/la020068n

[139] L. Yu (Y. Li) and N. C. Wardlaw, "Mechanisms of nonwetting phase trapping during imbibition at slow rates," *Journal of Colloid and Interface Science*, vol. 109, no. 2, pp. 473–486, Feb. 1986. [Online]. Available: http://linkinghub.elsevier.com/retrieve/pii/0021979786903255

[140] N. R. Morrow and G. Mason, "Recovery of oil by spontaneous imbibition," *Current Opinion in Colloid & Interface Science*, vol. 6, no. 4, pp. 321–337, Aug. 2001. [Online]. Available: http://linkinghub.elsevier.com/retrieve/pii/S1359029401001005

[141] Y. Mélean, D. Broseta, A. Hasmy, and R. Blossey, "Dispersion of imbibition fronts," *Europhysics Letters (EPL)*, vol. 62, no. 4, pp. 505–511, May 2003. [Online]. Available: http://iopscience.iop.org/0295-5075/62/4/505

[142] E. Saadatpoor, S. L. Bryant, and K. Sepehrnoori, "Effect of upscaling heterogeneous domain on CO_2 trapping mechanisms," *Energy Procedia*, vol. 4, pp. 5066–5073, Jan. 2011. [Online]. Available: http://linkinghub.elsevier.com/retrieve/pii/S1876610211007594

[143] T. K. Tokunaga, J. Wan, J.-W. Jung, T. W. Kim, Y. Kim, and W. Dong, "Capillary pressure and saturation relations for supercritical CO_2 and brine in sand: High-pressure $P_c(S_w)$

controller/meter measurements and capillary scaling predictions," *Water Resources Research*, vol. 49, pp. 4566–4579, Jun. 2013. [Online]. Available: http://doi.wiley.com/10.1002/wrcr.20316

[144] D. Hillel, *Soil and Water: Physical Principles and Processes.* New York; London: Academic Press, 1971.

[145] M. Dong and I. Chatzis, "The imbibition and flow of a wetting liquid along the corners of a square capillary tube," *Journal of Colloid and Interface Science*, vol. 172, no. 2, pp. 278 – 288, 1995. [Online]. Available: http://www.sciencedirect.com/science/article/pii/S0021979785712532

[146] J. H. Dymond and H. A. Øye, "Viscosity of Selected Liquid *n*-Alkanes," *Journal of Physical and Chemical Reference Data*, vol. 23, pp. 41–53, 1994. [Online]. Available: http://scitation.aip.org/content/aip/journal/jpcrd/23/1/10.1063/1.555943

[147] H. Kuhn and H.-D. Försterling, *Principles of physical chemistry: understanding molecules, molecular assemblies, supramolecular machines.* Wiley, Chichester, 1999.

[148] J. Yang and E. S. Boek, "A comparison study of multi-component Lattice Boltzmann models for flow in porous media applications," *Computers & Mathematics with Applications*, vol. 65, pp. 882–890, Mar. 2013. [Online]. Available: http://linkinghub.elsevier.com/retrieve/pii/S0898122112006839

[149] J. Yang, "Multi-scale simulation of multiphase multi-component flow in porous media using the Lattice Boltzmann Method," Ph.D. dissertation, Imperial College London, 2013.

[150] S. Berg, H. Ott, S. A. Klapp, A. Schwing, R. Neiteler, N. Brussee, A. Makurat, L. Leu, F. Enzmann, J.-O. Schwarz, M. Kersten, S. Irvine, and M. Stampanoni, "Real-time 3D imaging of Haines jumps in porous media flow." *Proceedings of the National Academy of Sciences of the United States of America*, vol. 110, no. 10, pp. 3755–9, Mar. 2013. [Online]. Available: http://www.pubmedcentral.nih.gov/articlerender.fcgi?artid=3593852&tool=pmcentrez&rendertype=abstract

[151] P. A. Gauglitz and C. J. Radke, "Dynamics of Haines jumps for compressible bubbles in constricted capillaries," *AIChE Journal*, vol. 35, no. 2, pp. 230–240, Feb. 1989. [Online]. Available: http://doi.wiley.com/10.1002/aic.690350207

[152] J. Bico and D. Quéré, "Precursors of impregnation," *EPL (Europhysics Letters)*, vol. 61, pp. 348–353, 2003. [Online]. Available: http://iopscience.iop.org/0295-5075/61/3/348

[153] H. Kavehpour, B. Ovryn, and G. McKinley, "Microscopic and macroscopic structure of the precursor layer in spreading viscous drops," *Phys. Rev. Lett.*, vol. 91, p. 196104, Nov 2003. [Online]. Available: http://link.aps.org/doi/10.1103/PhysRevLett.91.196104

[154] M. Prodanović and S. L. Bryant, "A level set method for determining critical curvatures for drainage and imbibition," *Journal of Colloid and Interface Science*, vol. 304, no. 2, pp. 442 – 458, 2006. [Online]. Available: http://www.sciencedirect.com/science/article/pii/S0021979706007764

[155] M. Gladkikh and S. Bryant, "Prediction of imbibition from grain-scale interface movement," *Advances in Water Resources*, vol. 30, no. 2, pp. 249–260, Feb. 2007. [Online]. Available: http://linkinghub.elsevier.com/retrieve/pii/S0309170806000224

[156] W. Haynes, *CRC Handbook of Chemistry and Physics, 93rd Edition*, ser. CRC Handbook of Chemistry and Physics. Taylor & Francis, 2012.

[157] K. Humphry, M. van der Lee, E. Ineke, D. Van Bantenburg, and J. Southwick, "Microemulsion Flow in Porous Media: Implications for Alkaline-Surfactant-Polymer Flooding," in *SPE Enhanced Oil Recovery Conference*, Kuala Lumpur, Malaysia, 2013, pp. 1–13. [Online]. Available: https://www.onepetro.org/conference-paper/SPE-165233-MS

[158] L. Paterson, V. Hornof, and G. Neale, "Visualization of a Surfactant Flood of an Oil-Saturated Porous Medium," *Society of Petroleum Engineers Journal*, vol. 24, no. 03, pp. 325–327, Apr. 1984. [Online]. Available: http://www.onepetro.org/doi/10.2118/11598-PA

[159] P. G. Brewer, G. Malby, J. D. Pasteris, S. N. White, E. T. Peltzer, B. Wopenka, J. Freeman, and M. O. Brown, "Development of a laser Raman spectrometer for deep-ocean science," *Deep Sea Research Part I: Oceanographic Research Papers*, vol. 51, no. 5, pp. 739–753, May 2004. [Online]. Available: http://linkinghub.elsevier.com/retrieve/pii/S0967063704000135

[160] F. Pérez and J. Martinez-Frias, "Raman spectroscopy goes to Mars," *Spectroscopy Europe*, vol. 18, no. 1, pp. 18–21, 2006. [Online]. Available: http://tierra.rediris.es/publipapers/Raman_Spectroscopy_Europe.pdf

[161] A. F. Chrimes, K. Khoshmanesh, P. R. Stoddart, A. Mitchell, and K. Kalantar-Zadeh, "Microfluidics and Raman microscopy: current applications and future challenges." *Chemical Society reviews*, vol. 42, no. 13, pp. 5880–906, Jul. 2013. [Online]. Available: http://pubs.rsc.org/en/content/articlehtml/2013/cs/c3cs35515b

[162] N. Colthup, L. H. Daly, and S. E. Wiberley, *Introduction to infrared and raman spectroscopy*, 3rd ed. Boston ; London: Academic Press, 1990.

[163] C. Raman and K. Krishnan, "A new type of secondary radiation," *Nature*, vol. 121, pp. 501–502, 1928. [Online]. Available: http://repository.ias.ac.in/28460/

[164] C. Raman, "A new radiation," *Indian Journal of physics*, vol. 2, no. March, pp. 387–398, 1928. [Online]. Available: http://repository.ias.ac.in/70648/1/36-PUb.pdf

[165] C. V. Raman, "A Change of Wave-length in Light Scattering," *Nature*, vol. 121, no. 3051, pp. 619–619, Apr. 1928. [Online]. Available: http://www.nature.com/doifinder/10.1038/121619b0

[166] P. Larkin, *Infrared and raman spectroscopy : Principles and spectral interpretation*. Amsterdam ; Boston: Elsevier, 2011.

[167] P. Atkins and J. de Paula, *Atkins' Physical Chemistry*. Oxford University Press, 2014.

[168] J. R. Barnes, J. Smit, J. Smit, G. Shpakoff, K. H. Raney, and M. Puerto, "Development of Surfactants for Chemical Flooding at Difficult Reservoir Conditions," in *SPE Symposium on Improved Oil Recovery*. Tulsa, Oklahoma: Society of Petroleum Engineers, Apr. 2008, pp. 1–18. [Online]. Available: http://www.onepetro.org/doi/10.2118/113313-MS

[169] J. R. Barnes, H. Dirkzwager, J. Smit, J. Smit, A. On, R. C. Navarrete, B. Ellison, and M. A. Buijse, "Application of Internal Olefin Sulfonates and Other Surfactants to EOR. Part 1: Structure - Performance Relationships for Selection at Different Reservoir Conditions," in *SPE Improved Oil Recovery Symposium*. Tulsa, Oklahoma: Society of Petroleum Engineers, Apr. 2010, pp. 1–16. [Online]. Available: http://www.onepetro.org/doi/10.2118/129766-MS

Appendices

A. MatLab Code

```
clear

ref2=[
9   0.005
11  0.015
13  0.069
15  0.086
17  0.084
19  0.072
23  0.108
25  0.059
27  0.076
29  0.041
31  0.039
32  0.035
34  0.024
36  0.019
38  0.019
40  0.011
42  0.013
46  0.016
48  0.013
50  0.006
52  0.010
54  0.008
56  0.006
58  0.004
60  0.004
64  0.009
68  0.002
70  0.002
73  0.002
```

```
77  0.002
83  0.002
85  0.002
87  0.002
91  0.002
95  0.002
];

%[kx,ky]=

%ref2(:,2)=ref2(:,2)-min(ref2(:,2));

%=============give pore size distribution
    here=======================

ref1=[
12  0.95
17  24.05
22  47.15
27  78.16
32  63.29
37  25.00
42  17.09
47  7.91
52  11.08
57  4.11
62  3.16
72  3.16
77  1.90
82  5.06
102 3.16
107 1.90
112 1.90
137 0.95
142 0.63
152 0.63
157 0.63
];

%ref1=ref2;
```

```
pore_r_min=12;
pore_r_max=157;
%=========================================================================

%ref1(:,2)=ref1(:,2)-min(ref1(:,2));

r_min=9;
r_max=95;
r_ave=30;
sigma=16.0;
kappa=1.0;
%===========parameter for micromodels=============
d=10;
b=d/5*8;
a=d/5*24;
c=d/5*140;
left=round(c*1);  %=========parameter==========
right=round(c*1);
up=round(c*0.8);
down=round(c*1);
reservior=120;
lx=20;              %junction number in X direction
ly=10;              %junction number in Y direction
%=====================================================

r=r_min:0.05:r_max;

%======================USE
    EQUATIONS=======================================
% P=kappa*(r_max-r).*(r-r_min).*exp(-(r-r_ave).^2/(2*sigma^2));
% %P=kappa*(r_max-r).*(r-r_min)
% %plot (r,P);
%
%
%
%
% rrr=r;
% PPP=P;
% ss=trapz(r,P);
%
```

```
% num=[];
% r=r_min:0.05:r_min+0.5;
% P=kappa*(r_max-r).*(r-r_min).*exp(-(r-r_ave).^2/(2*sigma^2));
% num=[num,trapz(r,P)];
%
% for i=r_min+1:r_max-1
%     r=i-0.5:0.05:i+0.5;
%     P=kappa*(r_max-r).*(r-r_min).*exp(-(r-r_ave).^2/(2*sigma^2));
%     num=[num,trapz(r,P)];
% end
%
% r=r_max-0.5:0.05:r_max;
% P=kappa*(r_max-r).*(r-r_min).*exp(-(r-r_ave).^2/(2*sigma^2));
% num=[num,trapz(r,P)];
%
% num=num/ss;
% plot(num);
% hold on
% plot (ref2(:,1),ref2(:,2),'x');
% hold off
%
%
% dist=[0.0];tmp=0;
% for i=1:r_max-r_min+1
%     tmp=tmp+num(i);
%     dist=[dist,tmp];
% end
%=================================================================

%=======for channels=========================================

mimax=size(ref2,1);%ss=trapz(ref1(:,1),ref1(:,2));
dist=[0.0];tmp=0;mi=1;num=[];tmp2=0;
for i=1:r_max-r_min+1
    tmp2=0;
    if (mi<mimax)
        while ((ref2(mi,1)-r_min+1>=i) && (ref2(mi,1)-r_min+1<i+1))
            tmp=tmp+ref2(mi,2)*(ref2(mi+1,1)-ref2(mi,1));
            mi=mi+1;
        end
```

```
%     while (mi<mimax) && (ref2(mi,1)<i-r_min+1)
%         tmp=tmp+ref2(mi,2)*(ref2(mi+1,1)-ref2(mi,1));
%         tmp2=tmp2+ref2(mi,2)*(ref2(mi+1,1)-ref2(mi,1));
%         mi=mi+1;
%     end

    dist=[dist,tmp];
    end
    %dist=[dist,tmp];
%     i
%     mi
%     ref2(mi,1)-r_min+1
%    tmp
    num=[num,tmp2];
end
dist=dist/tmp;
%num=num/tmp;
%=============================================================

%=======for pores=============================================

mimax=size(ref1,1);%ss=trapz(ref1(:,1),ref1(:,2));
dist2=[0.0];tmp=0;mi=1;
for i=1:pore_r_max-pore_r_min+1
    if (mi<mimax)


    while (mi<mimax) && (ref1(mi,1)<i-pore_r_min+1)
        tmp=tmp+ref1(mi,2)*(ref1(mi+1,1)-ref1(mi,1));
        mi=mi+1;
    end

    %dist2=[dist2,tmp];
    end
    dist2=[dist2,tmp];
end
dist2=dist2/tmp;
%=============================================================
```

```
%=========================VALIDATION=========================
% test_data=[];
% for i=1:1000
%     tmp=rand;mark=0;
%     for (j=2:r_max-r_min+2)
%         if (tmp>=dist(j-1)) && (tmp<dist(j)) &&(mark==0)
%             test_data=[test_data,j-1];
%             mark=1;
%         end
%     end
% end
%
% sta=zeros(r_max-r_min+1);
% for i=1:1000
%     sta(test_data(i))=sta(test_data(i))+1;
% end
% figure
%
% plot(sta)
%============================================================

%======Random==channels=====
ch_int=r_min:r_max;
ch_int=ceil(ch_int/2);

% ch1=d/5*3;
% ch2=d/5*5;
% ch3=d/5*6.4;
% ch4=d/5*10.4;

%ch_int=[round(ch1/2),round(ch2/2),round(ch3/2),round(ch4/2)];
%ch_int=[floor(ch1/2),floor(ch2/2),floor(ch3/2),floor(ch4/2)];
% ch_int=[ceil(ch1/2),ceil(ch2/2),ceil(ch3/2),ceil(ch4/2)];
%============================
% a2=round(a/2);
% b2=round(b/2);
% c2=round(c/2);


a2=floor(a/2);
```

```
b2=floor(b/2);
c2=floor(c/2);
%================================

xdir=[left];
ydir=[down];

for i=1:lx-1
  xdir=[xdir,c];
end
for i=1:ly-1
  ydir=[ydir,c];
end
xdir=[xdir,right];
ydir=[ydir,up];

%ydir=[down,c,c,c,up];
%xdir=[left,c,c,c,right];
nx=left+c*(lx-1)+right;
ny=up+down+reservior+c*(ly-1);

pa=ones(nx,ny);


for i=1:nx
    for j=1:reservior
        pa(i,j)=0;
    end
end

%===========make pores=================
% for indx=1:lx
%     for indy=1:ly
%         corx=(indx-1)*c+left;
%         cory=reservior+(indy-1)*c+down;
%         for (i=corx-a2:corx+a2)
%             for (j=cory-a2:cory+a2)
%                 pa(i,j)=0;
%             end
%         end
```

```
%
%
%     end
% end
%=========================================

%===========make random pores=================
deb2=[];texts2=[];
for indx=1:lx
    for indy=1:ly
        corx=(indx-1)*c+left;
        cory=reservior+(indy-1)*c+down;

        tmp=rand;mark=0;
    for (j=2:pore_r_max-pore_r_min+2)
        if (tmp>=dist2(j-1)) && (tmp<dist2(j)) &&(mark==0)
            test_data=j-1;
            mark=1;
        end
    end
        chw=test_data+pore_r_min;deb2=[deb2,chw];
         %-------------------------

         %-------------------------
         texts2=[texts2;[corx,cory,chw]];
         a2=chw;
         %-------------------------
        for (i=corx-a2:corx+a2)
            for (j=cory-a2:cory+a2)
                pa(i,j)=0;
            end
        end


    end
end
%=========================================

deb=[];texts=[];shift=5;
%===============Random===channels==========
```

```
[texnx,texny]=size(texts2);


cory2=reservior;
cory1=reservior;
for indy=1:ly+1
    cory2=cory2+ydir(indy);

    for indx=1:lx

        corx=(indx-1)*c+left;

        %-------------------------
        % make the channel smaller than pores
        r_maxinternal=r_max;
        for texi=1:texnx
               if ((texts2(texi,2)>=cory1-2) &&
                   (texts2(texi,2)<=cory2+2) &&
                   ((texts2(texi,1)==corx)))
                   if (texts2(texi,3)<r_maxinternal)
                       r_maxinternal=texts2(texi,3);
                   end
               end
        end
        %r_maxinternal
        %-------------------------

        %-------------------------
      tmp=rand;mark=0;
    %for (j=2:r_max-r_min+2)
    for (j=2:r_maxinternal-pore_r_min+2)
        if (tmp>=dist(j-1)) && (tmp<dist(j)) &&(mark==0)
            test_data=j-1;
            mark=1;
        end
    end
        chw=test_data+r_min;deb=[deb,chw];
         %-------------------------

         %-------------------------
```

```
        texts=[texts;[corx-ch_int(chw)-shift,(cory1+cory2)/2,chw]];
        %-------------------------
       for i=corx-ch_int(chw):corx+ch_int(chw)
           for j=cory1:cory2
               pa(i,j)=0;
           end
       end

   end
   cory1=cory1+ydir(indy);
end


corx2=1;
corx1=1;
for indx=1:lx+1
   corx2=corx2+xdir(indx);

   for indy=1:ly

       cory=reservior+(indy-1)*c+down;
       %-------------------------

       %-------------------------
       % make the channel smaller than pores
       r_maxinternal=r_max;
       for texi=1:texnx
              if ((texts2(texi,1)>=corx1-2) &&
                  (texts2(texi,1)<=corx2+2) &&
                  ((texts2(texi,2)==cory)))
                  if (texts2(texi,3)<r_maxinternal)
                      r_maxinternal=texts2(texi,3);
                  end
              end
       end

       %-------------------------
     tmp=rand;mark=0;
   %for (j=2:r_max-r_min+2)
   for (j=2:r_maxinternal-pore_r_min+2)
```

```
        if (tmp>=dist(j-1)) && (tmp<dist(j)) &&(mark==0)
            test_data=j-1;
            mark=1;
        end
    end
        chw=test_data+r_min;deb=[deb,chw];
         %-------------------------

         %-------------------------
         texts=[texts;[(corx1+corx2)/2,cory+ch_int(chw)+shift,chw]];
         %-------------------------
        for i=corx1:corx2
            for j=cory-ch_int(chw):cory+ch_int(chw)
                pa(i,j)=0;
            end
        end

    end
    corx1=corx1+xdir(indx);
end
%=============================================

%===============side channels================
% side_w=9;
% for i=1:side_w
%     for j=reservior+down:ny
%         pa(i,j)=0;
%     end
% end
%
% for i=nx-side_w+1:nx
%     for j=reservior+down:ny
%         pa(i,j)=0;
%     end
% end
%=============================================

figure
imshow(pa);
imwrite(pa,'./image13.png');
```

```
figure
imshow(pa);
[tx,ty]=size(texts);
for i=1:tx
    text(texts(i,2),texts(i,1),int2str(texts(i,3)),'FontSize',13);
end

[tx,ty]=size(texts2);
for i=1:tx
    text(texts2(i,2),texts2(i,1),int2str(texts2(i,3)),'FontSize',13,'Color',
        'w');
end
% text(160,160,sc,'FontSize',18)
% text(190,160,'sfd','FontSize',18)

%=============STATISTICAL VALIDATION====================
stas=zeros(r_max);

[tx,ty]=size(deb);
for i=1:ty
    stas(deb(1,i))=stas(deb(1,i))+1;
end


figure
%plot(deb);
plot (r_min:r_max,num);
hold on
plot (ref2(:,1),ref2(:,2),'b');
hold on
plot(r_min:r_max,stas(r_min:r_max,1)/ty,'rx-');
hold off
legend('analytical','random distribution');
%=========================================================

%=========================================
fid = fopen('3rd_Gen_Glass_13.dat','wt');

for k=1:d+2
```

```
    for j=1:ny
        for i=1:nx
        if ((k==1) || (k==d+2))
            if (j<=reservior)
                fprintf(fid,'%1d\n',0);
            else
                fprintf(fid,'%1d\n',1);
            end
        else
            fprintf(fid,'%1d\n',pa(i,j));
        end
        end
    end
end
%=========================================

nx
ny
d+2
```

B. ImageJ Macros

Background Correction

```
input = getDirectory("Choose input folder");
output = getDirectory("Choose output folder");

function action (input, output, filename) {
   open (input + filename);
   makeRectangle(0, 36, 6960, 76);
   run("Duplicate...", "title=Drainage01-1.tif");
   run("Scale...", "x=- y=- width=6960 height=3486
       interpolation=Bilinear average create
       title=Drainage01-2.tif");
   makeRectangle(6450, 30, 18, 3186);
   run("Duplicate...", "title=Drainage01-3.tif");
   run("Scale...", "x=- y=- width=6960 height=3486
       interpolation=Bilinear average create
       title=Drainage01-4.tif");
   imageCalculator("Subtract create",
       "Drainage01-2.tif","Drainage01-4.tif");
   selectWindow("Result of Drainage01-2.tif");
   imageCalculator("Subtract create", filename, "Result of
       Drainage01-2.tif");
   saveAs("tif", output + filename);
   close();
}

setBatchMode(true);
images = getFileList(input);
for (i=0; i<images.length; i++)
action(input, output, images[i]);
setBatchMode(false);
```

Image Variation

```
input = getDirectory("Choose input folder");
output = getDirectory("Choose output folder");

function difference (input, output, filename) {
   open (input + filename);
   imageCalculator("Subtract create", "Drainage01.tif",filename);
   selectWindow("Result of Drainage01.tif");
   saveAs("tif", output + filename);
   close();
}

setBatchMode(true);
images = getFileList(input);
for (i=0; i<images.length; i++)
difference(input, output, images[i]);
setBatchMode(false);
```

Image Segmentation

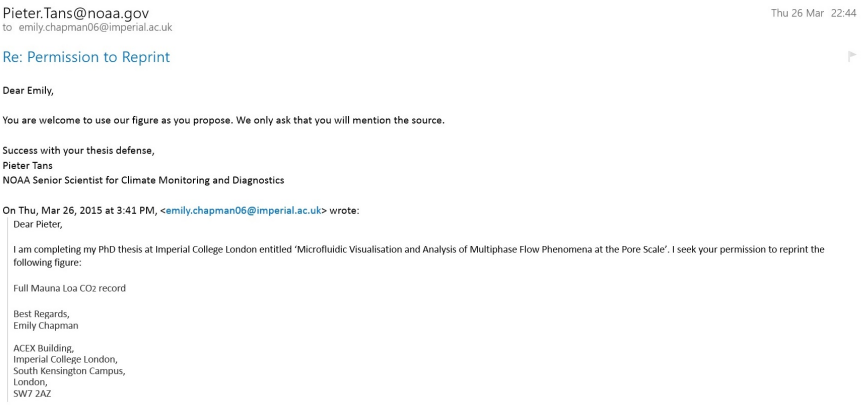
```
input = getDirectory("Choose input folder");
output = getDirectory("Choose output folder");

function threshold (input, output, filename) {
   open (input + filename);
// Color Thresholder 1.48b
// Autogenerated macro, single images only!
min=newArray(3);
max=newArray(3);
filter=newArray(3);
a=getTitle();
run("RGB Stack");
run("Convert Stack to Images");
selectWindow("Red");
rename("0");
selectWindow("Green");
rename("1");
selectWindow("Blue");
```

```
rename("2");
min[0]=13;
max[0]=255;
filter[0]="pass";
min[1]=3;
max[1]=255;
filter[1]="stop";
min[2]=3;
max[2]=255;
filter[2]="stop";
for (i=0;i<3;i++){
  selectWindow(""+i);
  setThreshold(min[i], max[i]);
  run("Convert to Mask");
  if (filter[i]=="stop") run("Invert");
}
imageCalculator("AND create", "0","1");
imageCalculator("AND create", "Result of 0","2");
for (i=0;i<3;i++){
  selectWindow(""+i);
  close();
}
selectWindow("Result of 0");
close();
selectWindow("Result of Result of 0");
rename(a);
// Colour Thresholding-------------
   saveAs("tif", output + filename);
   close();
}

setBatchMode(true);
images = getFileList(input);
for (i=0; i<images.length; i++)
threshold(input, output, images[i]);
setBatchMode(false);
```

C. Permissions



Pieter.Tans@noaa.gov
to emily.chapman06@imperial.ac.uk

Thu 26 Mar 22:44

Re: Permission to Reprint

Dear Emily,

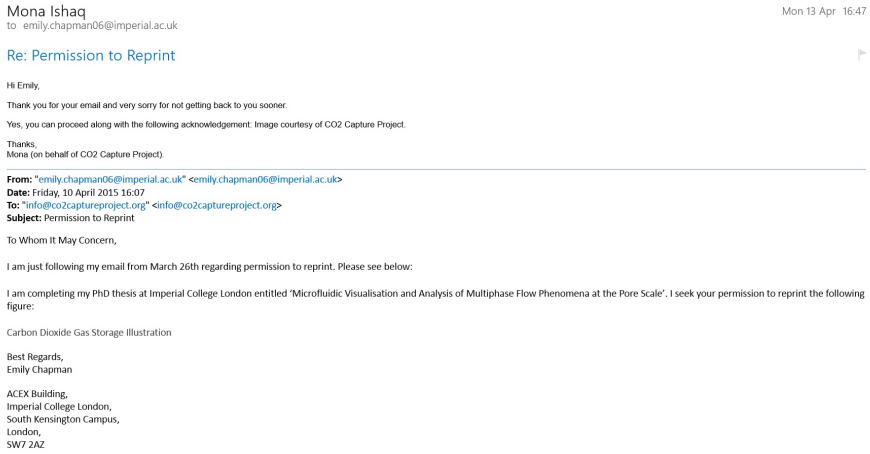
You are welcome to use our figure as you propose. We only ask that you will mention the source.

Success with your thesis defense,
Pieter Tans
NOAA Senior Scientist for Climate Monitoring and Diagnostics

On Thu, Mar 26, 2015 at 3:41 PM, <emily.chapman06@imperial.ac.uk> wrote:

> Dear Pieter,
>
> I am completing my PhD thesis at Imperial College London entitled 'Microfluidic Visualisation and Analysis of Multiphase Flow Phenomena at the Pore Scale'. I seek your permission to reprint the following figure:
>
> Full Mauna Loa CO2 record
>
> Best Regards,
> Emily Chapman
>
> ACEX Building,
> Imperial College London,
> South Kensington Campus,
> London,
> SW7 2AZ

Figure C.1.: NOAA permission to reprint Figure 1.1.B.



Mona Ishaq
to emily.chapman06@imperial.ac.uk

Mon 13 Apr 16:47

Re: Permission to Reprint

Hi Emily,

Thank you for your email and very sorry for not getting back to you sooner.

Yes, you can proceed along with the following acknowledgement: Image courtesy of CO2 Capture Project.

Thanks,
Mona (on behalf of CO2 Capture Project).

From: "emily.chapman06@imperial.ac.uk" <emily.chapman06@imperial.ac.uk>
Date: Friday, 10 April 2015 16:07
To: "info@co2captureproject.org" <info@co2captureproject.org>
Subject: Permission to Reprint

To Whom It May Concern,

I am just following my email from March 26th regarding permission to reprint. Please see below:

I am completing my PhD thesis at Imperial College London entitled 'Microfluidic Visualisation and Analysis of Multiphase Flow Phenomena at the Pore Scale'. I seek your permission to reprint the following figure:

Carbon Dioxide Gas Storage Illustration

Best Regards,
Emily Chapman

ACEX Building,
Imperial College London,
South Kensington Campus,
London,
SW7 2AZ

Figure C.2.: CO_2 Capture Project permission to reprint Figure 1.2.

FW: Permission to Reprint

Dear Emily,

Dover hereby grants you permission to reproduce the figure you mention below in your PhD thesis. Please give credit to the Dover edition in any standard form.

Thanks,

Joann
From: emily.chapman06@imperial.ac.uk [mailto:emily.chapman06@imperial.ac.uk]
Sent: Thursday, March 26, 2015 5:47 PM
To: Diana_Grey
Subject: Permission to Reprint

To Whom It May Concern,

I am completing my PhD thesis at Imperial College London entitled 'Microfluidic Visualisation and Analysis of Multiphase Flow Phenomena at the Pore Scale. I seek your permission to reprint the following figure:

J. Bear, Dynamics of Fluids in Porous Media.
Figure 9.2.4, page 445

Best Regards,
Emily Chapman

ACEX Building,
Imperial College London,
South Kensington Campus,
London,
SW7 2AZ

Figure C.3.: Dover permission to reprint Figure 2.2.

SOCIETY OF PETROLEUM ENGINEERS LICENSE
TERMS AND CONDITIONS
Apr 26, 2015

This is a License Agreement between Emily M Chapman ("You") and Society of Petroleum Engineers ("Society of Petroleum Engineers") provided by Copyright Clearance Center ("CCC"). The license consists of your order details, the terms and conditions provided by Society of Petroleum Engineers, and the payment terms and conditions.

License Number	3596730058849
License date	Mar 26, 2015
Licensed content publisher	Society of Petroleum Engineers
Licensed content publication	SPE Proceedings
Licensed content title	Surfactant Optimization for EOR using Advanced Chemical Computational Methods
Licensed content author	Marten Adriaan Buijse, Shell Exploration & Production;Kunj Tandon, Shell;Shekhar Jain, Shell et al
Licensed content date	2012
Type of Use	Thesis/Dissertation
Requestor type	academic/educational
SPE member	no
Format	print and electronic
Portion	figures/tables/images
Number of figures/tables/images	1
Will you be translating?	no
Distribution	25
Order reference number	None
Title of your thesis / dissertation	Microfluidic Visualisation and Analysis of Multiphase Flow Phenomena at the Pore Scale
Expected completion date	Apr 2015
Estimated size (number of pages)	182
Billing Type	Credit Card
Credit card info	Visa ending in 7594
Credit card expiration	12/2016
Total	13.50 USD

Figure C.4.: SPE permission to reprint Figure 2.8.

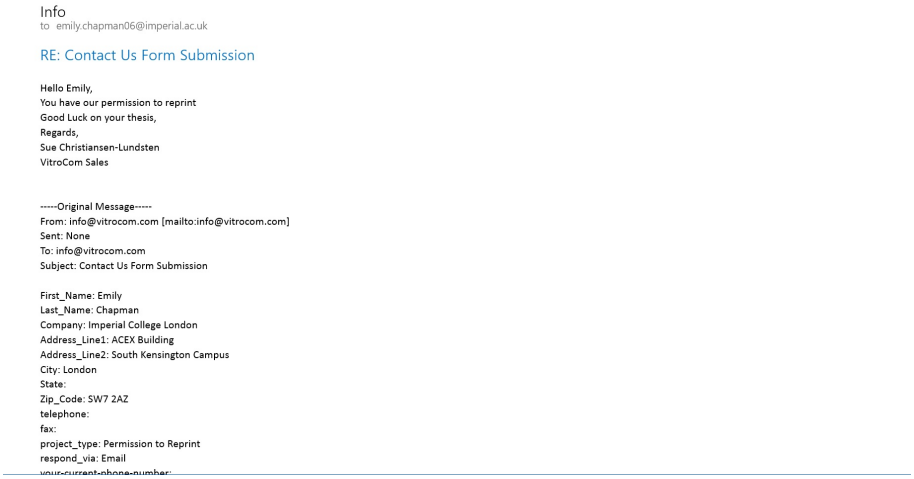
CAMBRIDGE UNIVERSITY PRESS LICENSE
TERMS AND CONDITIONS
Apr 26, 2015

This is a License Agreement between Emily M Chapman ("You") and Cambridge University Press ("Cambridge University Press") provided by Copyright Clearance Center ("CCC"). The license consists of your order details, the terms and conditions provided by Cambridge University Press, and the payment terms and conditions.

All payments must be made in full to CCC. For payment instructions, please see information listed at the bottom of this form.

License Number	3596711136064
License date	Mar 26, 2015
Licensed content publisher	Cambridge University Press
Licensed content publication	The Journal of Fluid Mechanics
Licensed content title	Mechanisms of the displacement of one fluid by another in a network of capillary ducts
Licensed content author	R. Lenormand, C. Zarcone and A. Sarr
Licensed content date	Apr 20, 2006
Volume number	135
Issue number	-1
Start page	337
End page	353
Type of Use	Dissertation/Thesis
Requestor type	Not-for-profit
Portion	Text extract
Number of pages requested	1
Order reference number	None
Territory for reuse	World
Title of your thesis / dissertation	Microfluidic Visualisation and Analysis of Multiphase Flow Phenomena at the Pore Scale
Expected completion date	Apr 2015
Estimated size(pages)	182
Billing Type	Invoice
Billing Address	Emily M Chapman 65C Albert Bridge Road London, United Kingdom SW11 4QA Attn: Emily M Chapman
TAX (0.00%)	0.00 GBP
Total	0.00 GBP

Figure C.5.: Cambridge University Press permission to reprint Figure 2.12.



Info
to emily.chapman06@imperial.ac.uk

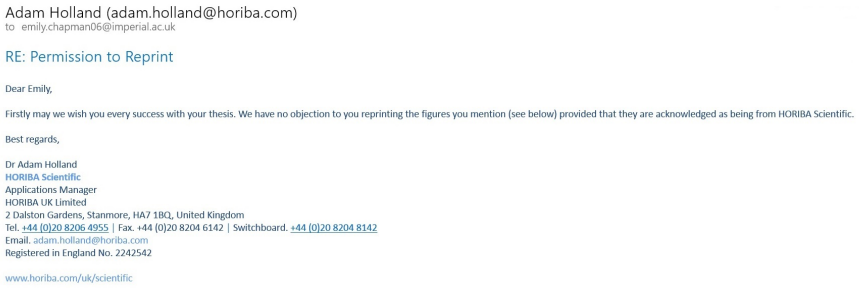
RE: Contact Us Form Submission

Hello Emily,
You have our permission to reprint
Good Luck on your thesis,
Regards,
Sue Christiansen-Lundsten
VitroCom Sales

-----Original Message-----
From: info@vitrocom.com [mailto:info@vitrocom.com]
Sent: None
To: info@vitrocom.com
Subject: Contact Us Form Submission

First_Name: Emily
Last_Name: Chapman
Company: Imperial College London
Address_Line1: ACEX Building
Address_Line2: South Kensington Campus
City: London
State:
Zip_Code: SW7 2AZ
telephone:
fax:
project_type: Permission to Reprint
respond_via: Email
your-current-phone-number:

Figure C.6.: VitroCom permission to reprint Figure 4.1.



Adam Holland (adam.holland@horiba.com)
to emily.chapman06@imperial.ac.uk

RE: Permission to Reprint

Dear Emily,

Firstly may we wish you every success with your thesis. We have no objection to you reprinting the figures you mention (see below) provided that they are acknowledged as being from HORIBA Scientific.

Best regards,

Dr Adam Holland
HORIBA Scientific
Applications Manager
HORIBA UK Limited
2 Dalston Gardens, Stanmore, HA7 1BQ, United Kingdom
Tel. +44 (0)20 8206 4955 | Fax. +44 (0)20 8204 6142 | Switchboard. +44 (0)20 8204 8142
Email. adam.holland@horiba.com
Registered in England No. 2242542

www.horiba.com/uk/scientific

Figure C.7.: HORIBA Scientific permission to reprint Figures 7.1, 7.2 and 7.3.

SOCIETY OF PETROLEUM ENGINEERS LICENSE
TERMS AND CONDITIONS
Apr 26, 2015

This is a License Agreement between Emily M Chapman ("You") and Society of Petroleum Engineers ("Society of Petroleum Engineers") provided by Copyright Clearance Center ("CCC"). The license consists of your order details, the terms and conditions provided by Society of Petroleum Engineers, and the payment terms and conditions.

License Number	3596721383398
License date	Mar 26, 2015
Licensed content publisher	Society of Petroleum Engineers
Licensed content publication	SPE Reservoir Evaluation & Engineering
Licensed content title	Identification and Evaluation of High-Performance EOR Surfactants
Licensed content author	David Levitt, University of Texas at Austin;Adam Jackson, Chevron Corp.;Christopher Heinson, Oxy et al
Licensed content date	2009
Volume number	12
Issue number	02
Type of Use	Thesis/Dissertation
Requestor type	academic/educational
SPE member	no
Format	print and electronic
Portion	figures/tables/images
Number of figures/tables/images	1
Will you be translating?	no
Distribution	25
Order reference number	None
Title of your thesis / dissertation	Microfluidic Visualisation and Analysis of Multiphase Flow Phenomena at the Pore Scale
Expected completion date	Apr 2015
Estimated size (number of pages)	182
Billing Type	Credit Card
Credit card info	Visa ending in 7594
Credit card expiration	12/2016
Total	13.50 USD

Figure C.8.: SPE permission to reprint Figure 7.11.